Bulk Heterojunction Organic Solar Cells Based on Crosslinked Polymer Donor Networks

Liu Bo

In partial fulfillment of the requirements for the

Degree of Doctor of Philosophy

Department of Physics

National University of Singapore

July 2012

For Father and Mother,

For Yuan Chai

Acknowledgements

The work described in this thesis was carried out in the Organic Nano Device Lab (ONDL), National University of Singapore (NUS) from August 2008 to July 2012, and was supported by research scholarship from the Department of Physics in NUS.

Looking back at the four years I have spent in National University of Singapore, I feel lucky and grateful to become who I am. Without the help and support from following people, the thesis would not have been possible.

First and foremost I would like to thank my supervisor Dr. Peter HO for accepting me as a member of the Organic Nano Device Laboratory (ONDL) at which the work described in this thesis is carried out. I am grateful to Peter for his guidance and ideas in the field of organic electronics and his patience, continuous support and enlightenment in my project.

Further I wish to express my gratitude to Chia Perq Jon for his guidance, and more importantly, his optimistic, affirmative and encouraging attitudes helped me build my confidence in the early stage of research career. I also want to say a big thank you to Zhou Mi, for his stimulating and inspirational discussions and comments. It is a luxury to have a big brother watching me and frankly pointing out my shortcomings. Next, my gratitude goes to Rachael, for her support, insightful discussions and covering for me in many occasions.

I also want to thank Dr. Lay-Lay Chua, and some colleagues, Li-Hong, Jing-Mei, Loke Yuen, Zhili, Guo Han for their brilliant work and scientific discussions, and all the current and former ONDL members for the wonderful company and making this period fruitful and memorable.

I would like to acknowledge Jie-cong and Bibin for the synthesis of crosslinker, Li-hong and Guo Han for the UPS/XPS measurements, Dagmawi for part of the EA measurements, and Jun Kai for proofreading, assisting some experiments and figure preparations.

Special gratitude goes to my mum and dad for their unconditional support to my years of overseas education. Finally I would thank dearest Ms. Chai Yuan for her love and support.

Abstract

The power conversion efficiency (*PCE*) of organic photovoltaic cells depends crucially on the morphology of their donor–acceptor heterostructure amongst other factors. While tremendous progress has been made to develop new donor and acceptor materials that better cover the solar spectrum, their heterostructure is still formed by a rather primitive process of spontaneous demixing. This is rather sensitive to processing conditions and hence difficult to realise over the large areas needed for manufacturing. In this thesis, it is demonstrated that the ideal interpenetrating heterostructure where the donor and acceptor phases are intimately mixed at the ten-nanometer length scale but contiguous over the device thickness can be readily created by acceptor doping into a lightly-crosslinked polymer donor network. The resultant nanotemplated network is markedly insensitive to processing conditions and resilient to phase coarsening. It also shows surprisingly the excellent local molecular order required for efficient carrier transport. A general 20% improvement in *PCE* for the prototypical regioregular poly(3-hexylthiophene) (P3HT): phenyl-C61-butyrate methyl ester (PCBM) donor–acceptor system to reach 4.2% has been found using this method over the usual spincast biblend devices. Since the donor–acceptor morphology is now predetermined by the crosslinking density independent of the P3HT: PCBM ratio, it is possible to critically test the standard optical–electrical model for P3HT: PCBM, and refine the parameters using data obtained in this work. To improve model reliability, we have moreover directly measured the built-in potential V_{bi} of these cells using electromodulated absorption spectroscopy to be 0.75 V, with negative polaron levels of P3HT and PCBM at 3.2 and 3.5 eV respectively. The open-circuit voltage deficit is thus only 0.1–0.15 V, which we have determined to arise here largely from majority carrier injection at the ohmic contacts. Excellent agreement

between the model and experimental current−voltage characteristics were obtained over a wide thickness range using a single global parameter set. Analysis of the results further suggests: (a) the electron–hole recombination rate constant is 2–3 orders of magnitude lower than the Langevin constant, as other authors have reported; and (b) the interface mobile carrier density is 1–2 orders of magnitude lower than the actual δ-doped carrier density in the organic semiconductor at the contacts. The latter suggests significant energetic spread of the carriers. Using the refined parameter set, we have systematically examined the transport and optical-structure optimization landscapes of organic solar cells in general. We established: (i) the importance of high carrier mobilities, and of mobility mismatch to enhance photocarrier collection from an asymmetric exciton-generation profile, and (ii) the existence of a remarkably simple λ_p / n_{PAL} scaling law, where λ_p is the absorption center wavelength and n_{PAL} is the refractive index, that determines the optimal absorption thickness of the photoactive layer. These results reveal new device insights and lay down a clear path for the systematic optimization of organic solar cells.

In Chapter 2, accurate determination of organic solar cells performance and calibration of solar simulator will be discussed, along with the calibration of silicon photodiode and spectrograph system.

In Chapter 3, a novel molecular infiltration method to fabricate polymer-based solar cells using sterically hindered bis(fluorophenyl azide)s (s-FPAs or crosslinker) is introduced. The donor polymer film is first deposited and photocrosslinked with versatile high-efficiency nitrene chemistry, then the molecular acceptor is “doped” into this film by contact with its solution under precise control. The morphologies of these devices has been characterized by AFM and TEM. The 2D *PCE* map of regioregular poly(3-hexylthiophene) (rrP3HT):phenyl-C61-butyrate methyl ester

(PCBM) solar cells as a function of the effective amount of rrP3HT and PCBM in the film was obtained for the first time. The results reveal a “ridge of efficiency” that coincides with the 1:0.8 P3HT: PCBM weight ratio line comprising islands of particularly high efficiencies at both low and high film thicknesses (maximum *PCE*, 4.2%). The *PCE* are generally 20-30% higher than blend films of the same composition made by conventional spin-casting. Further analysis shows that the internal quantum efficiency (*IQE*) of the crosslinked devices is near to unity across a wide range of thickness and composition, which is a special advantage of the crosslinking method.

Chapter 4 presents the built-in potential (V_{bi}) characterization of the crosslinked network devices and conventional blend devices by electroabsorption spectroscopy (Stark spectroscopy). The accurate measurement of V_{bi} is fundamental to the understanding of the device physics and possible loss mechanism, as described by the drift-diffusion model in Chapter 5.

Chapter 5 incorporates the optical modeling and electrical modeling to understand the device physics and loss mechanism of P3HT: PCBM solar cells. Most parameters in the model are independently measured by experiments, and the number of fitting parameters is kept as small as possible. The match of modeling results and experimental data indicates that the donor–acceptor morphology in crosslinked network P3HT: PCBM solar cell is identical across a wide range of composition and thickness. Amongst the new insights that have thus been achieved includes how the power-conversion-efficiency landscape varies with photoactive layer composition and thickness, and the role of optical interference, asymmetric carrier mobilities, carrier recombination, and injection boundary conditions in determining the optimal structure for organic solar cells.

Table of Contents

List of Figure

Chapter 1. Introduction

1.1 Solar energy

As the world consumption of mineral resources and gasoline increases, the need for renewable materials and energy becomes more urgent. All forms of energy are expensive, but as time progresses and technology advances, the renewable energy generally gets cheaper, while the fossil fuels like petroleum and coals get more expensive. Thus, the renewable energy will be more cost-effective than the traditional fossil fuels someday. Among the renewable energy, solar energy has special characteristics such as great ampleness and the superior accessibility compared with hydroelectricity, wind power, biofuels and geothermal energy. The technologies of photovoltaics (PV) and solar cells have been driven by the passion for the unlimited potential of solar energy and they have become a fast growing industry. However, the cost of PV and solar cell has to drop for economic viability. One has to keep in mind that the on-grid electricity price is typically 10-20 US cents/KWh,[1] while the PV techniques are trying hard to target 0.5-1 USD/KWh. On the other hand, the solar energy density is intrinsically low, capped at 1 kW/m^2, which is the total solar energy density received on earth. Let us consider the civil use first: Assuming that one family can have about 20m^2 for solar panel installation in urban area, and the module efficiency is decently 20%, the maximum continuous output is 20 m^2 * 1 kW/m^2 *20% = 4 kW, definitely not enough to meet the everyday demand, not to mention the industrial use or powering a car. Even though the energy can be stored for later use, at least 20% of it is lost during charging-discharging process. Thus, the currently practical utilization of solar energy would be supplementary in urban areas or off-grid applications in rural areas.

1.2 State-of-the-art solar cell technologies

For both inorganic and organic photovoltaic products and technologies, there are three main matrices for the commercialization: efficiency, cost and lifetime. Minimum requirements of 10% module efficiency, 10+ year lifetime and competitive price have to be reached simultaneously for the large scale commercial photovoltaic application.

The first crystalline silicon solar cell was developed at Bell Laboratories,[2] with 6% power conversion efficiency. In recent years, the efficiency of crystalline silicon solar cell has reached 25%,[3] which is quite close to the theoretical limit of 30%.[4,5] Although the Si solar cell dominates the PV market, with more than 85% market share, it accounts for less than 0.1% of world total energy production. Furthermore, the limited availability of "solar grade" Si raw material has caused the volatility of the silicon panel price and affected the production scale. The rest of the PV market is taken by thin film solar cells such as hydrogenated amorphous silicon (a-Si:H), cadmium telluride (CdTe), and copper-indium-gallium-selenide $CuIn_xGa_{1-x}Se_2$ (CIGS), which have shown decent efficiencies and been commercialised with limited scale though. However, they have some disadvantages like pollution (Cd, Te), shortage of raw materials (Cu, In), and fragility which require additional expensive glass support to protect.

Another promising thin film solar cell is dye-sensitized solar cell (DSSC)[6] that consists of a thin and porous titanium dioxide layer immersed with a photosensitive dye (ruthenium-polypyridine) and liquid iodide electrolyte. Despite the highest efficiency among the 3rd generation solar cell, good processability and better performance under indoor light than amorphous silicon,[7] DSSC has a major disadvantage with the use of the liquid electrolyte, which has temperature and chemical stability problems, making it not the ultimate solution.

Therefore, to design a sustainable and economic technology path for solar cells, new concepts and materials need to be developed. One possible route is based on conjugated polymers.

1.3 Conjugated polymer

Since Shirakawa, MacDiarmid and Heeger discovered in 1977 that the conductivity of conjugated polymers can be increased by more than 5 orders to the semiconductor level (10 S/cm) by doping,[8] a new field has emerged. They shared the Nobel Prize in chemistry in 2000 for this work. It was since 1990 that the field of organic electronics started to boom, after the demonstration of electroluminescence in conjugated polymers.[9] It was an important step when the great potential of applications on electronics of organic materials started to attract people's interests, followed by the discovery of novel devices and understanding of the device physics,[10-12] and the commercial organic electronics market today. The prospect of organic materials lies in the versatility and processibility which enables the possibility of new applications, like ultrathin flexible displays,[13] disposable sensors,[14,15] etc, that are never possible to be made by inorganic materials.

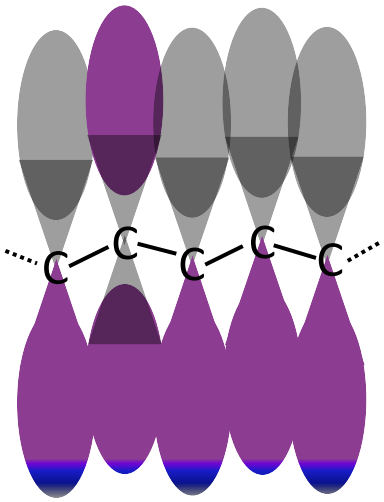

Figure 1.1 Illustration of π orbitals overlapping in conjugated polymers. The C-C bonds are partially double, and the electrons are delocalized across the whole alkyl chain.

The semiconducting properties of most of the conjugated polymers stem from the overlapping of the *p*-orbital wavefunctions (forming π bonds) of consecutive units, which are jointed by σ bonds (illustrated in **Figure 1.1**). In contrast, the industrial plastics are mainly jointed by σ bonds and are insulators. The overlapping allows delocalization of π electrons across all the adjacent aligned p-orbitals and the π electrons do not belong to a single bond or atom, but rather to a group of atoms, forming molecular orbitals. As the π electrons fill up the molecular orbitals, the filled π band with highest energy is called the highest occupied molecular orbital (HOMO) and the empty π^* band with lowest energy is called the lowest unoccupied molecular orbital (LUMO). The difference of LUMO and HOMO is the band gap of the conjugated polymer, which is reduced as the conjugation length increases (**Figure 1.2**).

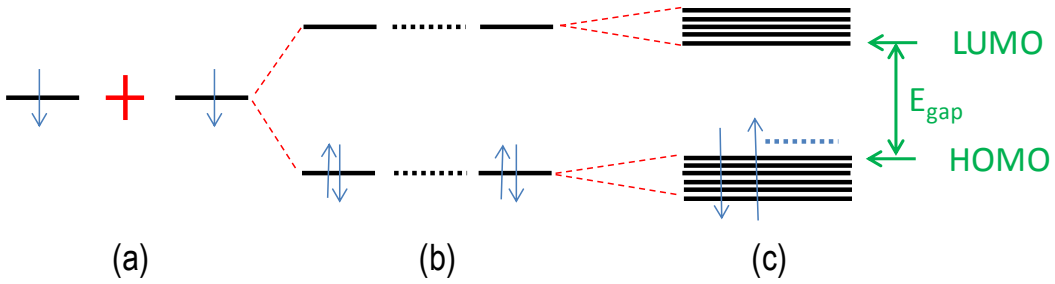

Figure 1.2 Energy states of π bond formation in conjugated polymer. **(a).** Single atomic states. **(b).** Bonding orbitals and anti-bonding orbitals. **(c).** Non-degeneracy of the π orbitals in conjugated polymer. E_{gap}, HOMO and LUMO level are shown.

The π electron can be excited by a photon with energy larger than the polymer band gap, without breaking the backbones (π bonds). Every π electron can be potentially excited by a photon, which explains the much higher absorption coefficient of conjugated polymers compared with inorganic materials. On the other hand, due to the spatial and energetic disorder in the system, the disturbance of the conjugation along the polymer backbone will change the HOMO and LUMO locally,[16] thus the density of states shows Gaussian like distribution[16,17] and the absorption spectrum is usually a broad band without distinct peaks. In **Figure 1.3**, a series of poly(para-phenylene-vinylene) (PPV) based conjugated polymers with tuneable bandgap and absorption range are shown.

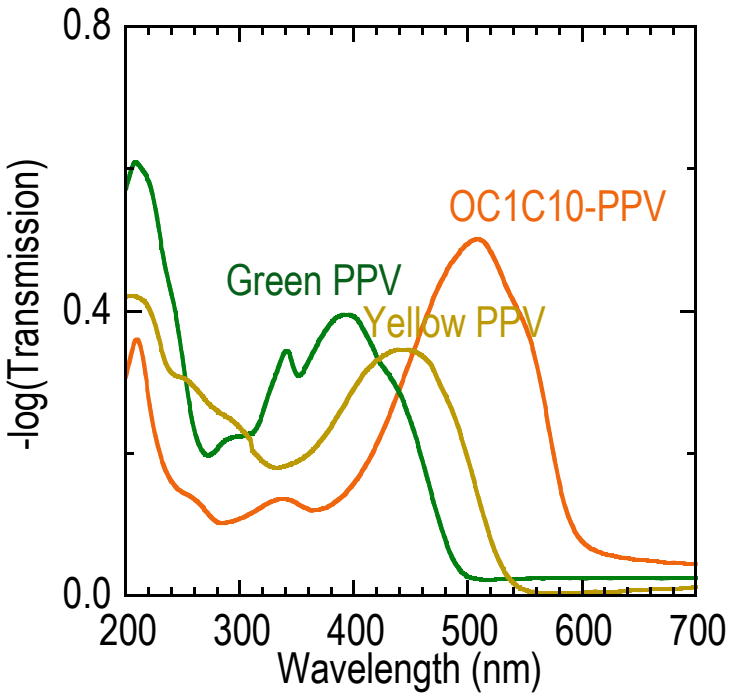

Figure 1.3 Systematically showing controllable band gap and appearance colour of PPV series.

In the aspect of processing method, polymer is conceptually different from inorganic material or organic small molecules. Due to the large size of the polymer molecules, the inter- and intra-molecular interaction become so complicated that polymer does not easily form crystals, but usually a glassy, amorphous state. When spun from solution, it forms a smooth film with a thickness ranging from tens of nanometer to several micrometers. Conjugated polymer combine the excellent processing and mechanical properties of polymer and the opto-electronic properties of semiconductors, making it an ideal candidate for large area and light weight applications, such as lighting panels,[18,19] solar cell panels[20,21] and large size TVs and screens,[13] etc.

1.4 Organic bulk heterojunction (BHJ) solar cells

The history of organic solar cell dates back to 1959 when an anthracene single crystal cell exhibited a photovoltage of 200mV with very low efficiency. In the next twenty years, the progress on organic solar cell research was slow, and the PV devices based on single material (or homojunction) could achieve 0.1% power conversion efficiency (*PCE*) at most, which was unpractical for any applications. This was mainly attributed to the fact that organic materials have low relative dielectric constant (typically 2-4) compared with inorganic semiconductors, which leads to a mobile bounded electron-hole pair (known as exciton) upon light absorption, while a free electron-hole pair is generated in an inorganic solar cell. The electric field generated by asymmetric work function of the electrodes is too weak to efficiently separate the exciton into electron and hole,[22-24] while exciton itself has very limited diffusion length (1-10nm) before decaying to the ground state. In addition, the typical charge mobility in an organic solar cell device is low (0.001cm^2/Vs or less), making the chance low for electron and hole to travel to the respective electrodes to form current before they recombine. This picture was changed when Tang put two materials (referred as donor and acceptor) in contact and showed *PCE* of 1% in 1986.[25] In 1992, ultrafast photo-induced electron transfer from conjugated polymer to fullerene molecule (C60) was shown by Sariciftci,[26] bringing fullerene and its derivatives[27] to the centre of the stage. A major breakthrough came soon when Heeger's group and Friend's group reported the concept of bulk heterojunction by blending polymer and fullerene or two polymers in 1995.[28,29] Bulk heterojunction allows for more interfacial contact between the donor/ acceptor phases (thus more charge transfer) than the previous planar heterojunction. Since then, the chemists has spent considerable amount of effort on developing new polymers and fullerene derivatives to push forward the performance of the organic solar cells.[30-33]

Unfortunately, two decades have passed, and we have not advanced much from the concept of heterojunction while the *PCE* record has reached 10% for tandem cells.[34]

1.4.1 The structure and mechanism of heterojunction solar cells

The schematic layout of a typical BHJ solar cell is shown in **Figure 1.4**. It consists of a photoactive layer, responsible for photon absorption and charge separation, sandwiched between two electrodes to collect the electrons and holes, respectively. The commonly used substrates are glass or PET, and the anode material is dominantly indium-tin oxide (ITO) for its transparency and conductivity. A nearly transparent aqueous composite PEDT:PSS, which consists of polyethylenedioxythiophene (PEDOT) and polystyrenesulfonate (PSS), is used as a cover layer to deepen the anode work function and block the electron current.[35-37] The photoactive layer will be spun on top of it, followed by the evaporation of a low work function metal (such as calcium, lithium fluoride or aluminium) under high vacuum as the cathode. In the last twenty years, the main research interest of photoactive layer has been focused on conjugated polymer and fullerenes. Polymer acts as (electron) donor, simply because most known polymer conducts holes better than electrons, and fullerene and derivatives are currently the best (electron) acceptors due to their high electron affinity, capability to delocalize and stabilize charges and its ball-like shape to easily fill the voids in polymer donor phase and alleviate the phase separation between donor and acceptor, even though they bear some intrinsic problems like instability in air.[38-40] Some examples of polymers and fullerenes used in BHJ solar cell devices are shown in **Figure 1.5**.

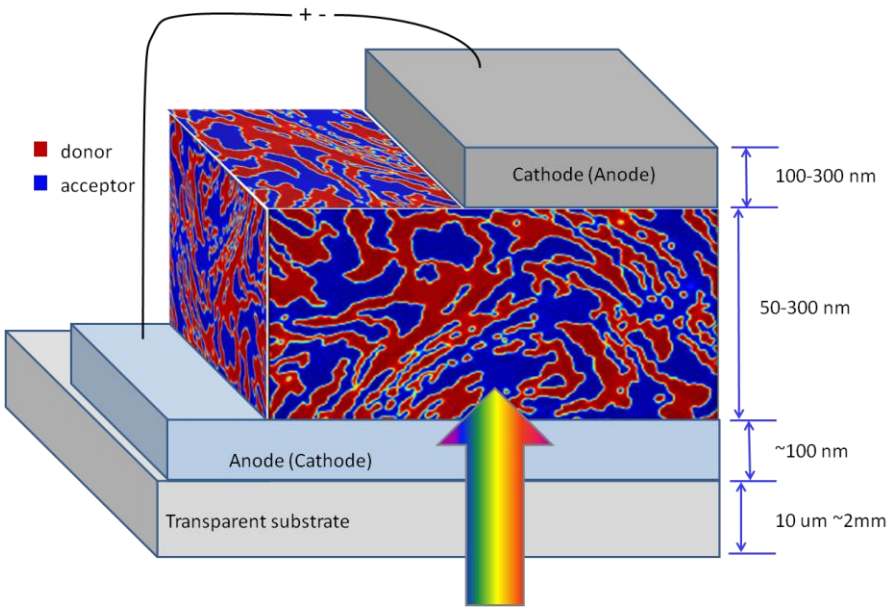

Figure 1.4 Schematic layout of a typical bulk heterojunction solar cell. The most widely used device structure is glass/ ITO/ PEDOT: PSSH/ active layer/ Ca/ Al.

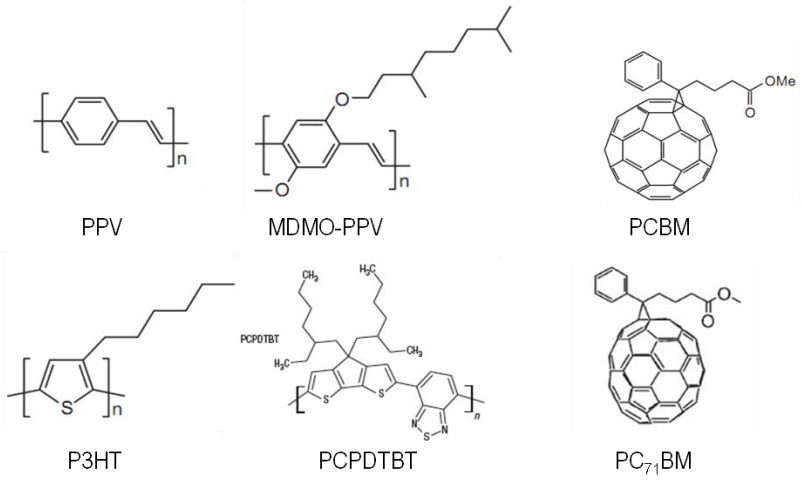

Figure 1.5 Chemical structures and abbreviations of some typical polymers and fullerenes used in organic solar cells. First row from left: poly(para-phenylene-vinylene) or PPV, poly(2-methoxy-5-(3'-7'-dimethyloctyloxy)-1,4-phenylenevinylene), or MDMO-PPV and a C60 derivative, phenyl-C61-butyric acid methyl ester (PCBM).Second row from left: poly(3-hexyl thiophene) or P3HT, poly[2,1,3-benzothiadiazole-4,7-diyl[4,4-bis(2-ethylhexyl)-4H-cyclopenta[2,1-b:3,4-b']dithiophene-2,6-diyl]] or PCPDTBT, a blue color low band gap polymer and a C_{70} derivative: $PC_{71}BM$. Fullerenes are quisi-2D spherical conjugated system, while polymers are 1D conjugated system.

Since the charge transfer can only take place at the donor/ acceptor interface[41,42] when the exciton binding energy is overcome by the band offset between donor and acceptor, controlling the nanoscale morphology of the donor- acceptor system becomes one of the key challenges in organic solar cell design and fabrication.[43-45]

As previously discussed, the planar heterojunction has the simplest structure and well defined morphology as shown in **Figure 1.6(a).** In fact, it is common in small molecule p-i-n junction solar cells. However, this structure requires stringent conditions such as small film thickness and high mobility to make efficient solar cells, because only the exciton that diffuses to the interface can be dissociated into electron-hole pair. While in a bulk heterojunction, the D/A interfacial area (photoactive area) is largely enhanced, as illustrated in **Figure 1.6(b)**, potentially leads to more separated charges if the charges can find their conducting paths to the respective electrodes. The problem is that the phase separation length scale cannot be directly controlled, nor can the presence of isolated phase or dead ends. **Figure 1.6(c)** demonstrates a hypothetical engineered structure, which conceives ordered morphology, proper conducting paths and large photoactive area. However, it has not been experimentally testified to be better than bulk heterojunction yet.

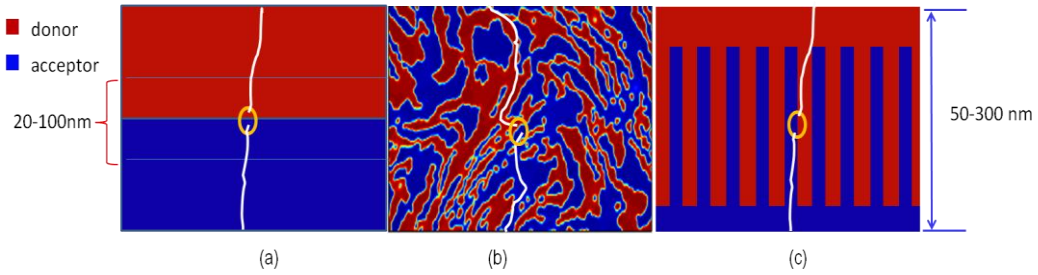

Figure 1.6 2D representation of **(a)** planar, **(b)** bulk and **(c)** engineered heterojunction. The photocurrent generation sites are highlighted in the yellow circles and the conducting paths are also indicated. The photoactive region in planar heterojunction is no more than 50 nm from the D/A interface. The interfacial area is much larger in **(b)** and **(c)** than in **(a).**

The mechanism of photocurrent generation is shown in **Figure 1.7** at the generation site. Firstly, upon photon absorption, a bound electron hole pair (exciton) is created in the donor (acceptor). It can be also considered as an electron excited from HOMO to LUMO level of the donor (acceptor). Then the exciton diffuses to the D/A interface, where the electron at the donor LUMO can be transferred to the acceptor LUMO, if the energy gain from the LUMO offset is enough to overcome the Coulomb binding barrier, forming a so called charge transfer (CT) state. The analysis also applies for the holes at the acceptor HOMO level. The CT state may relax to the ground state radioactively and triplet state non-radioactively, or separate into free electron and hole, which may undergo trap assisted recombination or Langevin type recombination before reaching the electrodes.[46-48]

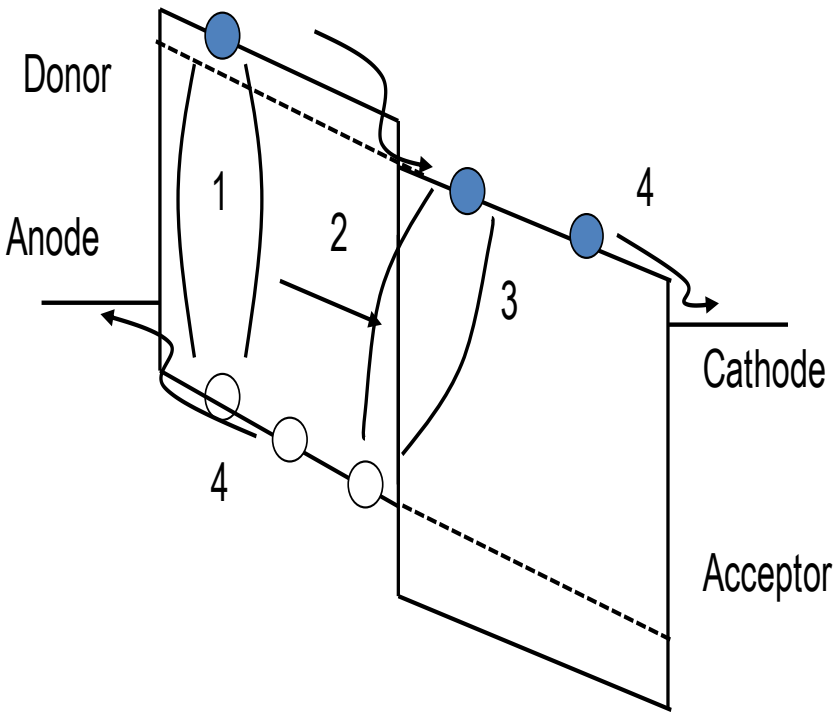

Figure 1.7 Photocurrent generation mechanism at the donor-acceptor interface.

The maximum output current of a solar cell device is uniquely determined by the above processes. The external quantum efficiency of a photovoltaic cell can be described: $\eta_{EQE} = \eta_A \times \eta_{ES} \times \eta_{ED} \times \eta_{CC}$, with the light absorption rate η_A, the exciton surviving yield η_{ES}, which is the fraction of excitons that can successfully diffuse to the D/A interface, dissociation efficiency η_{ED}, which is the fraction of excitons that dissociate into free electrons and holes at the D/A interface, and the charge carrier collection efficiency η_{CC}, which is the probability that a photo-generated free carrier reaches its corresponding electrode.

The main limiting factor for planar heterojunction is the $\eta_A \times \eta_{ES}$, meaning the number of excitons that can reach the D/A interface. The bulk-heterojunction can be very efficient in converting photons to electrons, e.g. the η_{EQE} has been reported to be as high as 65% at some wavelengths for P3HT: PCBM solar cell[49] or even near 100% in some new polymer: fullerene

systems.[50,51] On the other hand, the attempts to fabricate "nearly ideal" ordered morphology turn out to be not so inspiring, possibly because the controlled length-scale exceeds the exciton diffusion length in most polymers.[52,53]

1.4.2 Understanding the morphology in BHJ

From the discussion of last section, we know that the morphology of the bulk heterojunction is intrinsically related to efficiency. Thus, understanding and controlling the morphology is important or even necessary to further improve the device performance. In this section, the current understanding of the morphology of bulk heterojunction will be discussed, and the effort and methods to control or manipulate the morphology will come in next section.

The term *morphology* in this thesis includes surface topography, phase separation (or binary material distribution) and phase properties (crystallinity, continuity and stability). Surface topography of a sample such as BHJ film can be easily measured by Atomic Force Microscopy (AFM) without differentiating the components. Intuitively, a rough surface does not embody a finer inner structure, because such a structure is not thermodynamically stable. In contrary, a smooth surface may contain severer phase separation inside. Phase separation between polymer and fullerene happens during the film casting processes like spin casting, drop casting or inkjet printing, as the solvent dries. The kinetic parameters such as solvent evaporation rate, material precipitation rate and solution viscosity dominate the film formation process in the shorter time scope (1-60 seconds), while thermodynamic factors such as material miscibility and crystallinity will drive the morphological reorganization after film formation, which may have great impact on the long term stability of the BHJ and the corresponding devices.

To characterize the morphology of typically 100-200 nm thick BHJ active layer, whose feature is the size of 5-50nm, high resolution microscopy techniques are required. AFM as an accessible tool is widely used to characterize the surface topography, one of the most famous example is the solvent dependent morphology in MDMO-PPV: PCBM solar cells.[54] Some of its variants like Kelvin Probe Force Microscopy (KPFM), Electrostatic Force Microscopy (EFM) or photoconductive AFM (pcAFM) are used to correlate the surface morphology with surface work function, surface photo-excited charges, or photocurrent respectively.[55-57] Scanning Electron Microscopy (SEM) can visualize the lateral morphology via cross section mode[58] besides the surface morphology. Transmission Electron Microscopy (TEM) is the ideal tool to visualize the bulk morphology of BHJ because the transmitted and diffracted electron beam contains all the morphology information.[45] However, reconstructing the volume from the data is difficult. This was made possible by the Electron Tomography, also known as 3D TEM.[59,60] Until today, visualizing the morphology of BHJ is still a difficult job due to the high level requirement on equipment correction and calibration, high time consumption and possible sample deterioration issues.

1.4.3 Controlling the morphology

Due to the lack of understanding in BHJ morphology, the way of controlling it is very primitive. Furthermore, the control may not be generally effective because so many factors are involved in determining the morphology. For instance, thermal annealing and pre-aging of polymer solution can improve the performance of polythiophene fullerene system,[30,61] but they are not beneficial to many other systems.[62] Adding small amounts of high boiling point processing additive like 1,8-diiodooctane (DIO) into the host solvent in PCPDTBT:PCBM or PTB7:$PC_{71}BM$

can greatly improve the device efficiency by factor of 2,[32,63] but the long term and thermal stability of the BHJ morphology and possible DIO residue remains questionable. Solvent annealing is also a thermodynamic process like thermal annealing, which is not guaranteed to be helpful to devices.

Some of the methods that can systematically change the parameters are co-solvent system [64,65] and nano-imprinting,[66-68] but the device performance could be at most enhanced marginally. On the other hand, there are obvious disadvantages for these techniques. The working space for co-solvent may be specific to the donor-acceptor combination, while the nano-imprinting is tedious to implement and the ordered structure feature size achieved does not obviously outperform a decent BHJ structure.

1.5 Challenges and outlook

1.5.1 Energy loss in open circuit voltage

It should be noted that the energy loss during the photon to electron conversion is considerably large, e.g. from 2.3eV (average photon energy in the absorption region of P3HT: PCBM) to less than 0.6 eV, because the usable potential is less than the open circuit voltage. This more than 70% loss can be understood in three aspects. Firstly, the open circuit voltage is less than the virtual bandgap of the donor-acceptor combination, which is 1.0~1.1 eV for P3HT: PCBM.[38] Secondly, the open circuit voltage (V_{oc}) is associated with the charge transfer state (state 3 in **Figure 1.7**) rather than the charge separated state (associated with virtual bandgap, see state 4 in **Figure 1.7**) due to the strong Coulomb binding energy in organic solids. Finally, the Ohmic

contacts at the electrodes for the sake of efficient charge extraction inject charges near V_{oc}, which partially counterbalance the photocurrent and reduce the V_{oc}.

A severe intrinsic disadvantage of bulk-heterojunction is that the virtual bandgap is smaller than both bandgaps of the donor and acceptor components, which counts for not only the energy loss immediately after charge transfer, but also the inferior light absorption of bulk-heterojunction compared with a single junction whose bandgap equals to the virtual bandgap of the bulk-heterojunction. For instance, silicon has a virtual bandgap of 1.1eV and typical V_{oc} of 0.6V, but it absorbs much more light than P3HT: PCBM thus the short circuit current (J_{sc}) is much higher. Theoretical calculations[38] have predicted that to achieve optimum *PCE* of 10%, the LUMO offset needs to be as small as possible, just enough to provide the energy for charge separation, which is assumed to be around 0.3eV, and the bandgap of donor is 1.4-1.5eV (corresponding to 1.1~1.2eV virtual bandgap, similar to the result in a single junction[69]). However, Ohkita et al. claimed that the charge separation efficiency is strongly dependent on ΔG_{cs} for polythiophenes,[70,71] where ΔG_{cs} is the free energy difference for charge separation process:

$$\Delta G_{cs} = E_s \text{ (singlet)} - (IP_{donor} - EA_{acceptor}) + B.E. = LUMO_{donor} - LUMO_{acceptor} + B.E.$$

Where E_s is the singlet exciton energy, IP_{donor} is the ion potential of donor, $EA_{acceptor}$ is the electron affility of acceptor, B.E. is the polaron Coulomb binding energy, $LUMO_{donor}$ and $LUMO_{acceptor}$ are the LUMO for donor and acceptor, respectively.

In Ohkita's picture, ΔG_{cs} = 0.9 eV is just enough for P3HT: PCBM to efficiently separate electrons and holes. This trade-off between charge separation efficiency and energy loss during charge separation further limits the overall *PCE* of organic bulk heterojunction solar cells.

1.5.2 Tandem polymer solar cells

The discussion in last section indicates that the *PCE* may merely hit 10% with the optimization of material properties such as energy levels and absorption. In fact, the state-of-the-art single junction OPV devices have *PCE* of 6-8%, with the bandgap and absorption almost optimized.[32,33,72]

One way we can think of to efficiently utilize the broad spectrum of photons from the sun is to design a cascade structure, with each layer absorbing a small fraction of the incident light. However, designing materials with cascadic properties and fabricating multi-layer structure devices are rather challenging. One form of cascade structure is tandem cells, and engineering the thickness, absorption and current of the sub cell while minimizing the loss in the recombination layer is key to high performance tandem cells. Two sub cells are usually serially connected because the conductivity of the recombination layer cannot sustain large lateral current. This requires careful adjustment in sub cell thickness (light absorption) so that the currents generated in two sub cells are matched. The absorption of a sub cell in the stack of a tandem cell is different from that of a single junction cell of same composition, due to the change in environment and subsequently its transfer matrix, so optical modeling has to be done.

The state-of-the-art tandem cell shows 10.6% *PCE*,[34] which comprises of two state-of-the-art single junction cells with *PCE* of 6% and 8%, showing still some room for improvement.

1.6 The objective and outline of this thesis

As mentioned above, the current state of organic solar cell is far from commercialisation. The lack of understanding in the morphology and mechanism hinders further improvement of

device performance. Near perfect morphology has been shown but only for limited cases,[50,51] while it is a must in pursuit of higher device efficiency. This thesis focuses on organic bulk heterojunction solar cells, especially in the aspects of controlling the morphology, improving the device performance and understanding the device physics.

In Chapter 2, accurate determination of organic solar cells performance and calibration of solar simulator will be discussed, along with the calibration of silicon photodiode and spectrograph system.

In Chapter 3, a novel molecular infiltration method to fabricate polymer-based solar cells using sterically hindered bis(fluorophenyl azide)s (s-FPAs or crosslinker) is introduced. The donor polymer film is first deposited and photocrosslinked with versatile high-efficiency nitrene chemistry, then the molecular acceptor is "doped" into this film by contact with its solution under precise control. The morphologies of these devices has been characterized by AFM and TEM. The 2D *PCE* map of regioregular poly(3-hexylthiophene) (rrP3HT):phenyl-C61-butyrate methyl ester (PCBM) solar cells as a function of the effective amount of rrP3HT and PCBM in the film was obtained for the first time. The results reveal a "ridge of efficiency" that coincides with the 1:0.8 P3HT: PCBM weight ratio line comprising islands of particularly high efficiencies at both low and high film thicknesses (maximum *PCE*, 4.2%). The *PCE* are generally 20-30% higher than blend films of the same composition made by conventional spin-casting. Further analysis shows that the internal quantum efficiency (*IQE*) of the crosslinked devices are near to unity across a wide range of thickness and composition, which is a special advantage of the crosslinking method.

Chapter 4 presents the built-in potential (V_{bi}) characterization of the crosslinked network devices and conventional blend devices by electroabsorption spectroscopy (Stark spectroscopy). The accurate measurement of V_{bi} is fundamental to the understanding of the

device physics and possible loss mechanism, as described by the drift-diffusion model in Chapter 5.

Chapter 5 incorporates the optical modeling and electrical modeling to understand the device physics and loss mechanism of P3HT: PCBM solar cells. Most parameters in the model are independently measured by experiments, and the number of fitting parameters is kept as small as possible. The match of modeling results and experimental data indicates that the donor–acceptor morphology in crosslinked network P3HT: PCBM solar cell is identical across a wide range of composition and thickness. Amongst the new insights that have thus been achieved includes how the power-conversion-efficiency landscape varies with photoactive layer composition and thickness, and the role of optical interference, asymmetric carrier mobilities, carrier recombination, and injection boundary conditions in determining the optimal structure for organic solar cells.

1.7 Abbreviations

For clarity, we have listed some abbreviations which are commonly used in the field. **Table 1.1** summarizes the abbreviations used throughout this thesis.

Table 1.1: List of most common abbreviations used throughout the thesis

Symbol	description
A	Acceptor
a	Electron-hole pair distance
AM1.5	Air mass 1.5
BHJ	Bulk heterojunction
D	Donor
Dn(p)	Electron (hole) diffusion coefficient
DSSC	Dye-sensitized solar cell
EQE	External quantum efficiency

FF	Fill factor
G	Generation rate of bound electron-hole pairs
HOMO	Highest occupied molecular orbital
I	Incident light intensity
IQE	Internal quantum efficiency
ITO	Indium-tin-oxide
Jn(p)	Electron (hole) current density
Jph	Net photocurrent density
Jsc	Short-circuit current density
kB	Boltzmann's constant
LUMO	Lowest unoccupied molecular orbital
MDMO-PPV	Poly(2-methoxy-5-(3',7'-dimethyl octyloxy)-p-phenylene vinylene)
N	Effective density of states of valance and conduction bands
n(p)	Electron (hole) density
OSC	Organic semiconductors
P	Electron-hole pair dissociation probability
PAL	Photo active layer
PCBM	Phenyl-C61-butyric acid methyl ester
PCE	power conversion efficiency
PCPDTBT	Poly[2,1,3-benzothiadiazole-4,7-diyl[4,4-bis(2-ethylhexyl)-4H-cyclopenta[2,1-b:3,4-b']dithiophene-2,6-diyl]]
PEDT: PSS	Poly(3,4-ethylene dioxythiophene):poly(styrene sulfonate)
PPV	Poly(phenylene vinylene)
PV	Photovoltaic
q	Elementary charge
R	Recombination rate of charge carriers
rrP3HT	Regioregular Poly(3-hexylthiophene)
SCL	Space-charge-limited
s-FPAs	Sterically hindered bis(fluorophenyl azide)s
T	Absolute temperature
U	Net generation rate of free carriers
Va	Applied voltage
Vbi	Built-in voltage
Voc	Open-circuit voltage
Vt	Thermal voltage
z	Position
ε	Dielectric constant
μn(p)	Electron (hole) mobility

1.8 References

1 http://en.wikipedia.org/wiki/Electricity_pricing, (2012).

2 Chapin, D., Fuller, C. & Pearson, G. A New Silicon p ‐ n Junction Photocell for Converting Solar Radiation into Electrical Power. *J. Appl. Phys.* **25**, 676 (1954).

3 Green, M. A., Emery, K., Hishikawa, Y., Warta, W. & Dunlop, E. D. Solar cell efficiency tables (version 39). *Progress in Photovoltaics: Research and Applications* **20**, 12-20 (2012).

4 Green, M. A. Solar cells: operating principles, technology, and system applications. *Englewood Cliffs, NJ, Prentice-Hall, Inc., 1982. 288 p.* **1** (1982).

5 Shockley, W. & Queisser, H. J. Detailed balance limit of efficiency of p ‐ n junction solar cells. *J. Appl. Phys.* **32**, 510-519 (1961).

6 O'regan, B. & Gratzel, M. A low-cost, high-efficiency solar cell based on dye-sensitized colloidal TiO2 films. *Nature* **353**, 737-740 (1991).

7 http://www.g24i.com/press,new-record-set-for-recycling-indoor-light-to-electricity,225.html, (2012).

8 Shirakawa, H., Louis, E. J., MacDiarmid, A. G., Chiang, C. K. & Heeger, A. J. Synthesis of electrically conducting organic polymers: halogen derivatives of polyacetylene,(CH) x. *J. Chem. Soc., Chem. Commun.*, 578-580 (1977).

9 Burroughes, J. H. *et al.* Light-emitting diodes based on conjugated polymers. *Nature* **347**, 539-541 (1990).

10 Sirringhaus, H. Device physics of solution ‐ processed organic field ‐ effect transistors. *Adv. Mater.* **17**, 2411-2425 (2005).

11 Burroughes, J. H., Jones, C. A. & Friend, R. H. New semiconductor device physics in polymer diodes and transistors. *Nature* **335**, 137-141 (1988).

12 Blom, P. W. M., Mihailetchi, V. D., Koster, L. J. A. & Markov, D. E. Device physics of polymer: fullerene bulk heterojuction solar cells. *Adv. Mater.* **19**, 1551-1566 (2007).

13 Choi, M. C., Kim, Y. & Ha, C. S. Polymers for flexible displays: From material selection to device applications. *Prog. Polym. Sci.* **33**, 581-630 (2008).

14 Someya, T. *et al.* Conformable, flexible, large-area networks of pressure and thermal sensors with organic transistor active matrixes. *PROC. NATL. ACAD. SCI. USA* **102**, 12321 (2005).

15 Mabeck, J. T. & Malliaras, G. G. Chemical and biological sensors based on organic thin-film transistors. *Anal. Bioanal. Chem.* **384**, 343-353 (2006).

16 Bässler, H. Localized states and electronic transport in single component organic solids with diagonal disorder. *Phys. Status Solidi B* **107**, 9-54 (1981).

17 Bässler, H. Charge transport in disordered organic photoconductors: a Monte Carlo simulation study. *Phys. Status Solidi B* **175**, 15-56 (1993).

18 Gustafsson, G. *et al.* Flexible light-emitting diodes made from soluble conducting polymers. *Nature* **357**, 477-479 (1992).

19 http://www.sumitomo-chem.co.jp/english/pled/exhibition.html, (2012).

20 Shaheen, S. E., Radspinner, R., Peyghambarian, N. & Jabbour, G. E. Fabrication of bulk heterojunction plastic solar cells by screen printing. *Appl. Phys. Lett.* **79**, 2996-2998 (2001).

21 Krebs, F. C. Roll-to-roll fabrication of monolithic large-area polymer solar cells free from indium-tin-oxide. *Sol. Energ. Mat. Sol. Cells* **93**, 1636-1641 (2009).

22 Barth, S. & Bässler, H. Intrinsic photoconduction in PPV-type conjugated polymers. *Phys. Rev. Lett.* **79**, 4445-4448 (1997).

23 Da Costa, P. G. & Conwell, E. Excitons and the band gap in poly (phenylene vinylene). *Phys. Rev. B* **48** (1993).

24 Marks, R., Halls, J., Bradley, D., Friend, R. & Holmes, A. The photovoltaic response in poly (p-phenylene vinylene) thin-film devices. *Journal of Physics: Condensed Matter* **6**, 1379 (1994).

25 Tang, C. Two‐layer organic photovoltaic cell. *Appl. Phys. Lett.* **48**, 183-185 (1986).

26 Sariciftci, N. S., Smilowitz, L., Heeger, A. J. & Wudl, F. Photoinduced electron transfer from a conducting polymer to buckminsterfullerene. *Science* **258**, 1474-1476 (1992).

27 Hummelen, J. C. *et al.* Preparation and characterization of fulleroid and methanofullerene derivatives. *The Journal of Organic Chemistry* **60**, 532-538 (1995).

28 Yu, G., Gao, J., Hummelen, J., Wudl, F. & Heeger, A. Polymer photovoltaic cells: enhanced efficiencies via a network of internal donor-acceptor heterojunctions. *Science* **270**, 1789-1791 (1995).

29 Halls, J. J. M. *et al.* Efficient photodiodes from interpenetrating polymer networks. *Nature* **376**, 498-500 (1995).

30 Padinger, F., Rittberger, R. S. & Sariciftci, N. S. Effects of postproduction treatment on plastic solar cells. *Adv. Funct. Mater.* **13**, 85-88 (2003).

31 Peet, J. *et al.* Efficiency enhancement in low-bandgap polymer solar cells by processing with alkane dithiols. *Nature Mater.* **6**, 497-500 (2007).

32 Liang, Y. *et al.* For the bright future—bulk heterojunction polymer solar cells with power conversion efficiency of 7.4%. *Adv. Mater.* **22**, E135-E138 (2010).

33 He, Y., Chen, H. Y., Hou, J. & Li, Y. Indene− C60 Bisadduct: A New Acceptor for High-Performance Polymer Solar Cells. *J. Am. Chem. Soc.* **132**, 1377-1382 (2010).

34 Li, G., Zhu, R. & Yang, Y. Polymer solar cells. *Nature Photon.* **6**, 153-161 (2012).

35 Groenendaal, L., Jonas, F., Freitag, D., Pielartzik, H. & Reynolds, J. R. Poly (3, 4-ethylenedioxythiophene) and its derivatives: past, present, and future. *Adv. Mater.* **12**, 481-494 (2000).

36 Huang, J. *et al.* Investigation of the Effects of Doping and Post‐Deposition Treatments on the Conductivity, Morphology, and Work Function of Poly (3, 4‐ethylenedioxythiophene)/Poly (styrene sulfonate) Films. *Adv. Funct. Mater.* **15**, 290-296 (2005).

37 Ouyang, J., Chu, C. W., Chen, F. C., Xu, Q. & Yang, Y. High‐Conductivity Poly (3, 4‐ethylenedioxythiophene): Poly (styrene sulfonate) Film and Its Application in Polymer Optoelectronic Devices. *Adv. Funct. Mater.* **15**, 203-208 (2005).

38 Scharber, M. C. *et al.* Design rules for donors in bulk-heterojunction solar cells - towards 10% energy-conversion efficiency. *Adv. Mater.* **18**, 789-794 (2006).

39 Brabec, C. J., Sariciftci, N. S. & Hummelen, J. C. Plastic solar cells. *Adv. Funct. Mater.* **11**, 15-26 (2001).

40 Hoppe, H. & Sariciftci, N. S. Organic solar cells: An overview. *J. Mater. Res* **19**, 1925 (2004).

41 Halls, J., Pichler, K., Friend, R., Moratti, S. & Holmes, A. Exciton diffusion and dissociation in a poly (p-phenylenevinylene)/C60 heterojunction photovoltaic cell. *Appl. Phys. Lett.* **68**, 3120 (1996).

42 Brabec, C. J. *et al.* Tracing photoinduced electron transfer process in conjugated polymer/fullerene bulk heterojunctions in real time. *Chem. Phys. Lett.* **340**, 232-236 (2001).

43 Chirvase, D., Parisi, J., Hummelen, J. & Dyakonov, V. Influence of nanomorphology on the photovoltaic action of polymer–fullerene composites. *Nanotechnol.* **15**, 1317 (2004).

44 Hoppe, H. *et al.* Nanoscale Morphology of Conjugated Polymer/Fullerene ‐ Based Bulk ‐ Heterojunction Solar Cells. *Adv. Funct. Mater.* **14**, 1005-1011 (2004).

45 Yang, X. *et al.* Nanoscale morphology of high-performance polymer solar cells. *Nano. Lett.* **5**, 579-583 (2005).

46 Cheyns, D. *et al.* Analytical model for the open-circuit voltage and its associated resistance in organic planar heterojunction solar cells. *Phys. Rev. B* **77**, 165332 (2008).

47 Howard, I. A., Mauer, R., Meister, M. & Laquai, F. Effect of morphology on ultrafast free carrier generation in polythiophene: fullerene organic solar cells. *J. Am. Chem. Soc.* (2010).

48 Mandoc, M., Kooistra, F., Hummelen, J., De Boer, B. & Blom, P. Effect of traps on the performance of bulk heterojunction organic solar cells. *Appl. Phys. Lett.* **91**, 263505 (2007).

49 Li, G. *et al.* High-efficiency solution processable polymer photovoltaic cells by self-organization of polymer blends. *Nature Mater.* **4**, 864-868 (2005).

50 Park, S. H. *et al.* Bulk heterojunction solar cells with internal quantum efficiency approaching 100&percnt. *Nature Photon.* **3**, 297-302 (2009).

51 Chen, H. Y. *et al.* Polymer solar cells with enhanced open-circuit voltage and efficiency. *Nature Photon.* **3**, 649-653 (2009).

52 He, X. *et al.* Formation of nanopatterned polymer blends in photovoltaic devices. *Nano Letters* **10**, 1302-1307 (2010).

53 Snaith, H. J. *et al.* Self-organization of nanocrystals in polymer brushes. Application in heterojunction photovoltaic diodes. *Nano Lett.* **5**, 1653-1657 (2005).

54 Shaheen, S. E. *et al.* 2.5% efficient organic plastic solar cells. *Appl. Phys. Lett.* **78**, 841 (2001).

55 Hoppe, H. *et al.* Kelvin probe force microscopy study on conjugated polymer/fullerene bulk heterojunction organic solar cells. *Nano Lett.* **5**, 269-274 (2005).

56 Coffey, D. C. & Ginger, D. S. Time-resolved electrostatic force microscopy of polymer solar cells. *Nature Mater.* **5**, 735-740 (2006).

57 Coffey, D. C., Reid, O. G., Rodovsky, D. B., Bartholomew, G. P. & Ginger, D. S. Mapping local photocurrents in polymer/fullerene solar cells with photoconductive atomic force microscopy. *Nano Lett.* **7**, 738-744 (2007).

58 Hoppe, H. *et al.* Nanoscale Morphology of Conjugated Polymer/Fullerene ‐ Based Bulk ‐ Heterojunction Solar Cells. *Adv. Funct. Mater.* **14**, 1005-1011 (2004).

59 Friedrich, H., de Jongh, P. E., Verkleij, A. J. & de Jong, K. P. Electron tomography for heterogeneous catalysts and related nanostructured materials. *Chemical Reviews* **109**, 1613-1629 (2009).

60 van Bavel, S. S., Bärenklau, M., de With, G., Hoppe, H. & Loos, J. P3HT/PCBM bulk heterojunction solar cells: impact of blend composition and 3D morphology on device performance. *Adv. Funct. Mater.* **20**, 1458-1463 (2010).

61 Kim, Y. *et al.* Device annealing effect in organic solar cells with blends of regioregular poly (3-hexylthiophene) and soluble fullerene. *Appl. Phys. Lett.* **86**, 063502-063502-063503 (2005).

62 Mühlbacher, D. *et al.* High photovoltaic performance of a low ‐ bandgap polymer. *Adv. Mater.* **18**, 2884-2889 (2006).

63 Peet, J. *et al.* Efficiency enhancement in low-bandgap polymer solar cells by processing with alkane dithiols. *Nature Mater.* **6**, 497-500 (2007).

64 Campbell, A. R. *et al.* Low-temperature control of nanoscale morphology for high performance polymer photovoltaics. *Nano Lett.* **8**, 3942-3947 (2008).

65 Yao, Y., Hou, J., Xu, Z., Li, G. & Yang, Y. Effects of solvent mixtures on the nanoscale phase separation in polymer solar cells. *Adv. Funct. Mater.* **18**, 1783-1789 (2008).

66 He, X. *et al.* Formation of nanopatterned polymer blends in photovoltaic devices. *Nano Lett.* **10**, 1302-1307 (2010).

67 Cheyns, D. *et al.* Nanoimprinted semiconducting polymer films with 50 nm features and their application to organic heterojunction solar cells. *Nanotechnol.* **19**, 424016 (2008).

68 Kim, M. S. *et al.* Flexible conjugated polymer photovoltaic cells with controlled heterojunctions fabricated using nanoimprint lithography. *Appl. Phys. Lett.* **90**, 123113-123113-123113 (2007).

69 Shockley, W. & Queisser, H. J. Detailed balance limit of efficiency of p‐n junction solar cells. *J. Appl. Phys.* **32**, 510-519 (1961).

70 Clarke, T. M., Ballantyne, A. M., Nelson, J., Bradley, D. D. C. & Durrant, J. R. Free energy control of charge photogeneration in polythiophene/fullerene solar cells: The influence of thermal annealing on P3HT/PCBM blends. *Adv. Funct. Mater.* **18**, 4029-4035 (2008).

71 Ohkita, H. *et al.* Charge carrier formation in polythiophene/fullerene blend films studied by transient absorption spectroscopy. *J. Am. Chem. Soc.* **130**, 3030-3042 (2008).

72 Chu, T. Y. *et al.* Bulk heterojunction solar cells using thieno [3, 4-c] pyrrole-4, 6-dione and dithieno [3, 2-b: 2′, 3′-d] silole copolymer with a power conversion efficiency of 7.3%. *J. Am. Chem. Soc.* **133**, 4250-4253 (2011).

Chapter 2. Accurate characterization of organic solar cells and calibration of solar simulator

In this chapter, we describe the rationale to calibrate the silicon photodiode and spectrograph, in order to characterize the solar simulator. We also describe the theory to correct the spectral mismatch factor. These are essential to accurate characterization of organic solar cell devices.

The characterization of bulk-heterojunction solar cells is usually conducted with the existing standards established by the inorganic photovoltaic community. The most important performance figure-of-merit for solar cell is the power conversion efficiency (*PCE*), which is the ratio of the maximum electrical power output to the incident irradiance, should be measured under (or translated to) standard reporting condition (SRC): AM 1.5 (air mass 1.5) reference solar spectrum, 1000Wm^{-2} irradiance and 25°C cell temperature. However, conditions such as the AM 1.5 spectral distribution are very difficult and expensive to achieve, which require outdoors measurements or a very well tuned solar simulator, so the actual measurement condition will be different and the translation of the results is necessary.[1,2]

Another important parameter is the external quantum efficiency ($EQE(\lambda)$) or spectral responsivity ($SR(\lambda)$). The term *EQE* is defined by the number of electrons generated by every incident photon, while *SR* describes the current generation per unit power incidence:

$$SR(\lambda) = \frac{q\lambda}{hc}\mathrm{EQE}(\lambda) \approx \mathrm{EQE}(\lambda) \cdot \lambda(\mathrm{in\ nm})/1240$$

Where q is elementary charge, h is the Plank constant, and c is the speed of light and λ is the wavelength of incident photon.

2.1 AM1.5 standard reporting condition

The solar radiation closely matches a 5800K black body radiator at the outmost of the atmosphere, as shown in **Figure 2.1**. This spectrum is also termed as AM0, and the coefficient represents the optical path length through the Earth's atmosphere, in the unit of the thickness of the atmosphere. Considering the axial tilt, different time of the day and position on earth, the typical average attenuation is equivalent to 1.5 times of the atmosphere thickness or AM1.5 when the sunlight reaches the earth. Besides scattering, some cavities are created in the spectrum by the absorption of certain components of the atmosphere, such as ozone, water and carbon dioxide.

There are a few AM1.5 spectrum standards, and they are also evolving with time due to more and more accurate measurements and possibly climate change, etc. The latest and most widely adopted one is ASTM G173-03. [3]

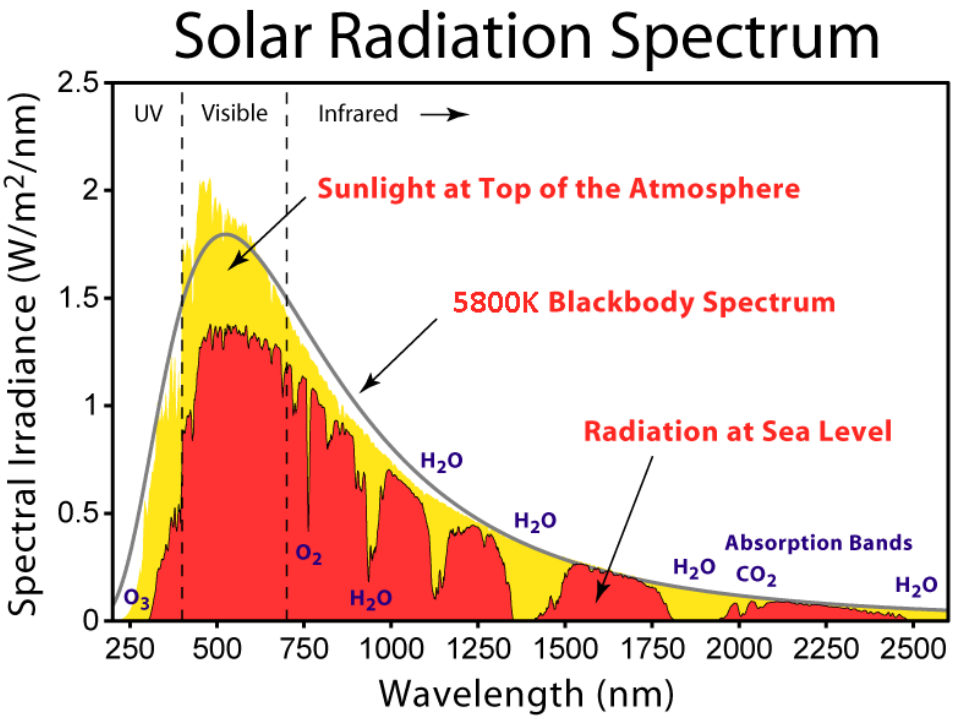

Figure 2.1 Solar irradiance spectrum above atmosphere and at surface. The effective temperature, or black body temperature, of the Sun (5800 K) is the temperature a black body of the same size must have to yield the same total emissive power.

On the other hand, it is not practical to always characterize the solar cells outdoors, or easily build a perfect AM1.5 lamp source. The commonly used solar simulator is xenon arc lamp equipped with several filters, which can simulate the natural sunlight well. Due to the discrepancy from standard AM1.5 and various grades (classified by the spectral mismatch, uniformity and temporal stability, etc), the simulators have to be calibrated to accurately characterize the solar cells. To communicate between different solar simulators, calibrated reference solar cells are also required. The key indices for a reference cell are the *SR* and short circuit current (I_{sc}) under a calibrated solar simulator source. The greater the

resemblance between the reference cell and the device under test (DUT), and also between the solar simulator spectrum and the standard AM 1.5, more accurate the measurement will be.

2.2 *PCE* and *EQE* measurements of organic solar cells

The *PCE* of a solar cell device can be extracted from the current density-voltage (J-V) characteristics under the illumination of a home-made solar simulator (165W Xenon lamp + AM1.5G solar simulator filter), which can be measured by Keighley 4200 SCS system. The measurement is done in a vacuum chamber (pressure < 10^{-4} mbar) to protect the photoactive layer and the low work function cathode. The active area of a device pixel is usually determined to be 0.0429 ± 0.0002 cm^2 by the area of the cathode.

The typical J-V curves of a bulk heterojunction solar cell in the dark (red dotted line) and under illumination (orange solid line) are shown in **Figure 2.2**, as well as the power output curve P=J*V (green dash line).

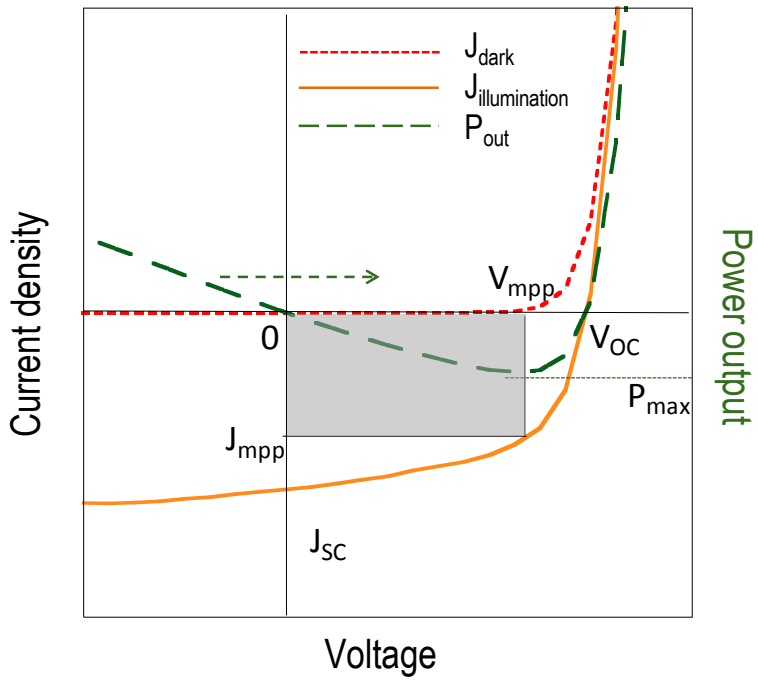

Figure 2.2 Typical J-V curves of a solar cell device in the dark (red dotted line) and illumination (orange solid line) conditions, and power output curve (green dash line). The short circuit current (J_{sc}), open-circuit voltage (V_{oc}) and maximum output power (P_{max}, shaded area) are shown.

The dark J-V curve shows typical diode characteristics, and the illuminated J-V curve is shifted down. The difference is the photo-generated current. To obtain the maximum output power, the solar cell should work at the maximum power point voltage (V_{mpp}, as shown in **Figure 2.2**). The *PCE* can be extracted as

$$PCE = \frac{P_{max}}{P_{incident}} = \frac{V_{mpp} \cdot J_{mpp}}{P_{incident}} = \frac{V_{OC} \cdot J_{SC} \cdot FF}{P_{incident}}$$

where *FF* is the fill factor:

$$FF = \frac{V_{mpp} \cdot J_{mpp}}{V_{OC} \cdot J_{SC}}$$

These indices provide a overview of the solar cell performance, which depend not only on the quality of the cell (composition, thickness and morphology[4,5] of the photoactive layer, the

electrodes used[6,7]) and the external stimulation (incident light intensity,[8,9] temperature[10]) but also the detailed spectrum of the incident light, simply because of the wavelength dependent responsivity ($SR(\lambda)$) of the solar cell.

In order to report the accurate *PCE* under the standard AM1.5 spectrum, the spectral mismatch factor has to be corrected. In order to do that, one has to know the solar simulator spectrum quite accurately, and in order to measure the solar simulator spectrum, one needs at least a calibrated silicon photodiode and a calibrated spectrograph system.

The *EQE* (*SR*) of the solar cell is measured on the same rig. Monochromatic light beam is generated from a tungsten lamp (50W) and a monochromator (Newport Cornerstone 260 1/4 m, F/ 3.9, model# 74100), then directed and focused onto the pixel. The beam size is smaller than the device pixel. The proper alignment of the pixel is achieved by maximizing the photovoltage (V_{pd}) measured with a multi-meter via adjusting the XYZ position of the pixel under illumination of monochromatic light (such as 550nm). A transimpedance amplifier (10M gain) is used to convert and amplify the photocurrent (I_{sc}) to voltage due to the low incident light intensity (~0.01mWcm^{-2}).

After alignment, recording of the I_{sc} (V_{pd}) of the device pixel by a Keighley 2400 source meter and the stepwise wavelength scan of the monochromator are controlled and coordinated by a Labview program.

A silicon photodiode (SiPD) with known quantum efficiency (QE) characteristics is also placed under the monochromatic light to determine the incident light intensities at different wavelengths.

$EQE_{cell}(\lambda) = QE_{SiPD}(\lambda) * Isc_{cell}(\lambda) / Isc_{SiPD}(\lambda)$,

where I_{sc} can be calculated from V_{pd}, gain and illuminated area.

2.3 Calibration of the silicon photodiode

The quantum efficiency (QE) or *SR* of a silicon photodiode (OPT301M from Burr Brown, amplifier circuit and a zero adjuster) has been calibrated in house. A calibrated silicon photodiode (SiPD) can be considered as a reference cell with zero bias, and can be used to gauge the power of solar simulator.

The reference lamp is a calibrated quartz-tungsten-halogen lamp (Newport 63358, traceable to NIST standard), powered with a constant current of 6.5A, and an output power of 45W. Its wavelength range is 250-2400nm, suitable to calibrate both Si photodiode and InGaAs photodiode. It has a linear shape bulb, while the filament can be regarded as a point source from 1.25 meters away (Viewing angle < 0.02/1.25 = 0.016 rad = 0.92'(°)).

The wavelength dependent irradiance spectrum is provided by the manufacturer. The empirical expression and the spectrum graph are shown below in **Figure 2.3**.

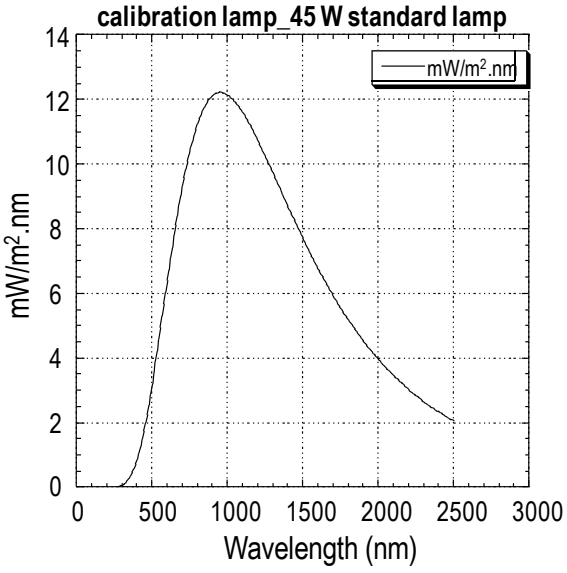

45W QTH calibrated lamp
Model number: Oriel 63358
serial number: 7-1726

Expression for the irradiance (mW/m^2 nm) :
$x^{-5}*\exp(m1+m2/x)*(m3+m4/x+m5/x^2+m6/x^3+m7/x^4)$,

Where wavelength x=nm;
m1=41.8034809540978;
m2=-4776.1389929453;
m3=0.825361064462176;
m4=421.249674888088;
m5=-319156.334268857;
m6=90288159.8083707;
m7=-9519785430.83809;

Figure 2.3 Irradiance spectrum of a calibrated quartz-tungsten-halogen lamp at a distance of 0.5m.

The calibration setup is as following (**Figure 2.4**): the bulb is vertically placed at around 0.4 meters high on the optical table. The photodiode to be calibrated (PTC) is placed 1.25 meters away at the same height, facing the lamp, and housed in a black paper box with a small aperture, which shields the room light and other scattered and reflected light except the light directly from the reference lamp. Some black paper is placed vertically between the PTC and the reference lamp to further reduce the reflection from the surface of the optical table.

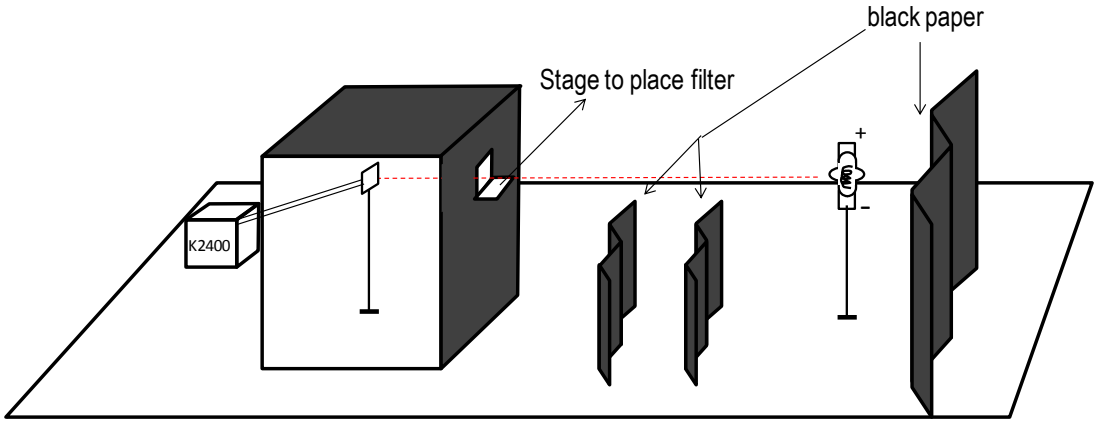

Figure 2.4 Silicon photodiode calibration setup.

A complete series of band pass filters are put in front of the SiPD so that it responds to a small fraction of light (10nm width or so) at a time. Assuming the QE of this fraction of light is a constant, whose validity can be testified by the result, it can be calculated by dividing the photocurrent by the incident photon flux. The SiPD is integrated with an amplifier with 4-stage trans-impedance gain from 10^4 to 10^7, so the photocurrent is converted to voltage and measured by a Keighley 2400 source meter. On the other hand the incident photon flux is computed from the reference lamp spectrum and the transmission functions of the filters. In this way, the QE at certain wavelengths can be determined and a smooth QE curve is obtained.

The results are shown in **Figure 2.5**. By integrating the product of QE(λ) of SiPD and photon flux(λ) of reference lamp, we can reproduce the photocurrent within 3% error to the measured data, which confirms that the method to determine the QE of the SiPD is valid.

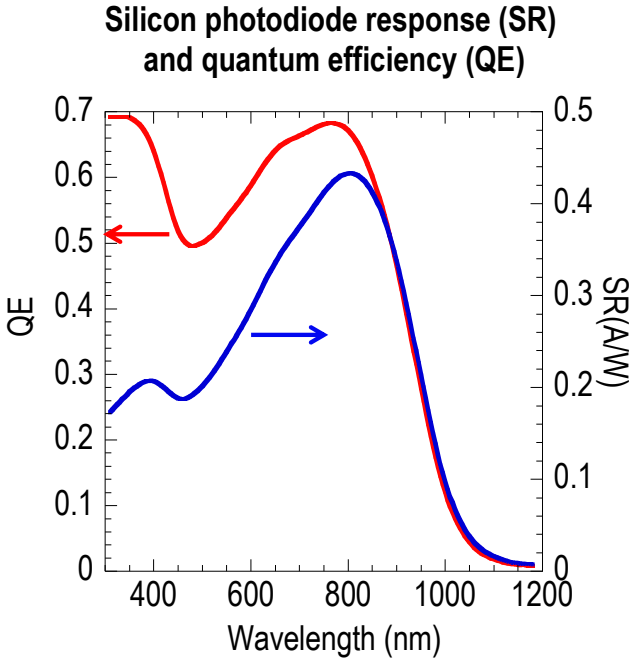

Figure 2.5 Silicon photodiode response (*SR*) and quantum efficiency (QE)

2.4 Wavelength calibration of the InstaSpec X CCD imaging spectrograph

The Oriel InstaSpec X CCD (model# 78236) coupled with MS127i Imaging Spectrograph (model# 77480) can measure the irradiance spectrum of a light source accurately and quickly with its cooled CCD sensors. This CCD system works at two different wavelength ranges for the purpose of higher accuracy: 300-800nm and 600-1200nm with tunable gratings.

Hg-Ar lamp has been employed to calibrate the wavelength of the spectrograph (grating position). The ideal match (error< 0.5nm) of the distinct spectral lines on the spectrograph and

the Hg-Ar lamp indicates a successful wavelength calibration. The spectral lines are shown in the following **Figure 2.6** for two wavelength ranges.

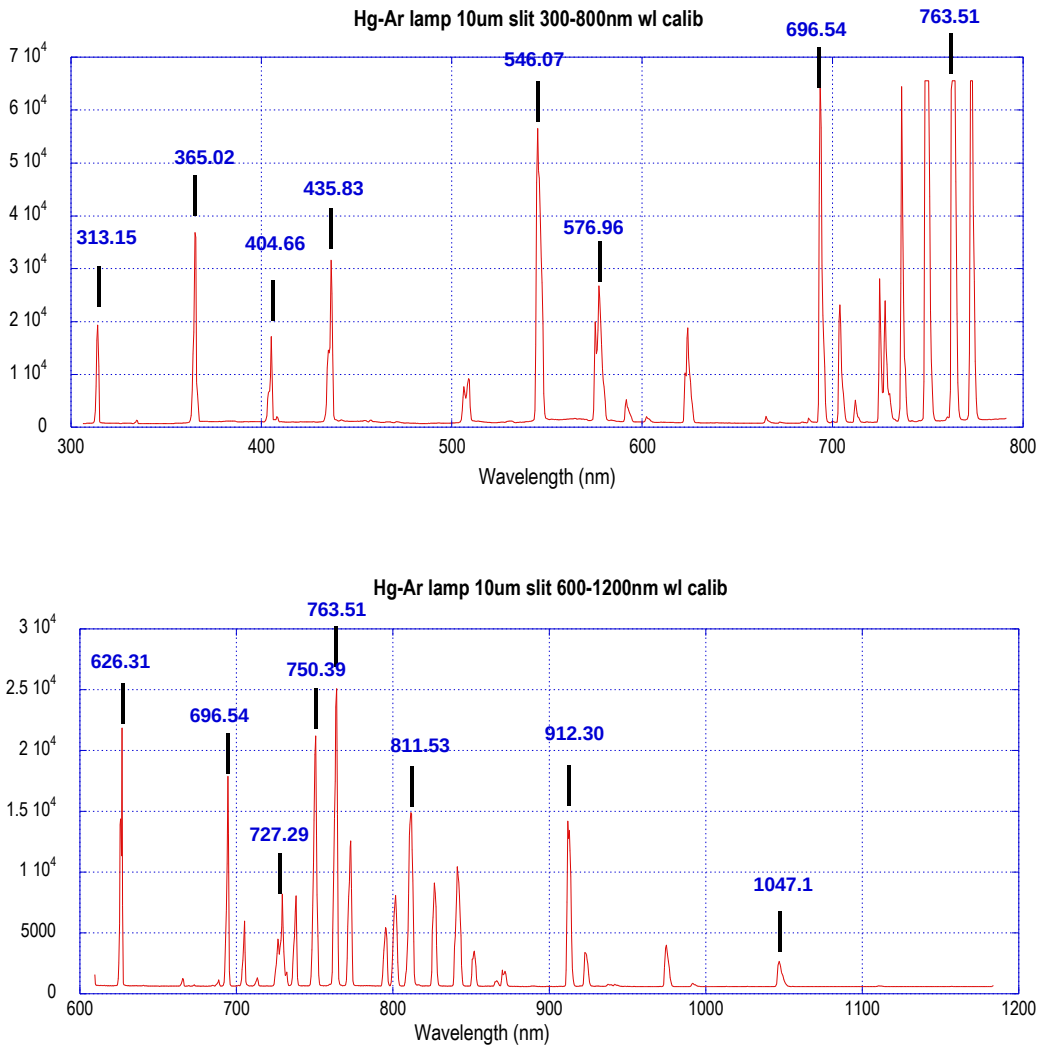

Figure 2.6 Hg-Ar lamp spectral lines

A calibrated spectrograph system can be used to calibrate the wavelength of other equipments such as monochromators.

2.5 Responsivity calibration of InstaSpec X CCD system

The InstaSpec X CCD system converts incident light to electrons with some built-in gain function, the relationship between incident power or photon flux and the electron counts needs to be established so that the CCD system can be used to characterize the absolute intensity of a light source spectrum.

Simply replace the PTC in **Figure 2.4** with a SMA optical fiber connector, which can be connected with the CCD system via an optical fiber (D=1mm). The black paper box can be removed because the optical fiber is an enclosed system. In this way, the irradiance spectrum in **Figure 2.3** can be projected onto the CCD system, represented by a diagram of electron counts per second at each CCD channel, as shown in **Figure 2.7**. Assuming the linear response in certain light intensity range, one can derive the irradiance spectrum easily from the counts per second recorded by the CCD system, **Figure 2.3** and **Figure 2.7**. Take note that **Figure 2.3** corresponds to a distance of 0.5 meter from the calibrated lamp, and the irradiance at 1.25 meter distance is scaled inverse proportionally to the square of distance. (Scaling factor $=(0.5/1.25)^2 = 0.16$, experimentally testified.)

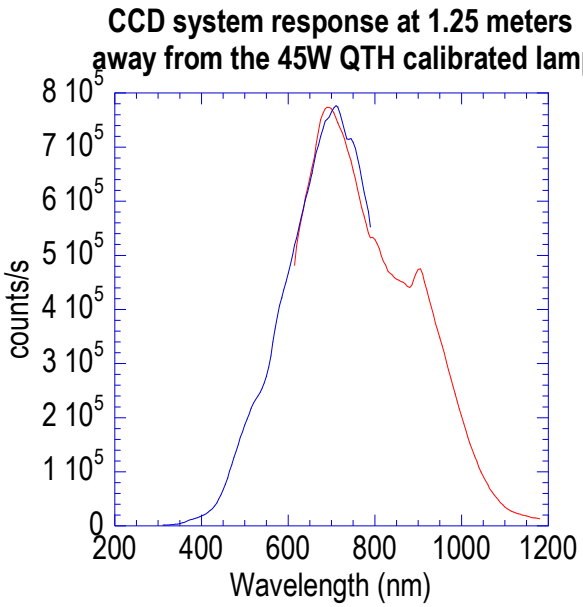

Figure 2.7 CCD system (including the optical fibre) response at 1.25 meters away from the 45W QTH calibrated lamp. The overlapped wavelength region shows good consistency before and after changing the grating. Dark counts are subtracted from the total counts, first order scattering from neighbouring channels is corrected.

2.6 Characterization of a home-made solar simulator with InstaSpec X CCD system

With the calibrated InstaSpec X CCD system and SiPD, one can in principle determine any spectrum within the measuring range. Firstly, the photodiode voltage (V_{pd}) response of our calibrated SiPD to the standard AM1.5 spectrum is estimated to be 11.5V, assuming linear responsivity at all light intensities:

$$\mathrm{V_{pd}} = \int_{\lambda} \mathrm{I_{AM1.5}}(\lambda) \cdot SR(\lambda) \cdot A \cdot G \cdot \mathrm{d}\,\lambda$$

Where $\mathrm{I_{AM1.5}}(\lambda)$ is the standard AM1.5 irradiance spectrum, $SR(\lambda)$ the spectral responsivity of the calibrated SiPD as shown in **Figure 2.5**, A the active area of the SiPD

(2.29mm*2.29mm), *G* the impedance gain (10^4 Ohm), integration range is the working range of the SiPD (300-1100nm).

The home-made solar simulator is tuned to also give V_{pd} =11.5V, so that the total irradiance is close to one AM1.5 sun. However, the light from the simulator is so strong that the CCD system saturates even at the minimum exposure time possible. A compromised solution is to place an OD filter in front of the fiber inlet and the CCD response can be recorded as C(λ). Let us denote the irradiance of calibrated QTH lamp as $I_0(\lambda)$ (**Figure 2.3***0.16), the CCD response to this irradiance as $C_0(\lambda)$ (**Figure 2.7**), and transmission of the OD filter as T(λ). Then the irradiance of the solar simulator can then be derived as:

$I(\lambda) = I_0(\lambda)/ C_0(\lambda)* C(\lambda)/T(\lambda)$,

the results are shown in **Figure 2.8** for both glass filter and metal coated filter.

Irradiance spectrum for two different filters is the same, but their intensity is twice that of the standard AM 1.5 spectrum, which means V_{pd0}=23V if the SiPD response is linear.

We soon realized that the problem is the non-linear response of SiPD to the irradiance at the level of 0.1 sun or more. With a series of OD filters, the dependence of V_{pd} on the light intensity of a 0.4mW 514nm laser (Spectra-physics 2017) is established in **Figure 2.9**. The laser was chosen over the solar simulator for its collimation and monochromaticity so that the T(λ) is not a variable anymore.

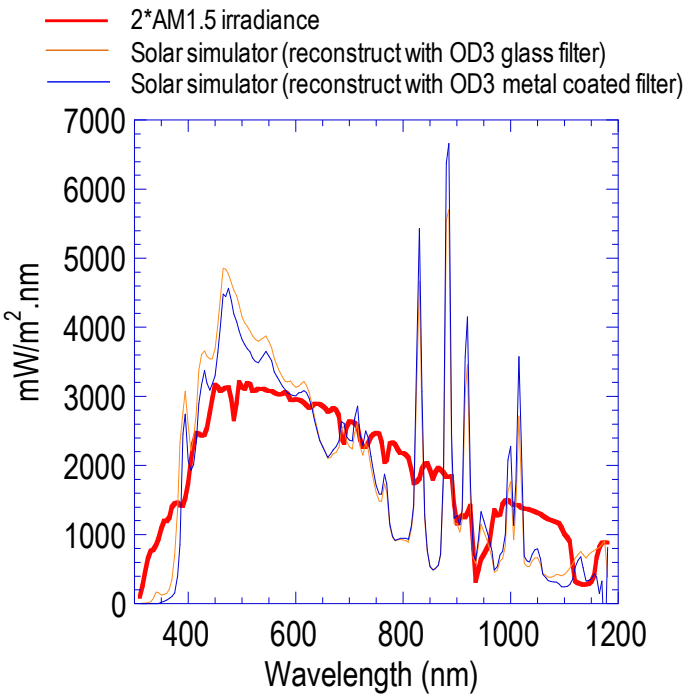

Figure 2.8 Irradiance spectrum of AM1.5 and home-made solar simulator. There are many undesirable sharp xenon atomic transitional peaks within 800-1100nm.

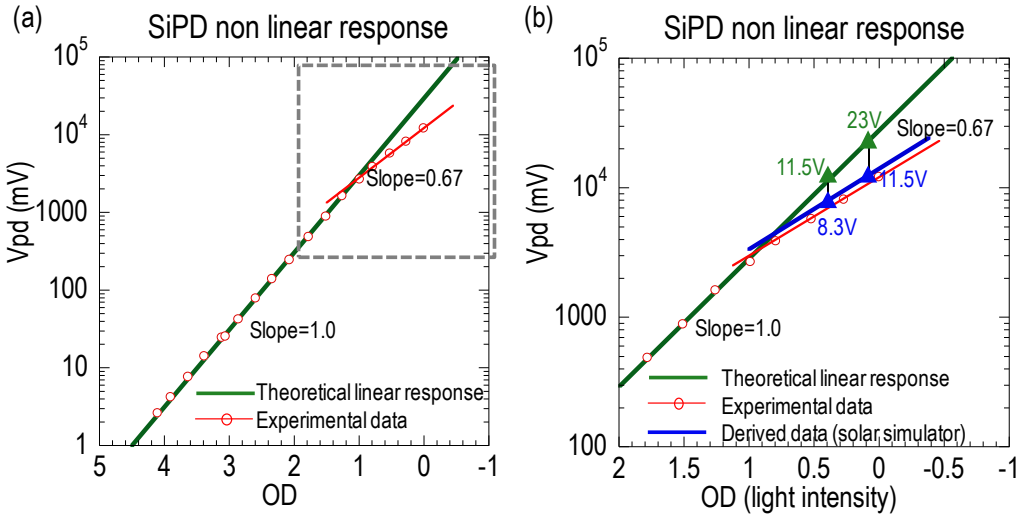

Figure 2.9 Non-linear response of SiPD under 514nm laser irradiation and solar simulator.

The experimental results clearly show that the SiPD response is linear up to V_{pd} =2V @10k gain, or 2V/10KΩ/ (0.229cm)^2 = 4mA/cm^2 photocurrent, or incident power of 20mW/cm^2 (*SR*(514nm) = 0.21A/W) on the SiPD, which is about 0.2 sun. Above this level, the photocurrent no longer scales linearly with the irradiance, but follow a power law:

Jph (V_{pd}) $\propto I^{0.67}$, possibly due to recombination. However, the response of SiPD to green laser or solar simulator is slightly different due to the wavelength dependent *SR*. It has been shown in the above calibration that when V_{pd} = 11.5V, the actual light intensity corresponds to V_{pd0}=23V if the SiPD response is linear. Assuming the power law at similarly high intensity for solar simulator is similar to the green laser, the power law curve has to be shifted up a little from the red line to the blue line, which presents the V_{pd} dependence on light intensity of the solar simulator. The V_{pd} can be read from the curve to be 8.3V when the V_{pd0} = 11.5V, corresponding to AM1.5 spectrum.

The accuracy of this procedure is not promising since the result is interpolated from experimental data points in log scale. Another possible error is that the solar simulator beam is not perfectly collimated, so the intensity is sensitive to spatial positioning of the device.

This issue has been solved after we got a calibrated Sol2A (Newport 94062a) solar simulator and a calibrated reference silicon cell. When the Sol2A simulator is tuned to one “sun” according to the calibrated silicon cell, the V_{pd} of the SiPD reads 8.7V, not far from derived value 8.3V (without mismatch factor correction, see next section).

2.7 Mismatch factor

As mentioned earlier, the standard reporting condition (SRC) contains three main specifications: device temperature during the measurement (25°C); the total incident irradiance (1000Wm^{-2}); and the spectral distribution (AM 1.5). However, one or more conditions such as the AM 1.5 spectral distribution are very difficult and expensive to achieve, which require outdoors measurements or a very well tuned solar simulator, so the actual measurement condition will be different and the translation of the results are necessary.[1,2] This section will discuss the translation, or the mismatch factor correction.

Firstly, the performance parameters (J_{sc}, V_{oc} and *FF*) of an organic solar cell are dependent on temperature; although the effect is not strong, neither has it received much attention yet. Since it is difficult to stick a thermal couple to the device in the vacuum chamber and measure the temperature of the active layer accurately, the standard practice is to minimize the device exposure time to the solar simulator so that the temperature of the device will not deviate much from room temperature.

Secondly, it is well known from the diode theory that the V_{oc} logarithmically depends on irradiance (V_{oc} = n kT/q ln(I_{sc} /I_0)), and it has been shown previously that the J_{sc} scales linearly at lower irradiance level but may scale sub-linearly at higher irradiance level depending on the characteristics of the solar cell. However, these corrections can be avoided by tuning the total irradiance of the solar simulator to exactly 1000Wm^{-2}, and the correction near one sun is easy to establish.

The main concern is to work out the translation of the device *PCE* from a solar simulator condition to AM1.5 standard condition. Assuming the V_{oc} and *FF* are not sensitive to the spectral mismatch factor (M) within a reasonable range (0.7<M<1.3), and the spectral

responsivity of the device under test (DUT) is the same at short circuit condition and maximum power condition, the *PCE* is proportional to J_{sc} and can be written as:

$$\mathrm{J_{AM1.5,DUT}} = \int_a^b \mathrm{I_{AM1.5}}(\lambda) \cdot SR_{\mathrm{DUT}}(\lambda) \cdot \mathrm{d}\,\lambda \ldots\ldots (1)$$

$$\mathrm{J_{sim,DUT}} = \int_a^b \mathrm{I_{sim}}(\lambda) \cdot SR_{\mathrm{DUT}}(\lambda) \cdot \mathrm{d}\,\lambda \ldots\ldots (2)$$

Where $\mathrm{J_{AM1.5,DUT}}$ and $\mathrm{J_{sim,DUT}}$ are the current outputs of DUT under standard AM1.5 spectrum and under solar simulator, respectively. $\mathrm{J_{AM1.5,DUT}}$ is to be determined and $\mathrm{J_{sim,DUT}}$ can be measured. $\mathrm{I_{AM1.5}}(\lambda)$ and $\mathrm{I_{sim}}(\lambda)$ are the irradiance of both spectrum, *a* and *b* the wavelength range of $SR_{\mathrm{DUT}}(\lambda)$, and $SR_{\mathrm{DUT}}(\lambda)$ the spectral responsivity of DUT, which might be dependent on irradiance level too.

The $\mathrm{I_{sim}}(\lambda)$ of the simulator needs to be calibrated by a calibrated reference cell.

$$\mathrm{J_{sim,RC}} = \int_c^d \mathrm{I_{sim}}(\lambda) \cdot SR_{\mathrm{RC}}(\lambda) \cdot \mathrm{d}\,\lambda \ldots\ldots (3)$$

$$\mathrm{J_{AM1.5,RC}} = \int_c^d \mathrm{I_{AM1.5}}(\lambda) \cdot SR_{\mathrm{RC}}(\lambda) \cdot \mathrm{d}\,\lambda \ldots\ldots (4)$$

Where $\mathrm{J_{AM1.5,RC}}$ and $\mathrm{J_{sim,RC}}$ are the currents of reference cell (RC) under standard AM1.5 spectrum and under solar simulator, respectively. $\mathrm{J_{sim,RC}}$ will be measured to determine the $\mathrm{I_{sim}}(\lambda)$, and $\mathrm{J_{AM1.5,RC}}$ is provided as the calibration data. $SR_{\mathrm{RC}}(\lambda)$ is the spectral responsivity of RC, *c* and *d* the wavelength range of $SR_{\mathrm{RC}}(\lambda)$. Ideally, the RC should be made of same materials and technology as the DUT, making the mismatch factor (M) close to unity. However, most organic solar cells cannot meet the most significant requirement: stability, so the commonly used reference cells are still silicon cells.

(2)/(1)*(4)/(3), we obtain:

$$\frac{\mathrm{J_{sim,DUT}}}{\mathrm{J_{AM1.5,DUT}}} \cdot \frac{\mathrm{J_{AM1.5,RC}}}{\mathrm{J_{sim,RC}}}$$

$$= \frac{\int_a^b \mathrm{I_{sim}}(\lambda) \cdot SR_{\mathrm{DUT}}(\lambda) \cdot \mathrm{d}\,\lambda}{\int_a^b \mathrm{I_{AM1.5}}(\lambda) \cdot SR_{\mathrm{DUT}}(\lambda) \cdot \mathrm{d}\,\lambda} \cdot \frac{\int_c^d \mathrm{I_{AM1.5}}(\lambda) \cdot SR_{\mathrm{RC}}(\lambda) \cdot \mathrm{d}\,\lambda}{\int_c^d \mathrm{I_{sim}}(\lambda) \cdot SR_{\mathrm{RC}}(\lambda) \cdot \mathrm{d}\,\lambda} \ldots\ldots (5)$$

The symmetrical form of equation (5) has some interesting properties: on the left hand side, the device areas for both DUT and RC are cancelled. On the right hand side, only the spectral shape but not the absolute value of $\mathrm{I_{sim}}(\lambda)$ is important, and the possible nonlinear dependence of $SR_{\mathrm{DUT}}(\lambda)$ and $SR_{\mathrm{RC}}(\lambda)$ on irradiance level is also cancelled. Take note that "*a*=*c* and *b*=*d*" is required to completely cancel the above effect, while the reference silicon cell organic solar cells could have very different *SR* and other characteristics. For example, the response wavelength range of unfiltered silicon cell is 350-1100nm, quite different from that of P3HT: PCBM cells 350-700nm. This indicates an undesirable situation: If the light intensity in range 700-1100nm of the solar simulator is very different from AM1.5, there is no effect on $\mathrm{J_{sim,DUT}}$ while $\mathrm{J_{sim,RC}}$ may change a lot, which causes a larger error. However, this can be improved by putting a KG5 filter in front of the silicon reference cell to modify its *SR* range to 350-700nm.

Let

$$\mathrm{M} = \frac{\int_a^b \mathrm{I_{sim}}(\lambda) \cdot SR_{\mathrm{DUT}}(\lambda) \cdot \mathrm{d}\,\lambda}{\int_a^b \mathrm{I_{AM1.5}}(\lambda) \cdot SR_{\mathrm{DUT}}(\lambda) \cdot \mathrm{d}\,\lambda} \cdot \frac{\int_c^d \mathrm{I_{AM1.5}}(\lambda) \cdot SR_{\mathrm{RC}}(\lambda) \cdot \mathrm{d}\,\lambda}{\int_c^d \mathrm{I_{sim}}(\lambda) \cdot SR_{\mathrm{RC}}(\lambda) \cdot \mathrm{d}\,\lambda} \ldots\ldots (6)$$

Where M is the spectral mismatch factor,[2] and M is dependent only on spectral shape of $\mathrm{I_{sim}}(\lambda)$,$\mathrm{I_{AM1.5}}(\lambda)$, $SR_{\mathrm{DUT}}(\lambda)$ and $SR_{\mathrm{RC}}(\lambda)$, which are calibration data or can be easily measured experimentally.

Usually the total irradiance of solar simulator is calibrated by tuning it until $J_{sim,RC} = J_{Am1.5,RC}$, the latter is calibration data, provided by the manufacturer of the calibrated cell. Then (5) becomes:

$$\frac{J_{sim,DUT}}{J_{AM1.5,DUT}} = M, \text{or}$$

$$J_{AM1.5,DUT} = {J_{sim,DUT}}/{M} \quad \text{or}$$

$$PCE_{AM1.5,DUT} = {PCE_{sim,DUT}}/{M}$$

thus the accurate translation of the solar cell performance to the AM1.5 standard conditions is done.

2.8 References

1 Emery, K. & Osterwald, C. Solar cell efficiency measurements. *Solar cells* **17**, 253-274 (1986).

2 Osterwald, C. Translation of device performance measurements to reference conditions. *Solar cells* **18**, 269-279 (1986).

3 ASTM Standard G173, Standard Tables for Reference Solar Spectral Irradiances: Direct Normal and Hemispherical on 37° Tilted Surface,
American Society for Testing and Materials, West Conshocken, PA, USA.

4 van Duren, J. K. J. *et al.* Relating the Morphology of Poly (p ‐ phenylene vinylene)/Methanofullerene Blends to Solar ‐ Cell Performance. *Adv. Funct. Mater.* **14**, 425-434 (2004).

5 van Bavel, S. S., Bärenklau, M., de With, G., Hoppe, H. & Loos, J. P3HT/PCBM bulk heterojunction solar cells: impact of blend composition and 3D morphology on device performance. *Adv. Funct. Mater.* **20**, 1458-1463 (2010).

6 Brabec, C. J., Shaheen, S. E., Winder, C., Sariciftci, N. S. & Denk, P. Effect of LiF/metal electrodes on the performance of plastic solar cells. *Appl. Phys. Lett.* **80**, 1288 (2002).

7 Mihailetchi, V., Blom, P., Hummelen, J. & Rispens, M. Cathode dependence of the open-circuit voltage of polymer: fullerene bulk heterojunction solar cells. *J. Appl. Phys.* **94**, 6849 (2003).

8 Koster, L., Mihailetchi, V., Xie, H. & Blom, P. Origin of the light intensity dependence of the short-circuit current of polymer/fullerene solar cells. *Appl. Phys. Lett.* **87**, 203502 (2005).

9 Schilinsky, P., Waldauf, C. & Brabec, C. J. Recombination and loss analysis in polythiophene based bulk heterojunction photodetectors. *Appl. Phys. Lett.* **81**, 3885 (2002).

10 Riedel, I. *et al.* Effect of Temperature and Illumination on the Electrical Characteristics of Polymer – Fullerene Bulk – Heterojunction Solar Cells. *Adv. Funct. Mater.* **14**, 38-44 (2004).

Chapter 3. Crosslinked donor network solar cells

In this chapter, we introduce a novel molecular infiltration method to fabricate polymer-based solar cells based on sterically hindered bis(fluorophenyl azide)s (s-FPAs or crosslinker). The donor polymer film is first deposited and photocrosslinked with versatile high-efficiency nitrene chemistry, then the molecular acceptor is "doped" into this film by contact with its solution under precise control. The morphologies of both normal blend and crosslinked devices have been characterized by AFM and TEM, showing that the donor-acceptor phase separation is finer in crosslinked devices. The 2D *PCE* map of regioregular poly(3-hexylthiophene) (rrP3HT):phenyl-C61-butyrate methyl ester (PCBM) solar cells as a function of the effective amount of rrP3HT and PCBM in the film has been established for the first time. The results reveal a "ridge of high efficiency" that coincides with the 1:1 P3HT: PCBM weight ratio line comprising islands of particularly high efficiencies at both low and high film thicknesses (maximum *PCE*, 4.2%). The *PCE* are generally 20-30% higher than blend films of the same composition made by conventional spin-casting. Further analysis shows that the internal quantum efficiency (*IQE*) of the crosslinked devices are near to unity across a wide thickness and composition range, which is a special advantage of the crosslinking method.

The efficient operation of donor–acceptor photovoltaic (PV) cells depends on having a suitable bulk heterostructure that can fully dissociate the photogenerated excitons into charge carrier pairs and transport them away without recombination to be collected at the electrodes.[1,2] In order to achieve this, the bulk heterojunction needs an appropriate electronic structure that gives efficient exciton dissociation and suppressed electron–hole recombination, and an appropriate morphology that gives a high heterojunction area and efficient charge carrier transport to the collection electrodes. The ideal morphology is an ultrafine intimate mixture of donor and acceptor nanophases at the exciton diffusion length scale (of the order of 10 nm) which has path continuity with high carrier mobilities across the much larger thickness of the photoactive layer (100–200 nm). To be technologically useful, this morphology further needs to be reliably manufacturable over large areas. So far there is no fabrication method that can meet all these requirements in a general way. The standard approach depends on spontaneous demixing of a donor–acceptor mixture film[3] under thermal[4] or solvent vapor[5] anneal, or in the presence of solvent additives.[6] While this is capable of generating an ultrafine morphology for some donor–acceptor systems, such as P3HT: PCBM to give high internal quantum efficiencies,[2,7] the processing window is rather narrow and variable,[4,5,8-11] and the final morphology is itself metastable and vulnerable to further phase coarsening.[10-14] Therefore the morphology aspect of present generations of donor–acceptor solar cells tends to be sub-optimal and suffers from issues including marked sensitivity to film composition, thickness and processing conditions.

3.1 General crosslinking methodology for semiconducting polymers

Heterostructures are central to efficiently manipulating charge carriers and excitons for high-performance semiconductor devices. Although these can be achieved by stepwise evaporation of molecular semiconductors, they are a considerable challenge for solution processed polymer organic semiconductors (OSCs) owing to re-dissolution of the underlying layers. Various methods have been employed to avoid this, including orthogonal solubility,[15] precursor polymers,[16] de-mixing of polymer mixtures,[17] or layer-by-layer polyelectrolyte assembly,[18] but these limit the useable materials set. There has recently been an intensive effort to develop polymer OSCs with thermal-or photo-crosslinkable side chains[19-21] or end-groups,[22,23] However this requires intensive synthesis and so is not amenable to rapid prototyping. Furthermore, the required high concentration[19] of the crosslinker seems to disrupt the interchain pi-stacking and degrade the semiconductor performance.

To overcome this, a simple and versatile photo-crosslinking methodology based on sterically hindered bis(fluorophenyl azide)s has been developed, an example of which is ethylene bis(4-azido-2,3,5-trifluoro-6-isopropylbenzoate) (chemical structure in inset of **Figure 3.1**). The FPA family in general has a number of desirable attributes (e.g. deep ultraviolet activation and non-specific insertion), and FPA prototypes[24,25] have been successfully used as photo-resists, and photo-affinity labels[26-28] and in doped conducting polymers.[27,29,30] They were found unsuitable for use in polymer OSCs because of exciton quenching and charge-carrier trapping. By suitably derivatising the FPA core with a steric substituent, the arene-perfluoroarene-interaction[31] is successfully suppressed to produce sterically-hindered FPA derivatives that are found suitable to produce quality polymer OSC heterostructures (**Figure 3.1**).

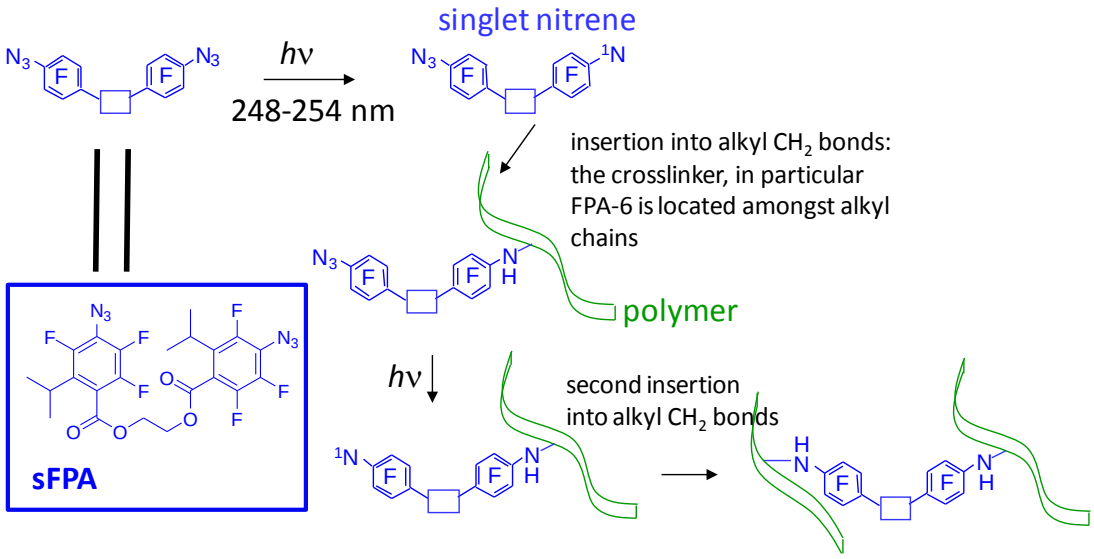

Figure 3.1 Schematic of the desired FPA photocrosslinking process. Inset: Chemical structure of sFPA

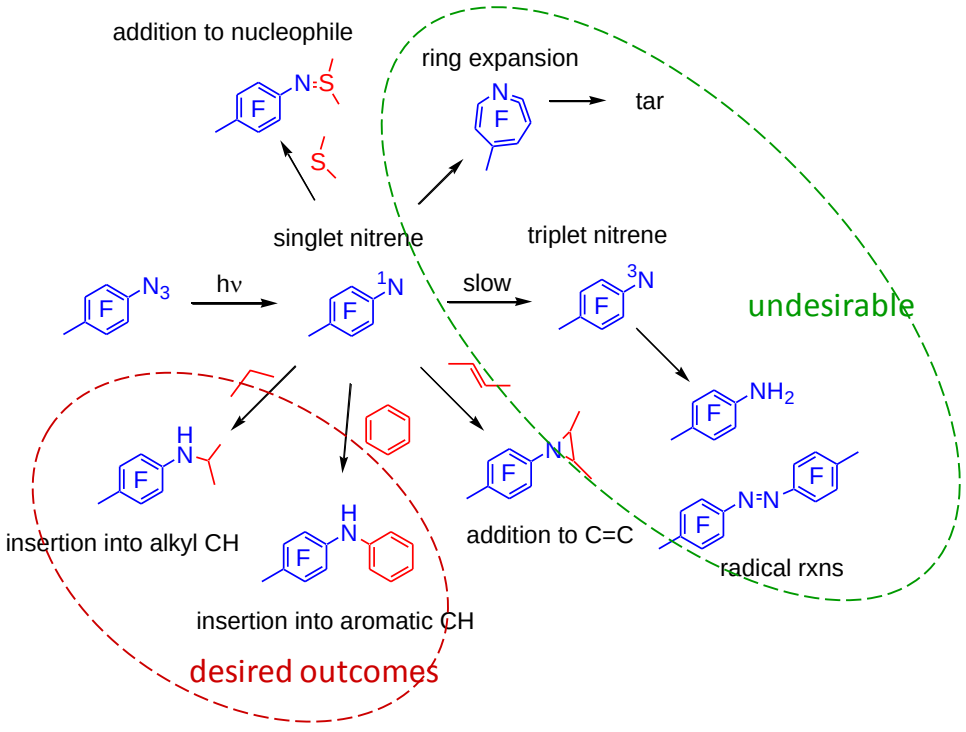

Figure 3.2 Overview of possible reactions of photogenerated singlet nitrenes in polymer OSCs

Furthermore, because the crosslinking mechanism is nonspecific (that is, does not require two specific chemical groups to bond together, **Figure 3.2**), extremely high photocrosslinking efficiency can be achieved at very low concentrations. In the ideal situation, one crosslinker per polymer chain is the minimum requirement (every polymer chain is linked to two other chains), which is below 1mol% of crosslinkers, for high-molecular-mass polymers. This is far lower than the 20mol% often needed in specific crosslinking schemes, such as epoxy-ring opening.

The methodology is simple: The polymer OSC is mixed with the sFPA in solution and spin-cast or inkjet-printed to give films that are then crosslinked by deep-ultraviolet (DUV) exposure in nitrogen. The absorption band of the sFPA turns out to be well matched with available DUV sources (e.g. low-pressure Hg lamps and excimer lasers) and to the transmission windows of polymer OSCs, as illustrated in **Figure 3.3** by several poly(p-phenylenevinylene)s, poly(fluorene) copolymers and poly(thiophene). This allows deep photo-exposures into thick films (up to 300 nm thick) with low photo-oxidation risks, which makes possible multilayer fabrication by sequentially depositing and photocrosslinking the layers. The photocrosslinked films remain remarkably fluorescent at several mol% concentration in high-MW polymers, indicating that the amount of exciton traps is well below the quenching threshold.[32]

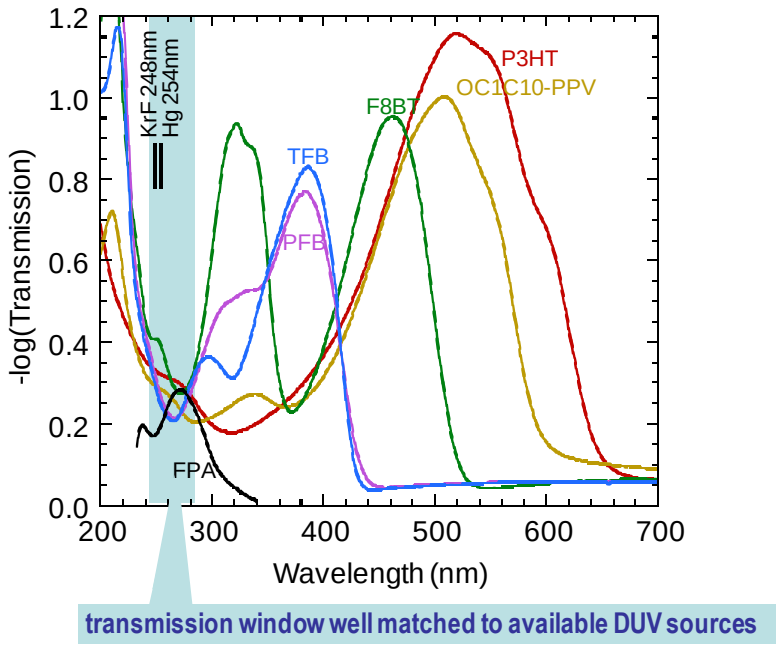

Figure 3.3 Absorption spectra of the sFPA and selected polymer OSCs. Polymer film thickness is about 100 nm.

3.2 Experimental methods

Materials: P3HT (Sigma Aldrich, >98% head-to-tail regioregularity, molecular weight 30-60K) and PCBM (Nano-C) were used as received. Crosslinkers were synthesized in house. Photocrosslinking was typically performed in a glove box (pO2; $p$$H_2O$< 1 ppm) at 254-nm deep-ultraviolet exposure with a dose of *ca*. 300 mJ cm^{-2} from an 8-W low-pressure Hg lamp.

Ultraviolet – visible Spectroscopy (UV-vis): UV-Vis absorption spectra were collected using a diode-array UV-Vis spectrograph (DW 1024, Ocean Optics) in the glovebox. The P3HT: PCBM films were spin cast on O2 plasma cleaned glass substrates.

Atomic Force Microscopy (AFM): Atomic force microscopy was performed in air with a Dimension 3000 Nanoscope operating on a tapping mode. Silicon cantilevers are used and 1 x 1 μm areas are scanned using 256 lines at 1 Hz scan speed.

Transmission Electron Microscopy (TEM): The pristine P3HT and crosslinked P3HT (after infiltration and removal of PCBM) TEM samples were prepared on PET flexible substrates. 150nm Al, 50nm PEDT: PSSH and ~100nm P3HT layer were sequentially deposited on PET substrates, and capped with 150nm Al. The Al layer helps to locate the sample and protect P3HT from electron radiation damage. Then the ~100nm thick cross-section of the sample was microtomed then floated from the water soluble PEDT: PSSH layer onto the surface of DI water and picked up with 200-mesh copper TEM grids without supporting film. Bright field TEM morphology observation was performed on a JEOL 2010 at 200KeV and weak focus condition.

Device fabrication and characterization: Solar cell devices were fabricated on ITO-coated glass substrates. The substrates were cleaned with an SC1-recipe. 50-nm-thick PEDT: PSSH (1:16 w/w; reformulated Baytron P, Leverkusen) films were then spin-cast, and annealed at 120ºC in the glovebox to remove absorbed moisture. The P3HT: PCBM films were then formed in the glovebox, either by conventional spin-casting of biblend mixtures (typically 1:1 by weight) or by back-infiltration of crosslinked P3HT films as described below and in the next section. The biblend film thicknesses were controlled through the solution concentration (18–24 mg mL^{-1}) and spin speed. All materials were processed from chlorobenzene.

To fabricate the infiltrated devices, P3HT solutions in chlorobenzene (10–20 mg mL^{-1}) with 3 weight percent of ethylene bis(4-azido-2,3,5-trifluoro-6-isopropylbenzoate (P3HT = 100%) as the crosslinker additive were spincast on ITO/ PEDT substrates. The films were crosslinked by

deep-ultraviolet exposure and washed with chlorobenzene twice on the spinner. PCBM was dissolved into chlorobenzene (8–30 mg mL^{-1}) and spun at different speeds onto the P3HT films. The thicknesses of the photoactive layers lie between 80 and 220 nm for both biblend and infiltrated network methods. All devices were then annealed in glove box at 140ºC for 10 min (hotplate temperature) before a 30-nm-thick Ca (capped with 120-nm-thick Al) layer was evaporated as cathode at 1 x 10^{-6} Torr. Eight devices (4.3 mm^2 each) were prepared and measured on each substrate.

The density of the P3HT nanophase in the photoactive layer was assumed to be 1.1 g cm^{-3}, based on its known crystalline density (1.16 g cm^{-3}).[33] The density of the PCBM nanophase was assumed to be 1.7 g cm^{-3}, based on the known crystalline densities of the 1 : 0.5 adduct of the PCBM : chlorobenzene complex (1.65 g cm^{-3}) and the 1 : 1 adduct of the PCBM : 1,2-dichlorochlorobenzene complex (1.67 g cm^{-3}),[34] which set the lower bound due to the incorporation of solvent molecules. The ratio of these densities is consistent with our measurements of (d_{P3HT}, d_{PCBM}) as described in the text.

Current–voltage characteristics were measured on a Keithley 4200 semiconductor characterization system, illuminated with the simulated AM1.5 spectral output (at 1.2 sun, due to the spectral mismatch) of a home-built solar simulator with Xe arc lamp corrected with an AM1.5G filter. This simulator was cross-calibrated with a commercial class ABA solar simulator (Oriel Sol2A) that was calibrated by the manufacturer and checked at Solar Energy Research Institute of Singapore (SERIS). Spectral mismatch correction was applied to the reported results.

Optical modeling: The standard optical transfer matrix method was used to model the photonic properties of the solar cells. The complex dielectric functions of all the layers were either known or measured in this work over the 400–650-nm wavelength range. The dielectric functions of P3HT: PCBM layer were measured by variable-angle spectroscopic ellipsometry on annealed biblend films with weight ratios 1:2, 1:1 and 2:1, and then interpolated by Bruggeman effective medium approximation to obtain the dependence on film composition. Computations were performed at wavelength steps of 5 nm, and (d_{P3HT}, d_{PCBM}) steps of 10 nm. The fractional absorption of the photoactive layer was computed from the difference in Poynting vectors. The integrated absorbed power and photon flux for the experimental solar simulator were then computed at 2-nm steps using the measured incident spectral irradiance taking care of reflection at the glass substrate. More details are described in chapter 5.

3.3 Absorption spectrum of P3HT: PCBM crosslinked network solar cells

We employed photocrosslinking based on the sterically-substituted bis(fluorinated phenyl azide) (*s*-FPA) platform that is effective at extremely low concentrations and does not damage the essential properties of polymer semiconductors.[29,32] Previously contiguous polymer–polymer donor–acceptor heterostructures have been demonstrated using this platform together with a sacrificial phase-directing method to give separate control of lateral and vertical length scales.[32] Here we combined the use of the crosslinking with infiltration of molecular acceptors to generate surprisingly efficient network morphology. These network-P3HT: PCBM films were made by spin-casting P3HT films with 3–5 weight-to-weight (w/w) % of the *s*-FPA photocrosslinker ethylene bis(4-azido-2,3,5-trifluoro-6-isopropylbenzoate (for chemical

structures, see inset of **Figure 3.1**) onto the desired substrates. The films were then exposed with 254-nm deep ultraviolet (DUV) in the transparency window of P3HT in a N_2 glovebox to activate primarily alkyl side-chain crosslinking through a nitrene-mediated mechanism.[32]

3.3.1 Fabrication process of crosslinked network solar cells

Figure 3.4 shows the film retention characteristics of P3HT as a function of the *s*-FPA concentration. These characteristics were measured after development with chlorobenzene (CB) to remove the uncrosslinked and low molecular-weight (MW) fractions. Since *s*-FPA exhibits near unity crosslinking efficiency,[32] the crosslink density ρ in the film is also given by the crosslinker concentration. The plot shows the film retention rises above zero at the gel point ($\rho \approx 2 \times 10^{19}$ cm^{-3}, or 1.6 w/w%) where an infinite polymer network first emerges, and increases towards unity with increasing ρ. Thus the network stiffness and porosity is tuneable through ρ. We typically set $\rho \approx 4–6 \times 10^{19}$ cm^{-3} (3-5 w/w%) to reach the lightly-crosslinked regime where there is one crosslink per 100–70 polymer repeat units.

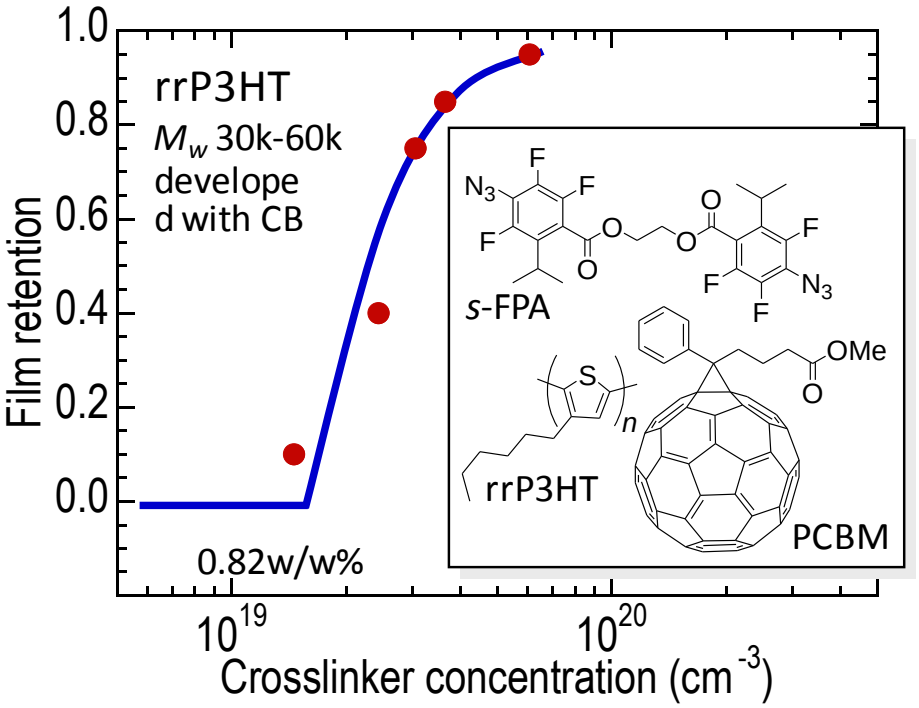

Figure 3.4 Film retention characteristics of P3HT using *s*-FPA as photocrosslinker. Inset gives the chemical structures.

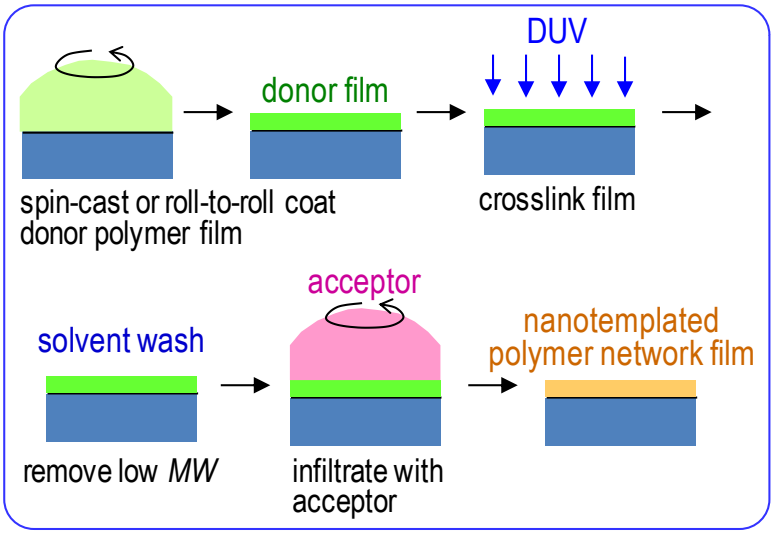

Figure 3.5 Processing schematic for nanotemplated polymer network films.

Figure 3.5 shows a schematic of the film processing. After the donor polymer film is crosslinked, the low MW fraction is removed by a solvent wash, and the molecular acceptor is then infiltrated into the network by spinning from solution.

Figure 3.6 shows the electronic spectra that reveal the evolution of P3HT polymer order with network formation. The crosslinked P3HT film (ρ = 3.7 x 10^{19} cm^{-3}; red spectrum) loses 20% of its absorption intensity after solvent wash (orange spectrum), due to removal of the low MW fraction. However the absorption features at 517, 560 and 610 nm (which correspond to 0→2, 0→1 and 0→0 vibronic bands)[35] persist, and the lowest-lying transitions are in fact slightly enhanced. This is characteristic of improved local polymer order characterized by planarized chain segments. When a PCBM solution (8 mg mL^{-1} in CB) is spin-cast over this film, the polymer band further diminishes and its spectral weight shifts towards shorter wavelengths, while the PCBM absorption tail[4] emerges below 450 nm (green). The blue shift arises because of disordering of the polymer chain conformation, which demonstrates that the PCBM molecules are incorporated into the film matrix. No surface PCBM crystals were found by optical microscopy. The infiltration is fully reversible, as contact with the pure solvent removes PCBM and restores the starting polymer spectrum (orange).

The incorporated amount of PCBM can be varied through its solution concentration and spin speed which together control the amount of PCBM deposited (light- and dark-blue spectra). The film composition was established for each film from the calibrated absorptivities and the measured initial and final film thicknesses, and presented as (d_{P3HT}, d_{PCBM}) coordinates. These give the effective P3HT and PCBM thicknesses which correspond to the distributed volume per unit area of the films, where the total film thickness $d = d_{P3HT} + d_{PCBM}$, by volume conservation.

They have been independently confirmed by X-ray photoelectron spectroscopy. For the set of spectra in **Figure 3.6**, d_{P3HT} is 65 nm, while d_{PCBM} is varied between 30 to 70 nm. Thus PCBM can be "dosed" at will into the film.

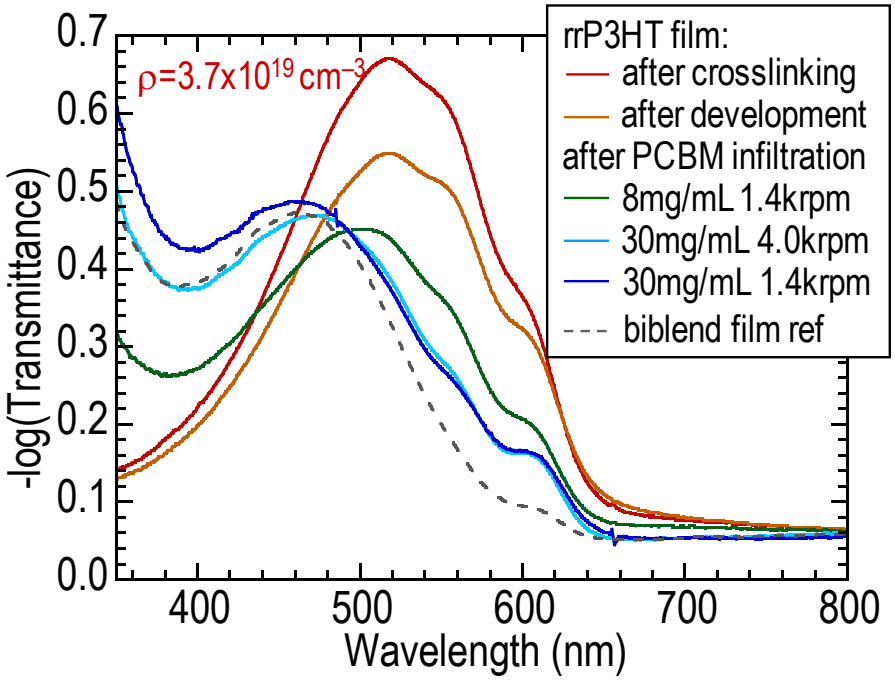

Figure 3.6 Electronic spectra of key stages: after crosslinking P3HT (d_{P3HT} = 77 nm; red), after chlorobenzene development (65 nm; orange), after PCBM infiltration at 8 mg mL^{-1} by spin-casting at 1,400 rpm (d_{PCBM} = 30 nm; green), or 30 mg mL^{-1} at 4.0 krpm (50 nm; light-blue), or 30 mg mL^{-1} at 1.4 krpm (70 nm; dark-blue); biblend film with (d_{P3HT}, d_{PCBM}) = (55 nm, 45 nm) as reference. Density of P3HT, 1.1 g cm^{-3}; PCBM, 1.7 g cm^{-3}.

The crosslinked P3HT host also shows a beneficial resilience to disordering by the PCBM phase. This is evidenced by the stronger 0⟶0 transition, which derives intensity from the ordered polymer segments, in the network films than in the demixed biblend film (grey dashed). The biblend film shows less order at low PCBM concentrations as spin-cast,[4,36] and even after thermal annealing to 140ºC, above the ordering transition at ≈ 110ºC where the biblend film

demixes to produce ordered P3HT domains.[4] The better order obtained in the P3HT network is beneficial to hole mobility which is an important determinant of solar cell performance[10,37] (the mobilities of both electrons and holes need to be larger than 10^{-3} cm^2 V^{-1} s^{-1} to minimize the space-charge voltage penalty).[38] This is assisted to some extent here by the more isotropic polymer orientation distribution that is expected to occur when P3HT orders about the PCBM nanophase which becomes conducive to hole transport in the film thickness direction.[39] In addition the crosslinked network suppresses the undesirable surface enrichment of P3HT, as evidenced by ion-sputter depth-profiling X-ray photoelectron spectroscopy,[40] which causes an unfavourable compositional layering during annealing of the biblend film.[36,41] Thus it becomes possible to achieve high *PCE* for the crosslinked network films without annealing after the cathode deposition.[4,36]

Absorption normalized spectrum of more blend and crosslinked P3HT: PCBM composites with different composition and thickness are shown in **Figure 3.7**. The typical range of the absorption spectra of spincast blend films are shaded blue, while those of crosslinked films are shaded red. There are 5 spectra for blend films and 8 for crosslinked network films. Their overlapping region is shaded in purple. It can be seen clearly that the crosslinked network films generally have a larger population of the highly-ordered P3HT segments than blend films.

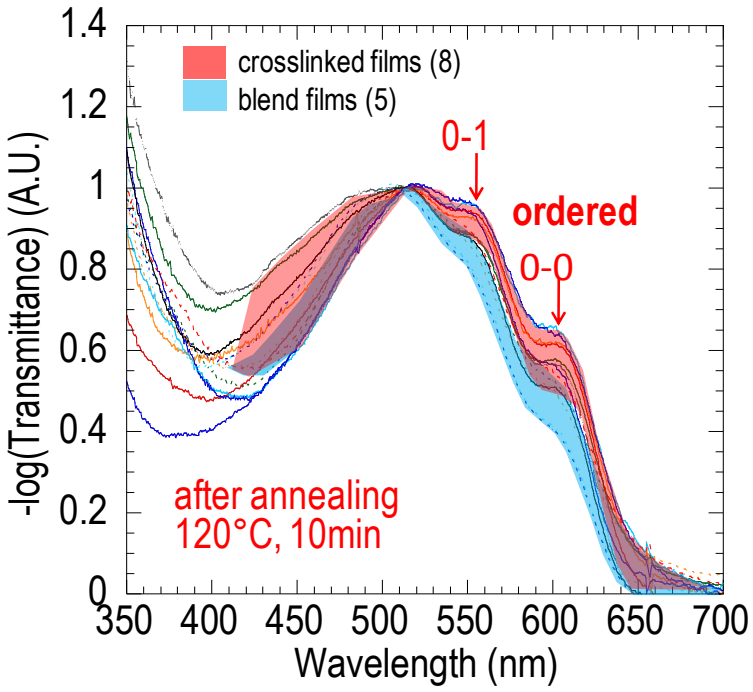

Figure 3.7 Absorption spectrum of blend and crosslinked P3HT: PCBM films.

3.3.2 Effect of crosslinker concentration

The solar cell device performance is very sensitive to the fabrication conditions, especially the state of P3HT such as morphology (crystallinity), regioregularity, and molecular weight.[10] In this section, the effect of crosslinker concentration on the absorption spectrum is discussed, which may have some indications on the morphology.

In **Figure 3.8**, the absorption spectrum of normal blend BHJ (0 w% of sFPA) and crosslinked (3 or 5 w% of FPA6) films with similar composition (donor acceptor ratio and film thickness) are compare for both before and after annealing. Before annealing, the blend film and crosslinked films containing 3 w% sFPA are obviously less crystalline than the crosslinked films containing 5 w% sFPA (dotted line in **Figure 3.8**). This is because the P3HT chains are free to move in

the blend film during the demixing process with PCBM, while in the 3 w% crosslinked film, the molar ratio of sFPA to P3HT chain is calculated to be mP3HT/MP3HT : m_{sFPA}/M_{sFPA} = 1/30,000: 0.03/544.4 = 1.65:1. Considering that each sFPA has two crosslinks, which means one P3HT chain is connected to 3.3 other chains on average (minimum requirement for crosslinking is 2). The P3HT chains form a loose net and they are still free to move. However, in the 5 w% crosslinked films, one P3HT chain is connected to 5.5 other chains on average. Thus the chance of two polymer chains binding by no less than 2 crosslinks is high, which makes them not free to move any more. These chains are bounded and they are somewhat resistive to the infiltration of PCBM, as reflected in the more obvious 0-0 and 0-1 peaks. In addition, the highest absorption peak shows less blue-shift and absorption drop than the other two. After annealing, the absorption of three films rise to the same position, due to the re-organization of the P3HT chains when heated above glass transition temperature. Interestingly, the 3 w% crosslinked film shows highest degree of P3HT crystallinity, followed by 5 w% crosslinked film and blend film after annealing. This effect will be discussed again in the next section, in regard of the morphology of the heterostructure.

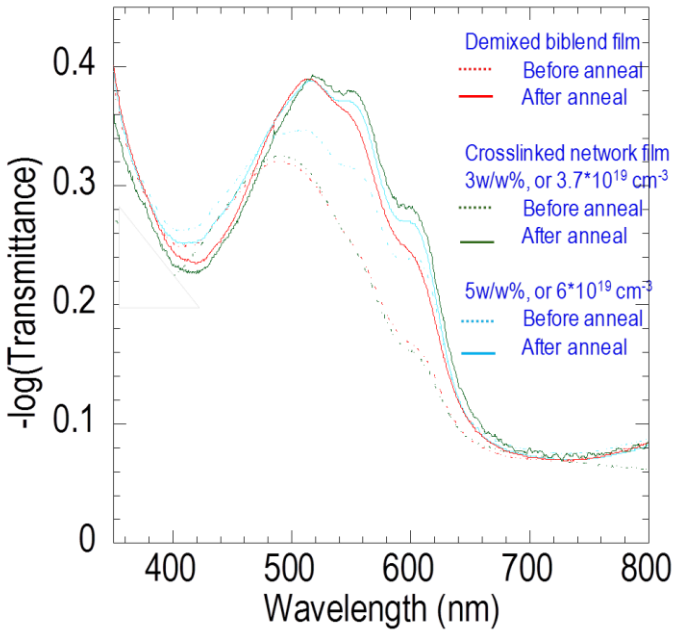

Figure 3.8 Effect of crosslinker concentration on the P3HT chain arrangement. Higher concentration of crosslinker makes the P3HT crosslinked network stiffer.

3.4 Morphology of the crosslinked network solar cells

The study on UV-vis absorption of the photoactive layer in last section has shown that the nanomorphology of the crosslinked heterostructure is different from that of the demixed bulk heterojunction. The model system of P3HT: PCBM has been extensively studied on morphology controlling. Methods such as thermal annealing,[42,43] solvent annealing,[5] solution pre-aging[44] and processing with solvent additives[45] have been shown to increase the P3HT crystallinity and donor and acceptor domain sizes and enhance the device performance. Among the above methods, thermal annealing, solvent annealing and solution pre-aging rely on the self-organization properties of P3HT, while the solvent additives method relies on the difference in donor and acceptor solubility and in the solvent drying rate. None of them are

methods with direct control. The crosslinking method employed in this study provides a possible route to directly control the structure of the polymer matrix, whose properties can be tuned by the amount of crosslinker used.

3.4.1 Surface morphology of the crosslinked P3HT: PCBM heterostructure

Atomic Force Microscopy (AFM) is one of the most common techniques to characterize the surface topography of a sample. Tapping mode has several key advantages compared with contact mode and non-contact mode, such as much lower chance to stick to or damage the sample, less stringent requirements for both the sample condition and the operating skills, and also providing some information on sample components. The additional information is obtained from phase imaging, which records the phase shift of the oscillation of the tip on the sample referred to free oscillations. The diagram is shown in **Figure 3.9.**

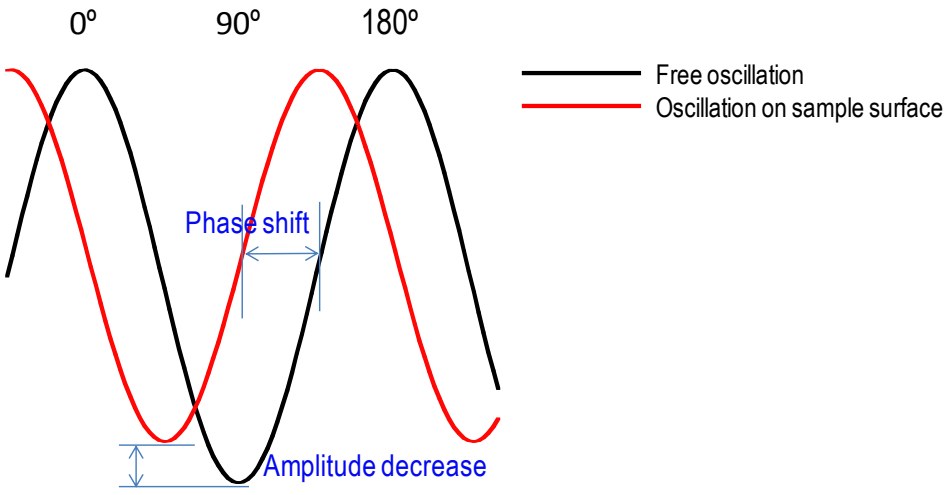

Figure 3.9 The origin of phase and amplitude images in AFM.

In fact, the phase contrast due to different material properties is widely seen in various samples, but phase image also contains topometric differences of the sample.

In this section, surface morphology of the P3HT polymer network with different concentrations of crosslinker will be discussed, as well as after PCBM infiltration and annealing.

Figure 3.10(a) presents the AFM height image of a typical P3HT: PCBM blend film after annealing, and **(b)** and **(c)** are the height and phase image of remaining P3HT network after washing the blend film with cyclopentanon to remove PCBM, respectively. The 50-nm-long, oval shape, black color holes in **(b)** and **(c)** were occupied by the PCBM rich phase before solvent wash, and this bad solvent washing process helps P3HT to form more ordered states, as shown in the phase image in **(c)**.

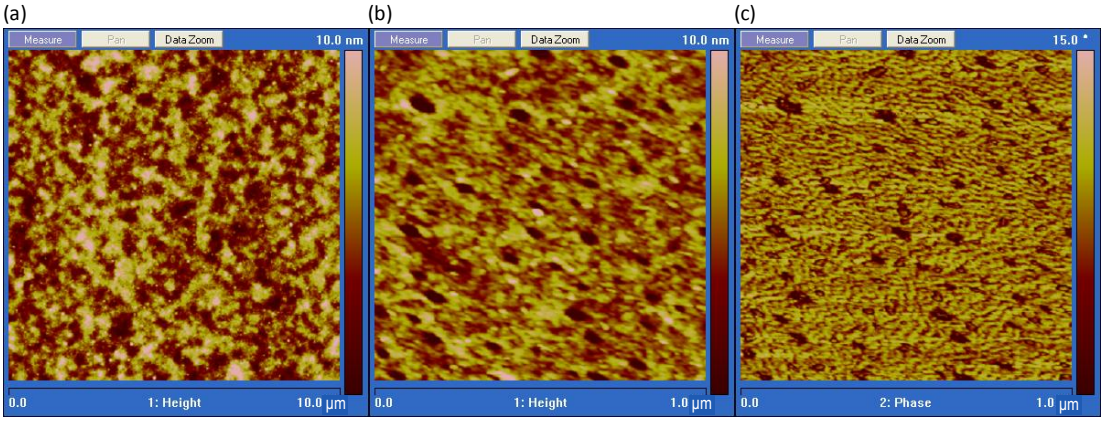

Figure 3.10 AFM images of conventional blend P3HT: PCBM. **(a).** Height image of conventional blend P3HT: PCBM, image size 10µm. **(b)** and **(c)**. Height and phase image of P3HT ordered states, obtained from P3HT: PCBM blend by cyclopentanon wash, image size 1µm.

To study the evolution of P3HT network formation, three samples are prepared with different amount of crosslinker. Sample A1 with 1 w/w%, or ρ = 1.2 x 10^{19} cm^{-3}, sample A2 with 3 w/w%,

or ρ = 3.7 x 10^{19} cm^{-3} and sample A3 with 5 w/w%, or ρ = 6.0 x 10^{19} cm^{-3}. They are all processed from chlorobenzene (CB). After crosslinking and thermal annealing at 130ºC for 10 minutes, they all show ordered states (**Figure 3.11**) in the phase image, as reported before.[46,47] The width of the fibrils was estimated to be around 10nm, indicating the upper limit of nano-crystalline region size in P3HT: PCBM system. To resolve the phase separation features of P3HT: PCBM composites, Transmission Electron Microscopy (TEM) has to be employed, as will be shown in section **3.4.2**.

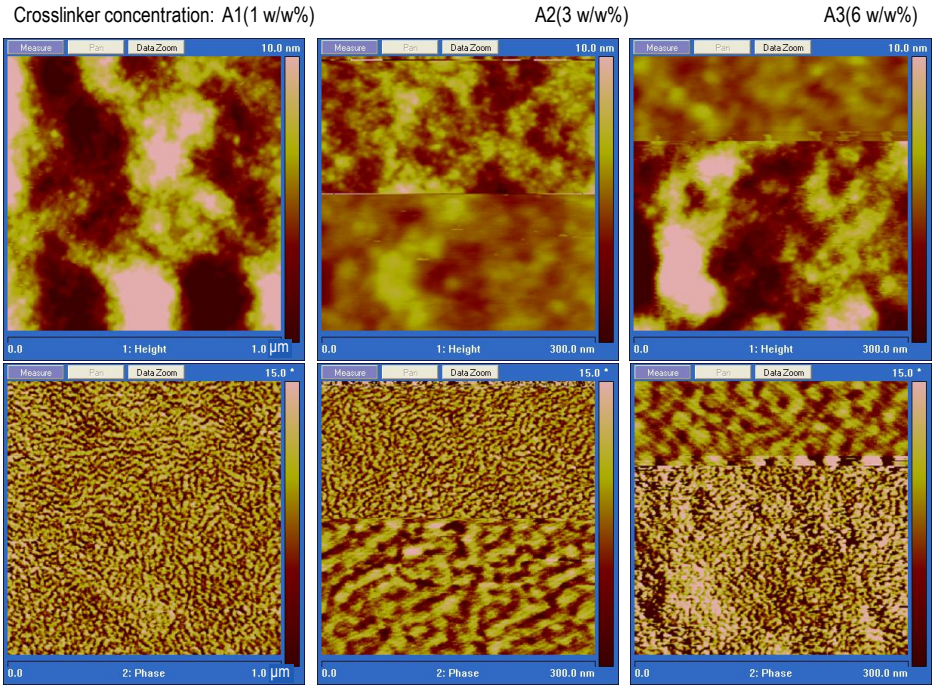

Figure 3.11 Height and phase images of P3HT films with different concentration of crosslinker. Left panel, 1 w/w%, image size 1µm; middle panel, 3 w/w%, image size upper half 1µm, lower half 0.3µm; right panel, 5 w/w%, image size upper half 0.3µm, lower half 1µm.

After CB wash and PCBM infiltration, the surfaces of infiltrated P3HT PCBM films show different characteristics in **Figure 3.12**: A1(1 w/w%) displays a rough surface, possibly related

to its thinner film thickness, while the surface morphology of A2(3 w/w%) is very similar to the conventional P3HT: PCBM blend surface. The surface of A3 (6 w/w%) shows some strange features, suggesting poor intermixing of both components due to the stiffness of highly crosslinked P3HT matrix. The phase images don't provide more information than height images.

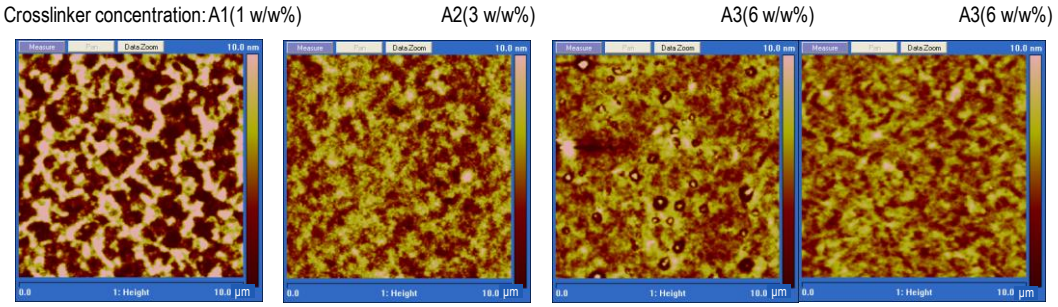

Figure 3.12 Height images of infiltrated P3HT: PCBM films with different concentration of crosslinker. Two positions of A3 film. image size 10µm.

After 130 ºC anneal for 10 minutes, the P3HT and PCBM nano-crystals re-organize, and the surface morphology of A1, A2 and A3 become similar, except that the feature size of A1 is finer (**Figure 3.13**).

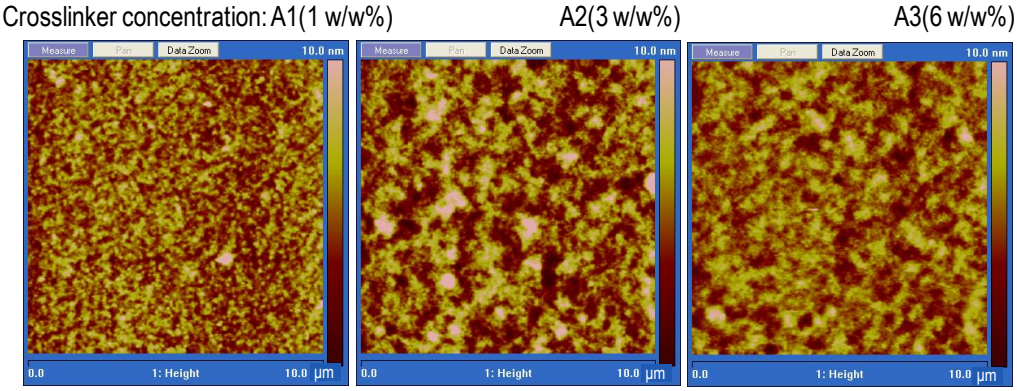

Figure 3.13 Height images of annealed infiltrated P3HT: PCBM films with different concentration of crosslinker. Image size 10µm.

3.4.2 Ultrafine morphology of the crosslinked P3HT: PCBM heterostructure

To obtain an indication of the length scale of order in P3HT segments, high-resolution transmission electron microscopy (HRTEM) was performed on ultrathin sections of the film before and after PCBM incorporation. For the latter, we removed the PCBM with hexane *in-situ* on the TEM grid (as confirmed by loss of the PCBM absorption band). Hexane is a non-solvent for P3HT and so does not disrupt the morphology of its network. No sample staining or supporting film was used to avoid structural artifacts. **Figure 3.14** shows the phase-contrast images collected in the weak defocus regime to additionally avoid phase artifacts. Under these conditions, the phase contrast transfer function (CTF) is well-behaved for spatial wavelengths down to *ca*. 0.5 nm. The cross section of the pristine P3HT film (**Figure 3.14(a)**) reveals a coarse texture characteristic of crystallinity. The diffractogram shows significant intensities at 3-nm and 10–20-nm wavelengths, which can be assigned to lamellar order of the P3HT chains and their crystalline domain size.[48] In contrast the cross section of the nanotemplated network film (**Figure 3.14(b)**) after PCBM incorporation and removal reveals an ultrafine "curly" texture with no significant correlation between neighboring features. Its diffractogram shows the 10–20-nm feature to be completely suppressed. Therefore the long-range order that is not conducive to efficient exciton dissociation is absent, while the short-range (local) order of the P3HT segments that appears essential for high carrier mobility remains. This demonstrates that phase-coarsening is effectively suppressed. On the other hand, demixed biblend films can exhibit a highly variable texture from ultrafine to coarse depending on film preparation conditions.[14,36,49]

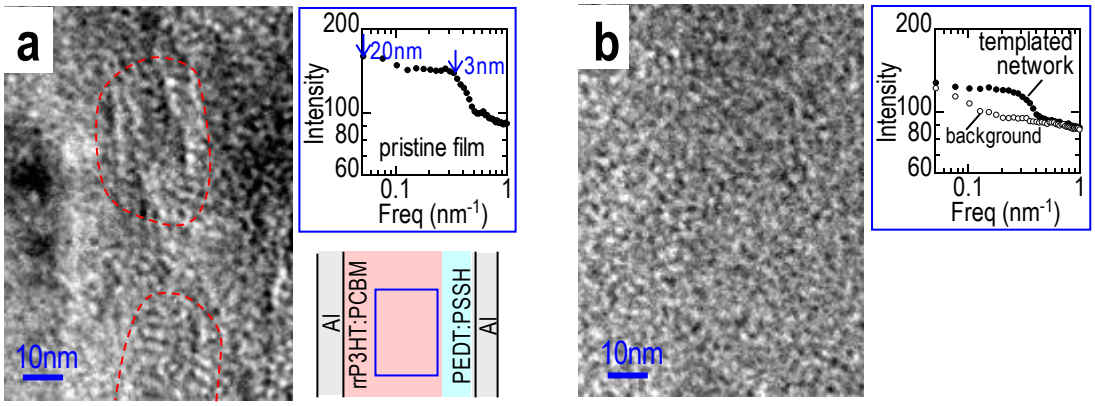

Figure 3.14 HRTEM phase-contrast images of ultrathin sections. **(a)** Pristine P3HT film and **(b)** nanotemplated P3HT network film prepared using same processing as for devices. The images were collected at 200 keV in the weak defocus regime (–100 nm), without sample staining or supporting film. Approximate semicrystalline domain boundaries were marked in **(a)** based on phase coherence as guide to eye. The PCBM nanophase fraction has been extracted with hexane to leave the polymer network intact in **(b).** The diffractograms were obtained by fast Fourier transform of the images and plotted against spatial frequency. The bottom right panel in **(a)** shows a schematic of the film configuration and location of the image (blue box). The Al strip suppresses charging and provides stability for imaging over extended times. A similar film configuration was used for **(b)**.

3.4.3 The mechanism of the PCBM infiltration process

Figure 3.15 outlines essential elements of the mechanism that leads to the key attributes of the network morphology. First the P3HT chains are lightly-crosslinked through their alkyl side chains, primarily in the amorphous regions (**Figure 3.15(a)**). Contact with a solvent causes expansion to a mesh with a length scale given by ~ $\rho^{-1/3}$, which is of the order of 50–35 repeat units here. This provides room for incorporation of the guest molecules (**Figure 3.15(b)**). As the solvent evaporates the polymer network contracts and re-forms local chain segment order which partitions the PCBM into the remaining disordered regions. PCBM has limited solubility

within the ordered P3HT phase[36,50]. This templates the formation of an ultrafine contiguous network that comprises ordered P3HT segments in intimate contact with PCBM. Annealing further improves molecular order within the network, but does not cause coarsening or phase breakup because the crosslinks restrict long-range chain segmental motion. Therefore the first-order network characteristics that are essential for high photo-carrier generation and collection efficiencies can be built in. Furthermore since this is essentially a self-organized heterostructure that is immobilized by crosslinks, its properties are much less dependent on demixing length scales and/or processing conditions.

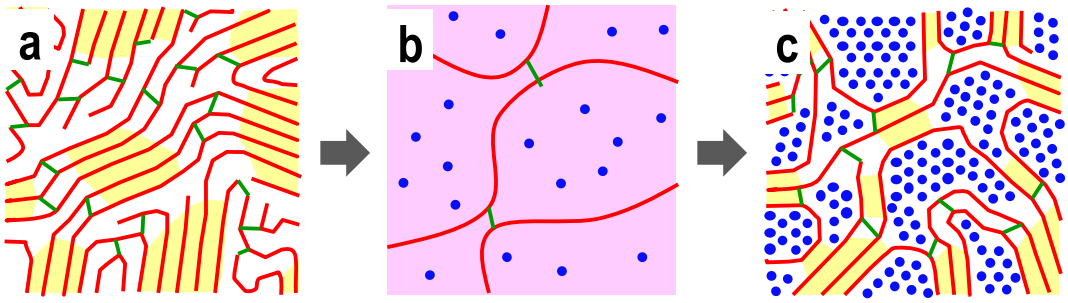

Figure 3.15 Schematic of the formation of the nanotemplated polymer network morphology. **(a)** The polymer (red chains) comprising ordered (yellow) and amorphous domains is lightly-crosslinked (green links) to give an infinite but swellable network. **(b)** This network expands in contact with the solvent to allow for incorporation of guest and solvent molecules into the network. **(c)** As the solvent evaporates the network contracts and becomes templated by the incorporated guest molecules. The properties of the resultant morphology, such as its length scale, order and phase connectivity, are determined by the crosslink density, rather than the solvent and drying conditions.

3.5 Device performance of crosslinked network solar cells

Solar cell devices were fabricated by sandwiching the photoactive layer between poly(3,4-ethylenedioxythiophene): poly(styrenesulfonic acid) (PEDT: PSSH) as the hole collector and

Ca/ Al as the electron collector. **Figure 3.16** shows the current–voltage characteristics of a nanotemplated network and a demixed biblend solar cell with the same P3HT: PCBM ratio (1:1 w/w; i.e., $d_{PCBM}/ d_{P3HT} \approx 0.6$) and the same d = 85 nm, measured under simulated solar radiation at equivalent 1.2 sun (due to the spectral mismatch). The network cell shows a significantly higher J_{sc} (12.6 *vs* 9.9 mA cm^{-2}), a slightly higher V_{oc} (0.63 *vs* 0.61 V) but similar *FF* (0.63) as the biblend cell. As a result, the network cell shows a *PCE* (4.2%) that is 30% higher than the biblend cell (3.2%). This shows that nanotemplated network can significantly improve several aspects of the solar cell characteristics of the P3HT: PCBM system. The direct comparison here between network and biblend devices measured in the same simulator removes the usual uncertainties associated in its calibration.

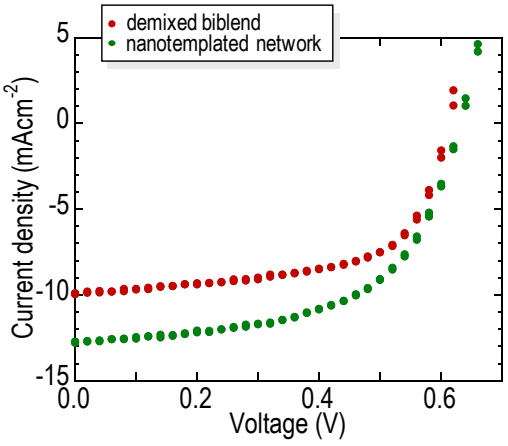

Figure 3.16 Current–voltage characteristics of an optimized demixed biblend device and a nanotemplated polymer network device: d, 85 nm; d_{PCBM}/ d_{P3HT}, 0.56. Device configuration: glass/ ITO/ 50nm PEDT: PSSH/ P3HT: PCBM/ Ca, under an equivalent solar irradiation of 1.2 sun.

3.5.1 Two dimensional *PCE* map

We then fabricated network-P3HT: PCBM cells over a larger composition–thickness space than attempted previously, using a combinatorial approach of doping different amounts of PCBM into crosslinked P3HT films of different thicknesses. **Figure 3.17** reveals the *PCE* landscape plotted against (d_{P3HT}, d_{PCBM}) that we have obtained. The network cells are shown as un-lined, and biblend cells as red-lined color-coded symbols. The biblend cells were only fabricated close to the d_{PCBM}/ d_{P3HT} = 0.6 composition line corresponding to the 1:1 w/w P3HT:PCBM.[50] The contour lines are interpolations using a 2D multi-Gaussian model to guide the eye.

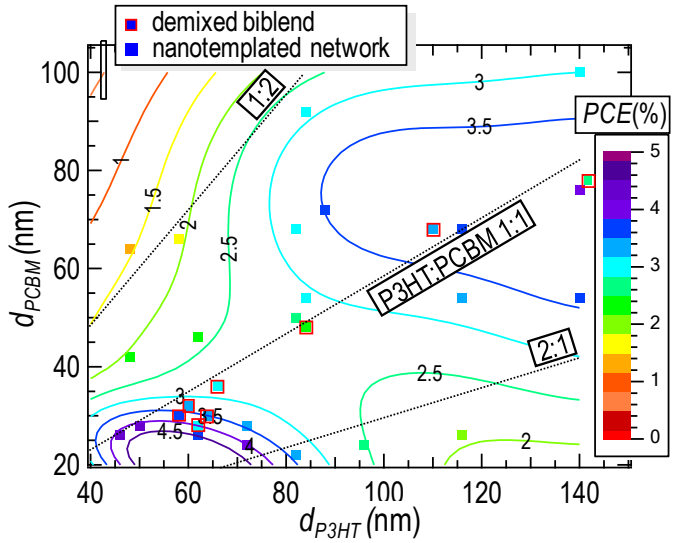

Figure 3.17 Power conversion efficiency *PCE vs* the cell composition and thickness (d_{P3HT}, d_{PCBM}) where d_i is the effective thickness, for nanotemplated polymer network cells (unlined color-coded symbols) and demixed biblend cells (red-lined color-coded symbols). Precision is ±0.15% (absolute). The network cell data are interpolated with a multi-Gaussian surface with a goodness-of-fit $c^2 \approx 1.5$, indicating an excellent model. The biblend data are clearly below this surface by 20 (±10) %. The 1:1 w/w P3HT: PCBM ratio is given by the line $d_{PCBM} = 0.60 * d_{P3HT}$. Other composition lines are as indicated.

The *PCE* surface reveals a high-efficiency ridge that is oriented diagonally near to the d_{PCBM} = 0.6 *d_{P3HT} line, with *PCE* falling off on both sides. Along this ridge, the *PCE* oscillates with film thickness. This oscillation has previously been predicted from the effect of the photonic structure on the absorption of the cell.[8,51] The first and second peaks reach 4.2% centered at (d_{P3HT}, d_{PCBM}) = (60 nm, 25 nm) and 4.0% at (140 nm, 75 nm) respectively, and are separated by a saddle that dips by relatively 30%. Because of this marked dependence on composition and photoactive layer thickness, the cell *PCE*'s have to be compared at matched (d_{P3HT}, d_{PCBM}) to elucidate their intrinsic differences. In this way, the network cells are found to be typically 20% more efficient than the biblend cells. The biblend cells here exhibit give a best *PCE* of 3.4% in the vicinity of the first *PCE* peak, which is similar to the typical optimized values (3.0–3.6%) that have been reported,[4,5,8,14,36,50] although 4–5% have also claimed.[43,52] The optimal P3HT: PCBM ratios in the network cells at each of the two peaks however are similar to those of the demixed biblend film.[4,5,8,14,50] This indicates the local compositions must also be rather similar.

The results here show that relatively high efficiency can be obtained at the second *PCE* peak which is potentially more desirable for manufacturing. The first *PCE* peak occurs in thin films that are challenging to manufacture pinhole-free on large areas. The present carrier mobilities of the P3HT: PCBM system[4] are not high enough to allow larger photoactive layer thicknesses to be usefully employed beyond the second peak.

3.5.2 Two dimensional fill-factor (*FF*) map

The V_{oc} of all the devices fall in the range 0.60±0.03 V, and it turn out to be more dependent on the donor-acceptor ratio rather than the morphology. On the other hand, the J_{sc} Two-dimensional map has no simple functional fitting as it is very dependent on the amount of light absorbed. Thus these two parameters will not be discussed individually, but the internal quantum efficiency, which is a very important indicator for the device performance, will be discussed in section 3.5.4.

Figure 3.18 shows the measured compositional dependence of the fill factor (*FF*), i.e. ratio of maximum electrical power output to the product of J_{sc} and V_{oc} of the cells. This *FF* shows a gradual decrease with increasing film thickness, but a pronounced asymmetry with sharper decrease over the PCBM-poor than P3HT-poor compositions. A decrease of *FF* indicates an increased electric field or voltage dependence of the photocurrent.[37] The gradual reduction in *FF* with *d* is thus to be expected on account of the larger space-charge voltage penalty arising from the larger carrier extraction distances,[38,53] and an additional (weak) field-dependence of the charge-separation step.[54] The asymmetry in its composition dependence however reveals an interesting morphological aspect of these devices. As the film composition becomes PCBM-poor, the PCBM network becomes increasingly poorly connected, which causes the effective electron mobility to fall and the photocurrent to pick up stronger voltage dependence. The converse however does not occur as readily for composition that become P3HT-poor because the P3HT network has already built-in continuity due to the crosslinks.

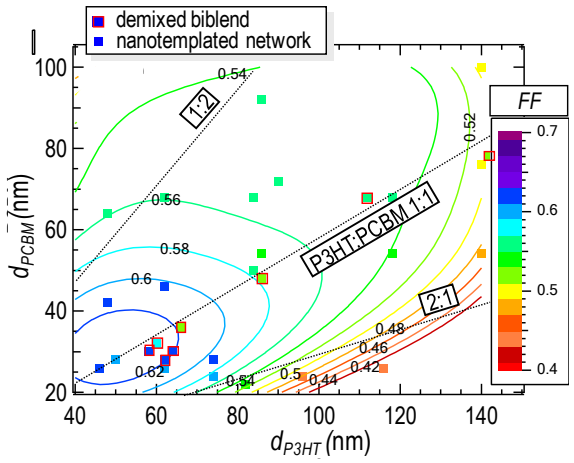

Figure 3.18 Measured composition dependence of the fill factor *FF* for the nanotemplated polymer network cells (un-lined color-coded symbols) and demixed biblend cells (red-lined color-coded symbols). The network cell data are interpolated with a polynomial surface (c^2 = 1.4; excellent goodness-of-fit).

3.5.3 Computed two dimensional power absorption (P_{abs}) and photon flux absorption (Φ_{ph}) map

To evaluate the photonic structure effect of the cells, we used a transfer matrix formalism (details to be shown in Chapter 5) to compute the absorbed photon flux Φ_{ph} in the photoactive layer in the cell. The reflective cathode in particular sets up a weak microcavity that redistributes the optical field within the cell,[8,51,55] which is previously well-known to alter the emission efficiency and radiation profile of organic light-emitting diodes.[56] The complex dielectric functions $\tilde{\varepsilon}(\lambda) = n(\lambda) + \mathrm{i} * k(\lambda)$ of all the layers as well as the spectral irradiance of the solar simulator were known or measured here, where n (λ) and k (λ) are real and imaginary components of the refractive index. We also took into account the compositional dependence of $\tilde{\varepsilon}(\lambda)$ of P3HT: PCBM by interpolating using the Bruggeman effective medium approximation for film compositions that span the (d_{P3HT}, d_{PCBM}) space. The Φ_{ph} was obtained

from Poynting vector analysis, and the integrated power absorbed in the photoactive layer P_{abs} was then computed by spectral integration over the solar spectrum. The key uncertainty lies in $\tilde{\varepsilon}(\lambda)$ of the evaporated cathode, but trial computations using a range of reasonable $\tilde{\varepsilon}(\lambda)$ functions do not change the results by more than 5%.

Figure 3.19(a) shows the dependence of P_{abs} on (d_{P3HT}, d_{PCBM}) for the incident solar power (1.2 sun, due to the spectral mismatch) used in our experiments. This plot clearly shows a marked oscillation with *d* but a weaker dependence on composition particularly for the thicker films. These are the direct consequences of the photonic structure of the cell. The first and second peaks reach 34 mW cm^{-2} at (60 nm, 20 nm) and 38 mW cm^{-2} at (140 nm, 70 nm) respectively, and are separated by a saddle that dips relatively *ca*. 27% along the 1:1 line. These peaks correspond respectively to the emergence of one and two optical field antinodes in the photoactive layer.[38] The second peak approaches the maximum absorption possible (within a few percent) in the photoactive layer, given reflection losses, and the parasitic ITO and PEDT: PSSH absorptions. A key feature here is that despite the large difference in film thicknesses, the P_{abs} of the photonic-structure optimized thin film (80 nm) is only *ca*. 12% lower than the thick film (220 nm), because the strong optical field enhancement in the centre of the thinner film increases its absorption efficiency markedly. The computed diagonal oscillation of the P_{abs} surface and location of its two peaks strikingly resemble those of the *PCE* surface. This is a clear signature of the role of the photonic structure in determining the performance of these solar cells.

The absorbed photon flux Φ_{ph} show exactly the same features (**Figure 3.19(b)**), so it will not be discussed in details.

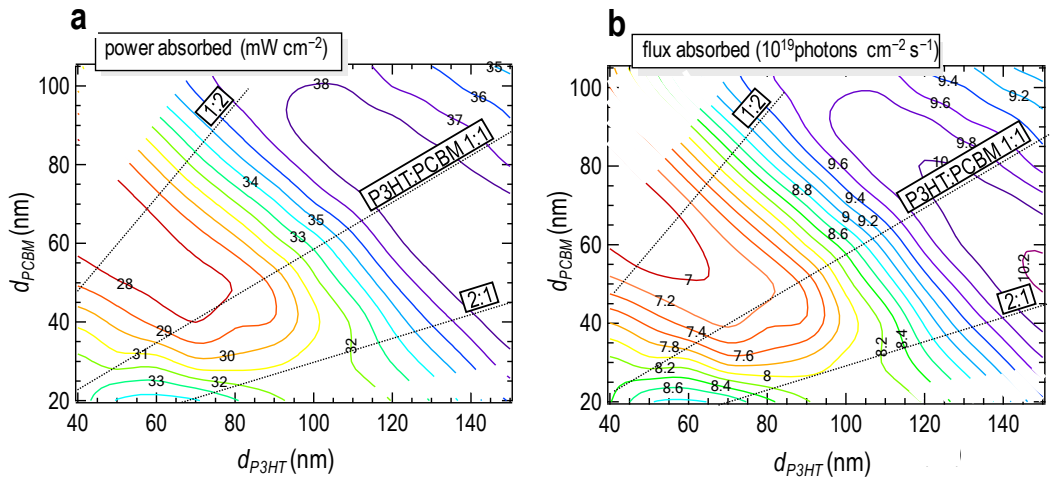

Figure 3.19 (a) Computed composition dependence of absorbed power P_{abs} and **(b)** photon flux Φ_{ph} for the experimental solar irradiance (1.2 sun equivalent due to spectral mismatch).

3.5.4 Two dimensional internal efficiency (*IQE*) map

In this section, we analyze the internal quantum efficiency η_{int} of these cells, i.e., electron collected per photon absorbed, as a measure of the intrinsic photocurrent generation efficiency of the network donor–acceptor heterostructure. This parameter gives the overall (bias-dependent) quantum efficiency for the photo-carrier generation and collection steps, which are both morphology-dependent and separated from the photon-absorption (i.e., exciton-generation) efficiency: $\eta_{IQE} = \eta_{GEN} \cdot \eta_{CC}$, where η_{GEN} is the photo-carrier generation efficiency given by fraction of excitons dissociated to the separated carrier pair, and η_{CC} is the charge collection efficiency given by the fraction collected at the electrodes. We extracted η_{IQE} at short-circuit from the measured J_{sc} according to: $\eta_{IQE} = J_{SC} / (e \cdot \Phi_{ph})$, where e is the elementary charge and Φ_{ph} is the computed photon flux absorbed (ph cm^{-2} s^{-1}) in the photoactive layer.

Figure 3.20 shows these η_{IQE} plotted as a function of (d_{P3HT}, d_{PCBM}). The data again reveal a broad high-efficiency ridge (shaded as a guide to the eye) with an average η_{IQE} of 0.85 that rises marginally to 0.9 in the vicinity of the first *PCE* peak, and falls off at greatly off-optimal compositions. In contrast to the marked thickness-dependent oscillations in the *PCE* and P_{abs} surfaces however, this η_{IQE} ridge is relatively flat and practically independent of thickness. This provides direct experimental evidence that the overall *PCE* of the solar cell can be separated into a photonic structure effect that affects P_{abs} (and Φ_{ph}) and a morphology effect that affects η_{IQE}. The high η_{IQE} attained shows that the nanotemplated network morphology can drive both the photo-carrier generation and collection steps towards near perfect efficiency with surprisingly little recombination losses.

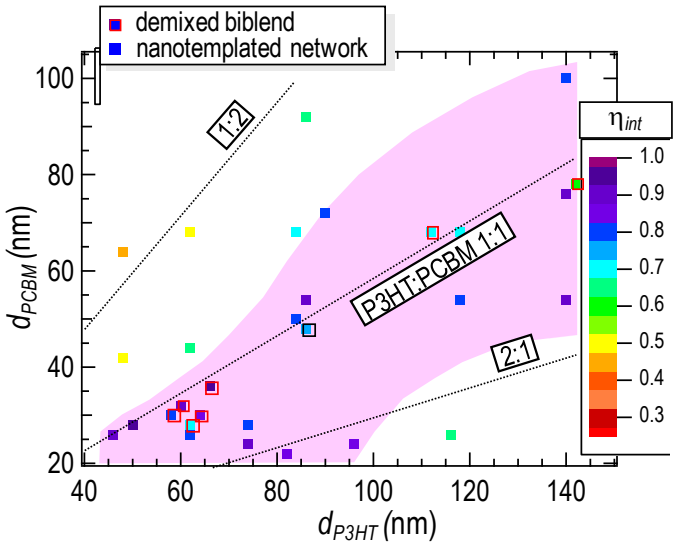

Figure 3.20 Composition dependence of the internal photon-to-electron conversion quantum efficiency η_{IQE} at short-circuit, for nanotemplated network cells (unlined color-coded symbols) and demixed biblend cells (red-lined color-coded symbols). The shaded region is a guide to the eye where $\eta_{IQE} \approx$ 0.85, obtained from the modeled *PCE* and *FF* surfaces together with the computed $\Phi_{ph.}$

In other words, these solar cells are operating very near to their theoretical limit given their fill factor and V_{oc}. For comparison, the demixed biblend films here (red-lined symbols) show a high η_{IQE} in the vicinity of the first *PCE* peak (≈ 0.8) which decreases gradually with increasing *d* to the vicinity of the second peak (≈ 0.6). We suspect this to be due to the difficulty of sustaining the optimal ultrafine contiguous morphology in demixed films across thicker films, resulting in incomplete harvesting of excitons.[57] This is consistent with current–voltage device modeling[58] and very-wide-timescale transient spectroscopy[54,59] results which have respectively suggested that each of the non-geminate and geminate recombination loss fractions can be remarkably low (≈ 0.1) in optimized biblend films. Thus the main effect of the crosslinked network morphology is to push the combined losses even lower, to ≤ 0.1, and over a relatively broader composition–thickness space.

Finally we address the other feature of the η_{IQE} surface which is the efficiency roll-off to the sides of the ridge. This confirms that the marked decrease in *PCE* for off-optimal compositions is not solely due to inefficient photon absorption as sometimes thought, but receives an important contribution from the sub-optimal morphology that arises even in a pre-defined network structure. Deviation of the phase volume fractions from the optimal must eventually increase the required exciton diffusion length and constrict the conduction path of one of the carriers, which would ultimately degrade $\eta_{GEN,}$ η_{CC} and hence η_{IQE}. The combined analysis of the *PCE*, P_{abs}, *FF* and η_{IQE} surfaces here thus reveals direct experimental evidence for the separate contributions of the photonic structure and of the donor–acceptor morphology to the overall efficiency of organic solar cells. The acceptor-templated crosslinked polymer donor network enables the attainment of the ultrafine contiguous donor–acceptor heterojunction that is prerequisite to the separate optimization both of these characteristics. This therefore

provides a clear path for achieving high power conversion efficiencies in other donor–acceptor organic solar cells.

3.5.5 Effects of initial P3HT morphology and processing conditions

There is a question of whether the morphology of the polymer network (distribution of crosslinking points) depends significantly on the processing solvent used to form the initial polymer film. In principle, one may expect that since the crosslinks are formed primarily in the amorphous regions where the crosslinkers are distributed, the resultant network morphology should depend on the crystalline morphology of the initial polymer film (i.e. crystalline phase fraction and form). If the dependence is strong, the donor–acceptor morphology may then be controlled indirectly by the exact solvent processing conditions of the initial polymer film, which may not always be desirable for manufacturing.

We show that that under practical film forming conditions, this effect is in fact negligible. The current–voltage characteristics and power conversion efficiencies (*PCE*), which are strongly related to the donor–acceptor morphology of the crosslinked P3HT: PCBM films, are broadly independent of the solvents used to make the initial P3HT films. The molecularly-templated crosslinked networks show similar high internal quantum efficiency of ca. 0.9, independent of solvent processing conditions (chloroform CF, chlorobenzene CB, and 1,2-dichlorobenzene DCB), in marked contrast to behavior of the usual demixed biblend films. These three solvents are good solvents for regioregular P3HT that span the entire range of vapor pressure that is practical for film formation. At room temperature, their vapor pressures are: CF, 160 mmHg; CB, 12 mmHg; DCB, 1.5 mmHg (normal boiling points: CF, 61^{o}C; CB, 131^{o}C; DCB, 180^{o}C).

The rate of solvent evaporation thus decreases by 2 orders of magnitude from CF to DCB, and hence the time to form more ordered chains increases correspondingly. Indeed we found that electrical behavior and *PCE* of the resultant infiltrated P3HT: PCBM solar cells are not significantly different. Thus the crosslinked polymer methodology does indeed enjoy the advantage of greatly reduced sensitivity of its donor–acceptor network and cell performance to processing conditions.

To establish this, one has to take cognizance of the 1D photonic structure effect as shown in **Figure 3.19**, which causes the absorbed power to vary, strongly in some regions, with (d_{P3HT}, d_{PCBM}). Where the dependence is particularly strong, for example in the vicinity of the first *PCE* peak, a small variation in (d_{P3HT}, d_{PCBM}) can make a large variation in the expected *PCE*. We decided to avoid these regions and their attendant uncertainties by operating close to the saddle point of the high-efficiency *PCE* composition ridge (**Figure 3.17**). We also avoided the second *PCE* peak because of the challenges of spin-casting thick P3HT films from the least volatile solvent (DCB) in the set.

Regioregular P3HT was dissolved together with s-FPA in CF, CB and DCB, to give a polymer concentration of 6.7, 14 and 20 mg mL^{-1} respectively, with 3 w/w% s-FPA (weight of crosslinker to weight of polymer). These solutions were then spin-cast at 2000 rpm (30 s) followed by 4000 rpm (20 s). Because the DCB film is still not completely dry at this stage, all films were further subjected at room temperature to a rough vacuum (< $1x10^{-3}$ mbar). We kept the P3HT film thicknesses within a narrow band by adjusting the solution concentration, so that the film morphology can be compared at nearly constant thickness. [As solvent volatility decreases, the polymer concentration has to be increased quite significantly to counteract the longer drying time and thinning of the solution film.]

The –log(transmittance) spectra (**Figure 3.21 (a)–(c)**) reveal that the different solvents induce slight differences in the chain molecular order within the as spin-cast P3HT films (red curves). The chain order varies as DCB ≈ CF > CB, as judged by the relative intensities of the 0–0 (605 nm), 0–1 (555 nm) and 0–2 (515 nm) vibronic bands and also their band widths. However the differences are small. This shows that varying the solvent volatility by 2 orders of magnitude does not cause chain order to vary significantly, unlike for low molecular-weight analogues. The gel curves are also marginally affected, as evidenced by slightly different film retention after crosslinking and solvent wash (green curves). These show that there is indeed a perceptible morphological difference between films spin-cast from different solvents, as may have been expected. The film thicknesses were 79, 85 and 78 nm respectively.

The films were then contacted with a PCBM solution (for simplicity: 15 mg mL^{-1} for CF film; and 30 mg mL^{-1} for the other films), and spun off at 1500 rpm, 2500 rpm and 3000 rpm respectively over the CF, CB and DCB films, to target a d_{PCBM}/d_{P3HT} ratio within a narrow band of 0.4–0.6, corresponding to the optimal composition on the high-efficiency ridge. Quantitative analysis based resolving the PCBM and P3HT absorption contributions confirm these results (blue curves). This shows that P3HT films prepared from different processing solvents can be similarly infiltrated with PCBM, and hence the methodology is general in this respect. The superior molecular chain order of these P3HT networks over those of the demixed biblend films is again evident (see also **Figure 3.6**).

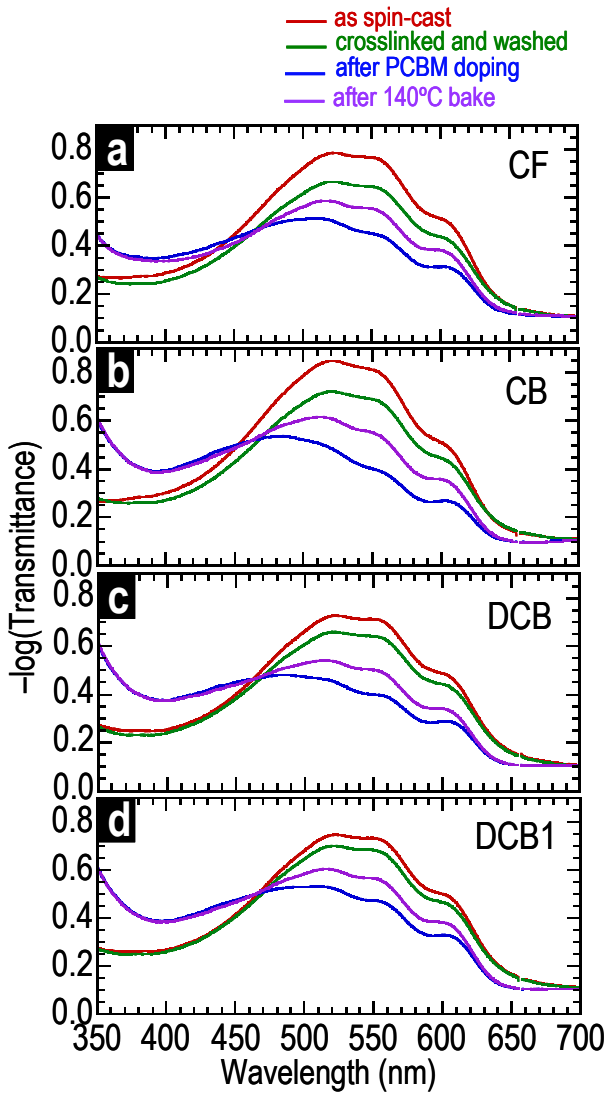

Figure 3.21 –log(Transmittance) spectra for P3HT and crosslinked P3HT:PCBM films processed from different solvents over glass/ ITO/ PEDT:PSSH from: **(a)** chloroform (CF), **(b)** chlorobenzene (CB), and **(c), (d)** 1,2-dichlorobenzene (DCB) solutions. For **(a)–(c)**, the film was washed with CB solvent, for **(d)**, the film was washed with DCB solvent. Legend: Red, as spin-cast P3HT films with $3.7 \times 10^{19} cm^{-3}$ s-FPA crosslinker; green, after photocrosslinking and solvent wash; blue, after PCBM doping by contact spinning with a CB solution; purple, after annealing at 140ºC for 10 min to give the final nanotemplated crosslinked donor–acceptor network (see text). After photocrosslinking and solvent wash, d_{P3HT}: 79 nm (CF), 85 nm (CB), 78 nm (DCB), 83 nm (DCB1). After PCBM doping, d_{PCBM}: 30 nm (CF), 50 nm (CB, DCB, DCB1). Despite initial solvent-induced differences in the polymer chain order in the starting films, the polymer chain order in the final polymer network is practically identical.

The films were then annealed at 140ºC for 10 min in the glove-box to fully develop the final donor–acceptor morphology (purple curves). After this step, the crosslinked P3HT network films that are now doped with PCBM clearly have very similar P3HT π–π^* absorption spectra band shapes. This shows that the P3HT segments in the network have similar molecular order. Thus despite solvent-induced differences in the initial polymer chain order in the starting films, the polymer chain order in the final polymer network is practically identical and rather insensitive to the processing solvent. We have also checked that changing the wash solvent from CB to DCB to give the sample denoted DCB1 does not significantly change the electronic spectrum of the crosslinked and nanotemplated P3HT network either (**Figure 3.21 (d)**).

The CF, DCB and DCB1 films then evaporated with Ca/ Al to give 8 solar cell pixels each, and then illuminated at 1.0 sun. The results corrected for spectral mismatch, under AM1.5 standard test conditions, gave average *PCE* values of 3.3, 3.0 and 3.2% respectively (precision, ±0.15%) for devices in this saddle region. These lie on the *PCE* surface that has been modeled from the high-efficiency crosslinked P3HT: PCBM data produced using CB as the processing solvent (**Figure 3.22(a)**). Despite the marked change in processing conditions, the electrical characteristics of the solar cells are not significantly different. Therefore the performance of these cells are determined by their (d_{P3HT}, d_{PCBM}) coordinates, independent of processing solvents. The internal quantum efficiencies (*IQE*) were then computed as before taking into account of the photon flux absorbed in the photoactive layer. The results give *IQE* of 0.8–0.85 in this region, which again are much higher *IQE* was obtained than the usual demixed biblend films (0.65–0.7), and are in fact commensurate with the high-efficiency ridge deduced from the CB films previously discussed in **Figure 3.17** and **Figure 3.20** (see in **Figure 3.22**).

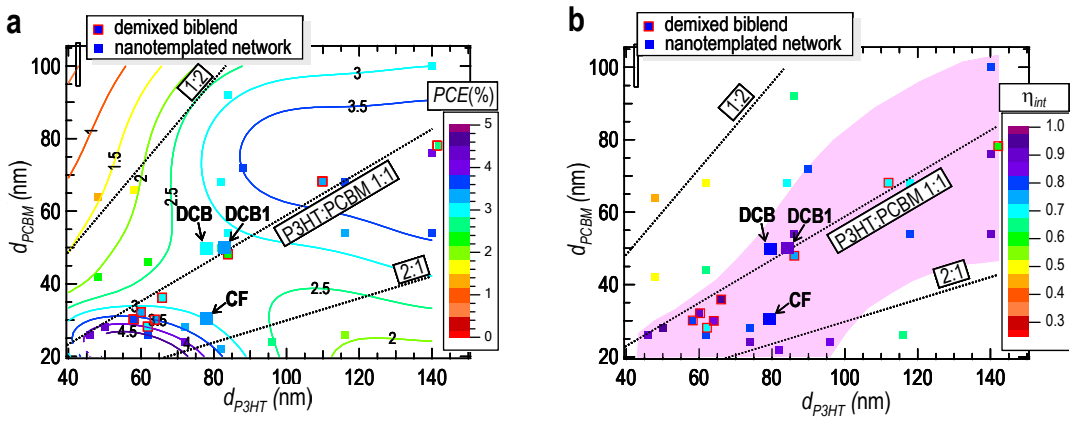

Figure 3.22 Change in processing solvents and conditions does not affect the efficiency of the crosslinked network solar cells. **(a)** *PCE* landscape, and **(b)** *IQE* landscape. These figures are taken from **Figure 3.17** and **Figure 3.20**, superposed with the data obtained for the CF, DCB and DCB1 devices. Despite the marked change in processing conditions, the *PCE, IQE* and electrical characteristics of the solar cells are not significantly different. This shows that the donor–acceptor morphology of these nanotemplated and lightly crosslinked P3HT: PCBM films are rather insensitive to the processing solvent and the initial polymer film morphology.

Therefore it is firmly established here the donor–acceptor morphology of these nanotemplated and lightly crosslinked P3HT: PCBM films are markedly insensitive to the processing solvents and the initial polymer film morphology. Despite the large variation in solvent volatility and drying time tested, the properties of the final crosslinked P3HT: PCBM network is practically identical, based on optical spectroscopy and the *IQE* for photocurrent generation which is highly sensitive to the donor–acceptor morphology. This overcomes a key challenge to the large-scale fabrication of nanostructured films with controlled morphology.

3.6 Conclusions

We have successfully applied the crosslinking method to control the heterojunction formation process from solution, and solar cell devices have been fabricated and characterized based on P3HT: PCBM system. The HRTEM results show that the domain size of crosslinked P3HT is finer than that of uncrosslinked P3HT. Device performance characterization reveals generally 20-30% higher *PCE* of crosslinked network solar cells compared with conventional blend devices. We attribute this improvement to the continuous polymer phase, which increase the hole collection efficiency, and the ultrafine phase separation, which may increase the charge generation efficiency. The internal quantum efficiency has been demonstrated to be more than 85% for a wide range of crosslinked network devices, indicating a near ideal morphology.

3.7 References

1 Blom, P. W. M., Mihailetchi, V. D., Koster, L. J. A. & Markov, D. E. Device physics of polymer: fullerene bulk heterojuction solar cells. *Adv. Mater.* **19**, 1551-1566 (2007).

2 Brabec, C. J. *et al.* Polymer-fullerene bulk-heterojunction solar cells. *Adv. Mater.* **22**, 3839-3856 (2010).

3 Moulé, A. J. & Meerholz, K. Morphology Control in Solution‐Processed Bulk‐Heterojunction Solar Cell Mixtures. *Adv. Funct. Mater.* **19**, 3028-3036 (2009).

4 Mihailetchi, V. D., Xie, H., de Boer, B., Koster, L. J. A. & Blom, P. W. M. Charge transport and photocurrent generation in poly(3-hexylthiophene):methanofullerene bulk heterojunction solar cells. *Adv. Funct. Mater.* **16**, 699-708 (2006).

5 Li, G. *et al.* "Solvent annealing" effect in polymer solar cells based on poly(3-hexylthiophene) and methanofullerenes. *Adv. Funct. Mater.* **17**, 1636-1644 (2007).

6 Peet, J. *et al.* Efficiency enhancement in low-bandgap polymer solar cells by processing with alkane dithiols. *Nature Mater.* **6**, 497-500 (2007).

7 Chirvase, D., Parisi, J., Hummelen, J. & Dyakonov, V. Influence of nanomorphology on the photovoltaic action of polymer–fullerene composites. *Nanotechnol.* **15**, 1317 (2004).

8 Moulé, A. J., Bonekamp, J. B. & Meerholz, K. The effect of active layer thickness and composition on the performance of bulk-heterojunction solar cells. *J. Appl. Phys.* **100**, 094503 (2006).

9 Chen, D., Nakahara, A., Wei, D., Nordlund, D. & Russell, T. P. P3HT/PCBM bulk heterojunction organic photovoltaics: Correlating efficiency and morphology. *Nano Lett.* (2011).

10 Kim, Y. Y. *et al.* A strong regioregularity effect in self-organizing conjugated polymer films and high-efficiency polythiophene:fullerene solar cells. *Nature Mater.* **5**, 197-203 (2006).

11 Coffey, D. C. & Ginger, D. S. Time-resolved electrostatic force microscopy of polymer solar cells. *Nature Mater.* **5**, 735-740 (2006).

12 Campoy-Quiles, M. *et al.* Morphology evolution via self-organization and lateral an vertical diffusion in polymer:fullerene solar cell blends. *Nature Mater.* **7**, 158-164 (2008).

13 Burkhard, G. F., Hoke, E. T., Scully, S. R. & McGehee, M. D. Incomplete exciton harvesting from fullerenes in bulk heterojunction solar cells. *Nano Lett.* **9**, 4037-4041 (2009).

14 van Bavel, S. S., Bärenklau, M., de With, G., Hoppe, H. & Loos, J. P3HT/PCBM bulk heterojunction solar cells: impact of blend composition and 3D morphology on device performance. *Adv. Funct. Mater.* **20**, 1458-1463 (2010).

15 Groenendaal, L. B., Jonas, F., Freitag, D., Pielartzik, H. & Reynolds, J. R. Poly(3,4-ethylenedioxythiophene) and Its derivatives: past, present, and future. *Adv. Mater.* **12**, 481-494 (2000).

16 Greenham, N. C., Moratti, S. C., Bradley, D. D. C., Friend, R. H. & Holmes, A. B. Efficient light-emitting diodes based on polymers with high electron-affinities. *Nature* **365**, 628-630 (1993).

17 Halls, J. J. M. *et al.* Efficient photodiodes from interpenetrating polymer networks. *Nature* **376**, 498-500 (1995).

18 Ho, P. K. H. *et al.* Molecular-scale interface engineering for polymer light-emitting diodes. *Nature* **404**, 481-484 (2000).

19 Müller, C. D. *et al.* Multi-colour organic light-emitting displays by solution processing. *Nature* **421**, 829-833 (2003).

20 Solomeshch, O. *et al.* Wide band gap cross-linkable semiconductor polymer LED. *Synth. Met.* **157**, 841-845 (2007).

21 Charas, A. *et al.* Photoacid cross-linkable polyfluorenes for optoelectronics applications. *Synth. Met.* **158**, 643-653 (2008).

22 Cheng, Y. J. *et al.* Thermally cross-linkable hole-transporting materials on conducting polymer: synthesis, characterisation and applications for polymer light-emitting devices. *Chem. Mater.* **20**, 413-422 (2008).

23 Klärner, G. *et al.* Cross-linkable polymers based on dialkylfluorenes. *Chem. Mater.* **11**, 1800-1805 (1999).

24 Keana, J. F. W. & Cai, S. X. New reagents for photoaffinity labeling: synthesis and photolysis of functionalized perfluorophenyl azides. *J. Org. Chem.* **55**, 3640-3647 (1990).

25 Cai, S. X., Keana, J. F. W., Nabity, J. C. & Wybourne, M. N. Conducting polymers as deep-uv and electron beam resists: direct production of micrometer scale conducting structures from poly(3-octylthiophene). *J. Molecular Electron.* **7**, 63-68 (1991).

26 Schnapp, K. A., Poe, R., Leyva, E., Soundararajan, N. & Platz, M. S. Exploratory photochemistry of fluorinated aryl azides: implications for the design of photoaffinity labeling reagents. *Bioconjugate Chem.* **4**, 172-177 (1993).

27 Cai, S. X., Glenn, D. J., Kanskar, M., Wybourne, M. N. & Keana, J. F. W. Development of highly efficient deep-uv and electron beam mediated cross-linkers: synthesis and photolysis of bis(perfluorophenyl) azides. *Chem. Mater.* **6**, 1822-1829 (1994).

28 Liu, L., Engelhard, M. H. & Yan, M. Surface and interface control on photochemically initiated immobilisation. *J. Am. Chem. Soc.* **128**, 14067-14072 (2006).

29 Khong, S. H. *et al.* General photo-patterning and post-deposition modification of polyelectrolyte thin films via efficient ionic bis(fluorinated phenyl azide) photo-crosslinkers. *Adv. Funct. Mater.* **17**, 2490-2499 (2007).

30 Png, R. Q. *et al.* Electromigration of the conducting polymer in organic semiconductor devices and its stabilization by crosslinking. *Appl. Phys. Lett.* **91**, 013511 (2007).

31 Collings, J. C. *et al.* Arene-perfluoroarene interactions in crystal engineering. Part 3: Single-crystal structures of 1:1 complexes of octafluoronaphthalene with fused-ring polyaromatic hydrocarbons. *New J. Chem.* **25**, 1410-1417 (2001).

32 Png, R. Q. *et al.* High-performance polymer semiconducting heterostructure devices by nitrene-mediated photocrosslinking of alkyl side-chains. *Nature Mater.* **9**, 152-158 (2010).

33 Hugger, S., Thomann, R., Heinzel, T. & Thurn-Albrecht, T. Semicrystalline morphology in thin films of poly(3-hexylthiophene). *Colloid Polym. Sci.* **2004**, 932-938 (2004).

34 Rispens, M. T. *et al.* Influence of the solvent on the crystal structure of PCBM and the efficiency of MDMO-PPV: PCBM 'plastic'solar cells. *Chem. Commun.*, 2116-2118 (2003).

35 Clark, J., Silva, C., Friend, R. H. & Spano, F. C. Role of intermolecular coupling in the photophysics of disordered organic semiconductors: aggregate emission in regioregular polythiophene. *Phys. Rev. Lett.* **98**, 206406-206401-206404 (2007).

36 Chen, D. A., Nakahara, A., Wei, D. G., Nordlund, D. & Russell, T. P. P3HT/PCBM bulk heterojunction organic photovoltaics: correlating efficiency and morphology. *Nano Lett.* **11**, 561-567 (2011).

37 Koster, L. J. A., Smits, E. C. P., Milhailetchi, V. D. & Blom, P. W. M. Device model for the operation of polymer/ fullerene bulk heterojunction solar cells. *Phys. Rev. B* **72**, 085205 (2005).

38 Liu, B., Png, R. Q. & Ho, P. K. H. New Organic solar cell design rule: Influence of non-uniform exciton generation profile and charge carrier mobility on organic solar cell performance. (2012).

39 Ho, P. K. H., Kim, J. S., Tessler, N. & Friend, R. H. Photoluminescence of poly(p-phenylenevinylene)-silica nanocomposites: evidence for dual emission by Franck-Condon analysis. *J. Chem. Phys.* **115**, 2709-2720 (2001).

40 Liu, B. & Ho, P. K. H. Unpublished. (2011).

41 Vaynzof, Y. *et al.* Surface-directed spinodal decomposition in poly(3-hexylthiophene) and C61-butyric acid methyl ester blends. *ACS Nano* **5**, 329-336 (2011).

42 Yang, X. *et al.* Nanoscale morphology of high-performance polymer solar cells. *Nano. Lett.* **5**, 579-583 (2005).

43 Ma, W., Yang, C., Gong, X., Lee, K. & Heeger, A. J. Thermally stable, efficient polymer solar cells with nanoscale control of the interpenetrating network morphology. *Adv. Funct. Mater.* **15**, 1617-1622 (2005).

44 Kim, J. S. *et al.* High‐Efficiency Organic Solar Cells Based on Preformed Poly (3‐hexylthiophene) Nanowires. *Adv. Funct. Mater.* **21**, 480-486 (2011).

45 Chen, H. Y. *et al.* Fast-grown interpenetrating network in poly (3-hexylthiophene): methanofullerenes solar cells processed with additive. *J. Phys. Chem. C* **113**, 7946-7953 (2009).

46 Hugger, S., Thomann, R., Heinzel, T. & Thurn-Albrecht, T. Semicrystalline morphology in thin films of poly (3-hexylthiophene). *Colloid Polym. Sci.* **282**, 932-938 (2004).

47 Samitsu, S., Shimomura, T., Heike, S., Hashizume, T. & Ito, K. Effective production of poly (3-alkylthiophene) nanofibers by means of whisker method using anisole solvent: structural, optical, and electrical properties. *Macromolecules* **41**, 8000-8010 (2008).

48 Kline, R. J., McGehee, M. D. & Toney, M. F. High oriented crystals at the buried interface in polythiophene thin-film transistors. *Nature Mater.* **5**, 222-228 (2006).

49 Moulé, A. J. & Meerholz, K. Morphology control in solution-processed bulk-heterostructure solar cell mixtures. *Adv. Funct. Mater.* **19**, 3028-3036 (2009).

50 Müller, C. *et al.* Binary organic photovoltaic blends: a simple rationale for optimum compositions. *Adv. Mater.* **20**, 3510-3515 (2008).

51 Dennler, G., Scharber, M. C. & Brabec, C. J. Polymer:fullerene bulk-heterojunction solar cells. *Adv. Mater.* **2009**, 1323-1338 (2009).

52 Irwin, M. D., Buchholz, D. B., Hains, A. W., Chang, R. P. H. & Marks, T. J. p-Type semiconducting nickel oxide as an efficiency-enhancing anode interfacial layer in polymer bulk-heterojunction solar cells. *Proc. Natl. Acad. Sci.* **105**, 2783-2787 (2008).

53 Mihailetchi, V. D., Wildeman, J. & Blom, P. W. M. Space-charge limited photocurrent. *Phys. Rev. Lett.* **94**, 126602 (2005).

54 Marsh, R. A., Hodgkiss, J. M. & Friend, R. H. Direct measurement of electric field-assisted charge separation in polymer:fullerene photovoltaic diodes. *Adv. Mater.* **22**, 3672–3676 (2010).

55 Hoppe, H., Arnold, N., Meissner, D. & Sariciftci, N. Modeling of optical absorption in conjugated polymer/fullerene bulk-heterojunction plastic solar cells. *Thin Solid Films* **451**, 589-592 (2004).

56 Kim, J. S., Ho, P. K. H., Greenham, N. C. & Friend, R. H. Electroluminescence emission pattern of organic light-emitting diodes: Implications for device efficiency calculations. *J. Appl. Phys.* **88**, 1073-1081 (2000).

57 Burkhard, G. F., Hoke, E. T., Scully, S. R. & McGehee, M. D. Incomplete exciton harvesting from fullerenes in bulk heterojunction solar cells. *Nano Lett.* **9**, 4037-4041 (2009).

58 Mihailetchi, V. D. *et al.* Origin of the enhanced performance in poly (3-hexylthiophene):[6, 6]-phenyl C-butyric acid methyl ester solar cells upon slow drying of the active layer. *Appl. Phys. Lett.* **89**, 012107 (2006).

59 Howard, I. A., Mauer, R., Meister, M. & Laquai, F. Effect of morphology on ultrafast free carrier generation in polythiophene: fullerene organic solar cells. *J. Am. Chem. Soc.* **132**, 14866-14876 (2010).

Chapter 4. Built-in potential of bulk heterojunction solar cells

In this chapter we employ the electroabsorption spectroscopy (Stark spectroscopy) to characterize the build in potential (V_{bi}) of the crosslinked network devices and conventional blend devices. The accurate measurement of V_{bi} is fundamental to the understanding of the device physics and possible loss mechanism, which is described by the drift-diffusion model in next chapter.

4.1 Built-in potential in organic electronic devices

The mechanism of voltage loss is of the same importance as photocurrent loss, but the origin of the open circuit voltage (V_{oc}) in bulk heterojunction solar cells is still unclear. It has been found that the open circuit voltage is limited by the molecular energy levels of the heterojunction components[1-5] or the charge transfer states.[6-9] More mechanism needs to be understood to explain the dependence on light intensity[10] and the fabrication conditions given the same heterojunction components.[11-13] Large variations exist when reporting the HOMO and LUMO of the heterojunction components. For example, the reported HOMO of rrP3HT varies between -4.6 and -5.0eV due to different methods and material properties,[1,14-16] and LUMO of PCBM varies between -3.7 and -4.3eV.[1,11,17,18]

The work function (WF) of a metal and the ion potential (IP) of an organic semiconductor relative to vacuum level can be accurately measured by Ultraviolet Photoelectron Spectroscopy (UPS). However, when the metal and semiconductor are placed in contact, their interfacial potential could be altered by exchange, correlation charge transfer, and covalent

bonds formation.[19-21] This junction can have either rectifying or non-rectifying characteristics, which describes the linearity and symmetry of the current–voltage (I-V) curve. The junction is called Ohmic contact or Schottky barrier contact, respectively.

The energy level alignment of a metal and a semiconductor is shown in **Figure 4.1**. The re-arrangement at the interface may cause the formation of interfacial dipole, or termed as vacuum level shift.[22] This vacuum level shift and the hole injection barrier (ϕ_{Bp}) can be derived from UPS data.

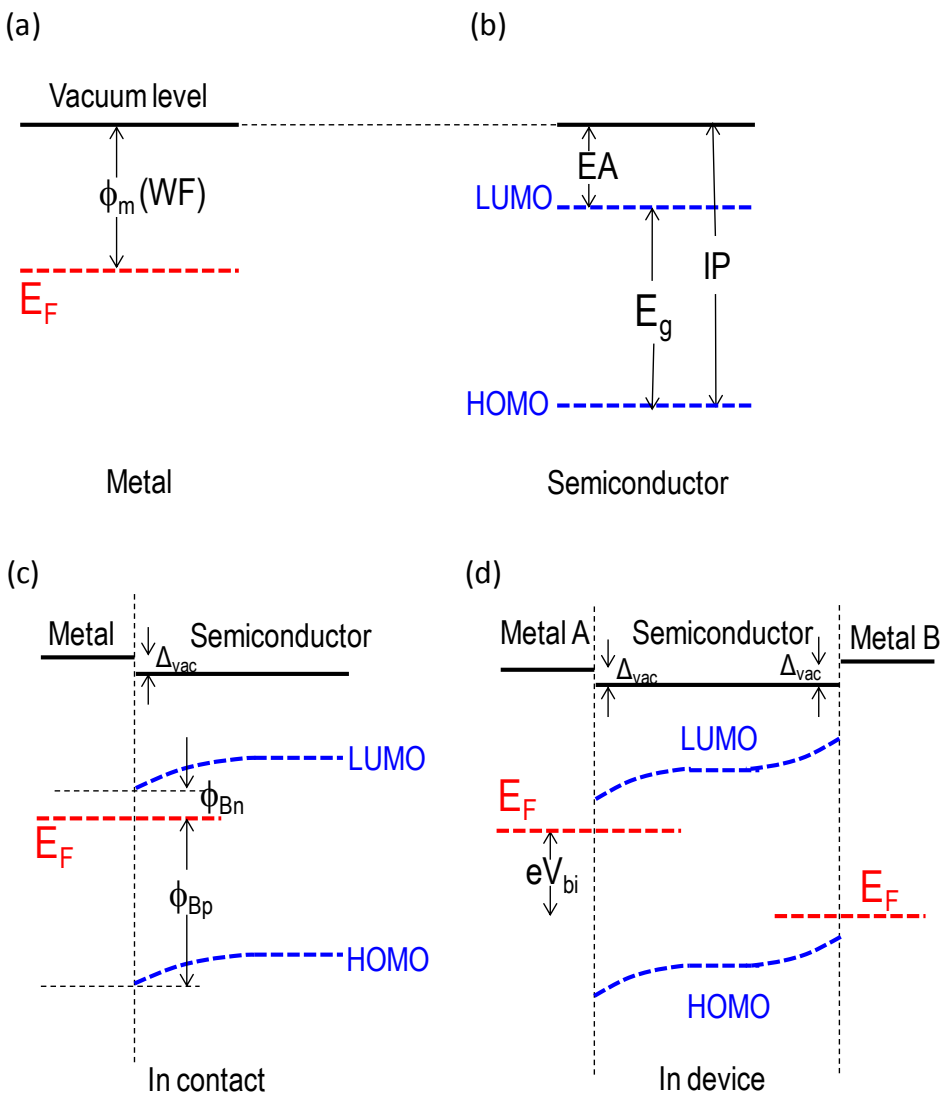

Figure 4.1 Energy diagram of a Metal- Organic semiconductor interface. **(a)** and **(b)** when separated and share the same vacuum level. **(c)** When brought in contact, with a vacuum level shift, ϕ_{Bp} and ϕ_{Bn} are the electron and hole barriers, respectively. **(d)** In an actual device, the V_{bi} is determined by the energy level alignment at the two contacts.

Considering a device with the semiconductor sandwiched by two metal contacts with different work function (V_{bi} =0 for same contacts), the V_{bi} is the combinative result of the energy level alignment of both contacts and even the organic semiconductor. The complicated physics and chemistry at Metal/Organic interface make it difficult to predict the interfacial properties and

performance simply from the work function and EA of separately material. Several mechanisms were proposed to explain the substantial deviations from the ideal Schottky–Mott picture,[23] such as charge exchange, metal surface modification by adsorbed molecules and Fermi level pinning by chemistry-induced states.[24-26]

Despite the unclear picture of energy level alignment at Metal/Organic interface, it can be inferred from the built-in potential (Vbi), corresponding to the flat-band condition, which is the upper limit of V_{oc}. The accurate measurement of V_{bi} is of great importance because we cannot evaluate the voltage loss mechanism (V_{bi}-V_{oc}) in OPV devices without it.

4.2 Theory and setup of Electroabsorption spectroscopy

Electroabsorption spectroscopy (Stark spectroscopy or EA spectroscopy) has been demonstrated as an effective technique to accurately determine the built-in potential in a complete OLED device, [27-30] but it has not been reported on OPV devices yet due to the difficulty to interpret the spectra when the active layer is changed from single component to a bulk heterojunction. Our work in demonstrating the V_{bi} in P3HT: PCBM solar cell devices is unprecedented.

EA spectroscopy measures changes in the optical constants caused by an external field. This effect is known as Stark effect, referring to the splitting and shifting of the spectral lines (energy states) of atoms and molecules due to the presence of a static external electric field. It is an electric analogue of Zeeman Effect where a spectral line splitting is due to the presence of a magnetic field. However, this effect is very weak and it requires lock-in techniques to pick up the signal.

The electroabsorption response of a solid film is proportional to the imaginary part of the third order susceptibility, $\mathrm{Im}\chi^{(3)}(h\nu)$, which is not dependent on electric field, and the square of the electric field[31]

$$\Delta\alpha(h\nu) \propto -\frac{\Delta T}{T}(h\nu)(or\ \frac{\Delta R}{R}) \propto \mathrm{Im}\chi^{(3)}(h\nu)\cdot E^2$$

where α is the absorption coefficient, hv is the photon energy, T is the transmission, R is the reflection and E is the electric field. An important trick here is to use a modulation technique to reduce the order of the electric field from 2 to 1 by introducing an AC bias on the DC electric field. The total electric field is

$$E = E_{DC} + E_{AC}\cos(\omega t)$$

Expanding the expression, we get

$$\Delta\alpha(h\nu) \propto \mathrm{Im}\chi^{(3)}(h\nu)\cdot[\frac{1}{2}\cdot E_{AC}^2(1+\cos(2\omega t)) + 2E_{AC}E_{DC}\cos(\omega t) + E_{DC}^2]$$

The modulated signal at the fundamental frequency of the applied AC bias is

$$\Delta\alpha(h\nu,\omega) \propto \mathrm{Im}\chi^{(3)}(h\nu)\cdot 2E_{AC}E_{DC}\cos(\omega t)$$

And the second harmonic signal is

$$\Delta\alpha(h\nu,2\omega) \propto \mathrm{Im}\chi^{(3)}(h\nu)\cdot\frac{1}{2}\cdot E_{AC}^2(1+\cos(2\omega t))$$

The actual electric field in the sample is the summation of the external field and built-in field,

$$E_{DC} = E_{applied} + E_{bi}$$

By sweeping the $V_{applied}$ one can determine that

$$V_{bi} = -V_{applied}$$

when the $\Delta\alpha(h\nu,\omega)$ is nullified.

It is worth mentioning that the modulated electroabsorption signal contains not only the changes in the optical constant, which is related to the electric field, but also the signal due to

photobleaching and charge induced absorption, etc. The interfacial charges, traps and non-uniform electric field due to the space charge could also cause difficulties in interpreting the data. It is better to conduct the measurements at 30K to avoid those complexities, although the measurements at room temperature are known to be consistent with low temperature measurements in some cases.[32]

The schematic diagram of the home-built rig for electroabsorption is shown in **Figure 4.2.**[32] Monochromatic light beam is generated from a 50W quartz-tungsten-halogen lamp and a monochromator (Newport Cornerstone 260, F /3.9, model # 74100), then directed and focused onto the device, which is placed inside a variable-temperature cryostat (10-300 K, APD HC-2). Chamber pressure below 10^{-6} Torr is maintained during the measurement by a turbo-molecular pump system. A sinusoidal drive voltage V=Vdc +Vac (ω= 1kHz) is applied on the device while the reflected light is demodulated by the lock-in amplifier (Stanford Research, SR830) to obtain the in-phase and quadrature component with respect to the excitation voltage. The measurement and data collection process is automatically controlled by Labview.

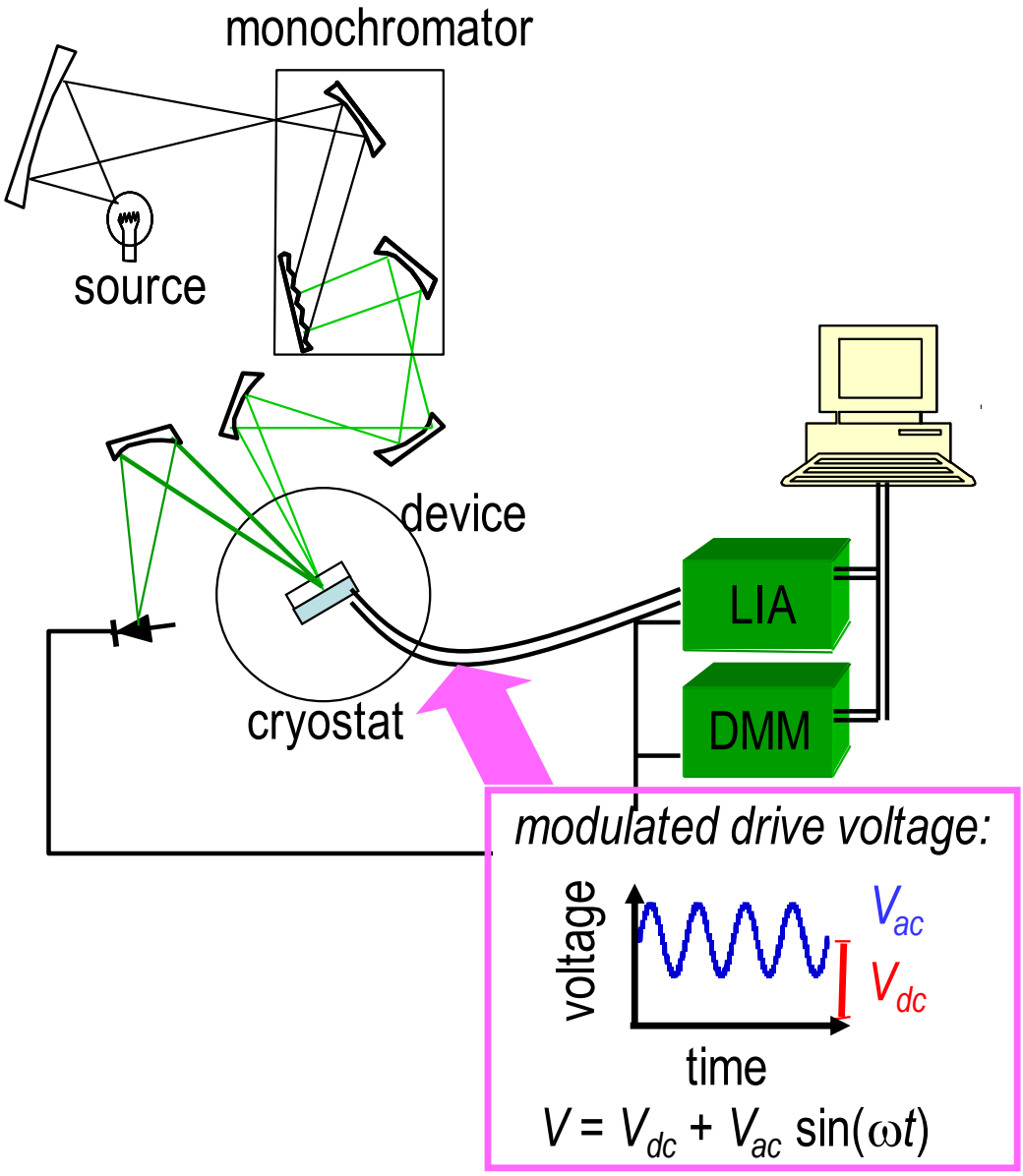

Figure 4.2 Experimental schematic of the electroabsorption spectroscopy

4.3 Electroabsorption spectroscopy of P3HT diodes and PCBM diodes

The reference EA spectrum of PCBM diode and P3HT diode were collected at 30K first, as shown in **Figure 4.3**. The PCBM diode structure consist of glass/ ITO/ PEDOT: PSSH/ PS: PCBM (1:4)/ Ca/ Al, and the PCBM is mixed with 20 wt% of polystyrene to form a more uniform

film during spin casting. Two stark peaks can be clearly identified at 2.25eV and 2.5eV (2.4~2.6 broad peak), and the built-in potential is determined to be 1.7V as the Stark peaks vanish. Since Fermi-level (E_F) pinning does not occur at the PEDT/ PCBM contact, vacuum-level alignment prevails there, and so the negative polaron (P^-) level of PCBM lies 1.7 eV above the E_F of PEDT: PSSH (5.2 eV), at 3.5 eV.

The P3HT diode has a similar structure to PCBM diode, glass/ ITO/ PEDOT:PSS/ P3HT/ Ca/ Al, besides the Stark peaks at 1.95, 2.15, 2.35 and 2.6eV, there are electric field independent sub-gap features extending out the $\boldsymbol{\pi}$-$\boldsymbol{\pi}^*$ absorption region. This broad sub-gap absorption is demonstrated to be the modulation on the interface charge transfer layer between PEDOT: PSSH and P3HT.[33,34] The Stark peaks do not vanish at zero-field, and the built-in potential is judged to be 1.0V based on the inversion of the peak polarity. Since E_F is pinned at this *h* contact at 4.2 eV,[35] the P^- level of P3HT lies *ca*. 1.0 V above this, and so at *ca*. 3.2 eV, which is 0.3 eV higher than that of PCBM. When $V_a = V_{bi}$, the EA spectrum of P3HT is dominated by the sub-gap polaron absorption of P3HT (broad band at 1.15–1.9 eV)[36,37] due to modulation of the δ-hole density at the ohmic contact,[33] together with the assciated bleaching of $\pi-\pi^*$ transitions, which give structured bands at 1.98 and 2.2 eV. The main Stark band of the P3HT exciton thus overlaps exactly with a narrower underlying bleached $\pi-\pi^*$ band.

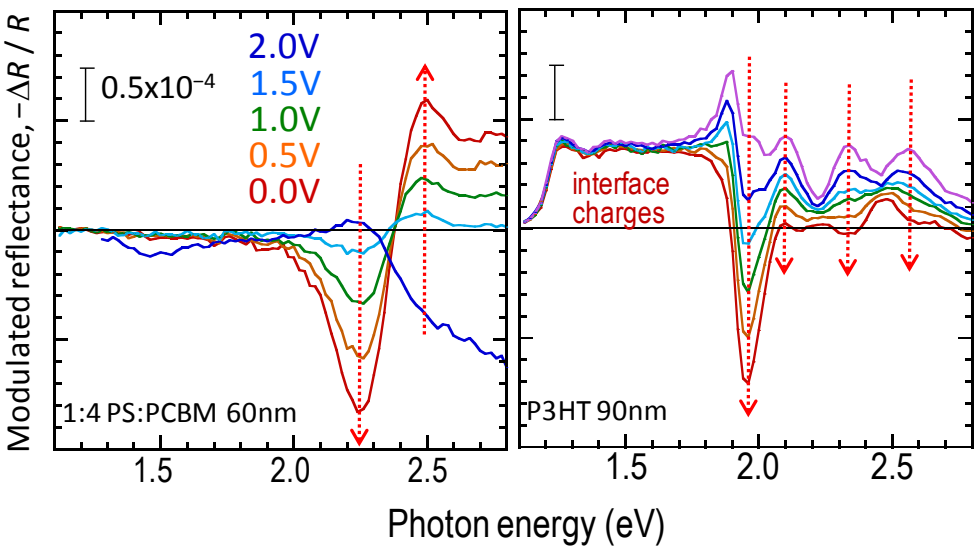

Figure 4.3 EA spectra of PCBM diode and P3HT diode at 30K. Left: 1:4 PS: PCBM diode, total thickness 60nm. The applied DC voltage steps from 2.0V to 0.0V, and the AC amplitude is 0.5V, same conditions for all EA measurements. Right: P3HT diode, thickness 90nm.

4.4 Electroabsorption spectroscopy of P3HT: PCBM solar cells

Identifying the Stark peaks of P3HT and PCBM is helpful to interpret the EA spectra of actual P3HT PCBM blend or crosslinked network devices. The EA spectrum of P3HT PCBM solar cells contains not only the components from P3HT and PCBM, but also the absorption of the charge transfer states, and photo-induced charges. Thus the analysis can be only based on the inversion of the Stark peaks polarity. Take note that the Stark peak of PCBM at 2.4~2.6eV has the opposite polarity to all other Stark peaks, making it easier to recognize, especially in the PCBM rich devices, e.g. device **(a)**, **(b)** and **(d)** in **Figure 4.4**, while in the P3HT rich device **(b)**, the P3HT Stark peaks (1.95eV and 2.15eV) and their polarity inversion can be recognized. For example, in a device with a P3HT: PCBM 1:2 w/w PCBM-rich film, we could observe the Stark spectrum of PCBM in the 2.3–2.7-eV region. The dc-bias dependent spectra suggest

field polarity inversion occurs at 0.75–1.0 V. In a device with a 2.5:1 P3HT-rich film, we could observe the Stark spectrum of P3HT in the 1.7–2.1-eV region. The spectra suggest field polarity inversion occurs at 0.75 V. Taken together the data suggests the V_{bi} occurs in the P3HT: PCBM devices the vicinity of 0.75 V, broadly independent of composition in the tested range. Although these measurements were performed at 30 K, previous work has shown that the V_{bi} of OSC diodes are robust and do not change noticeably with temperature.[34,38]

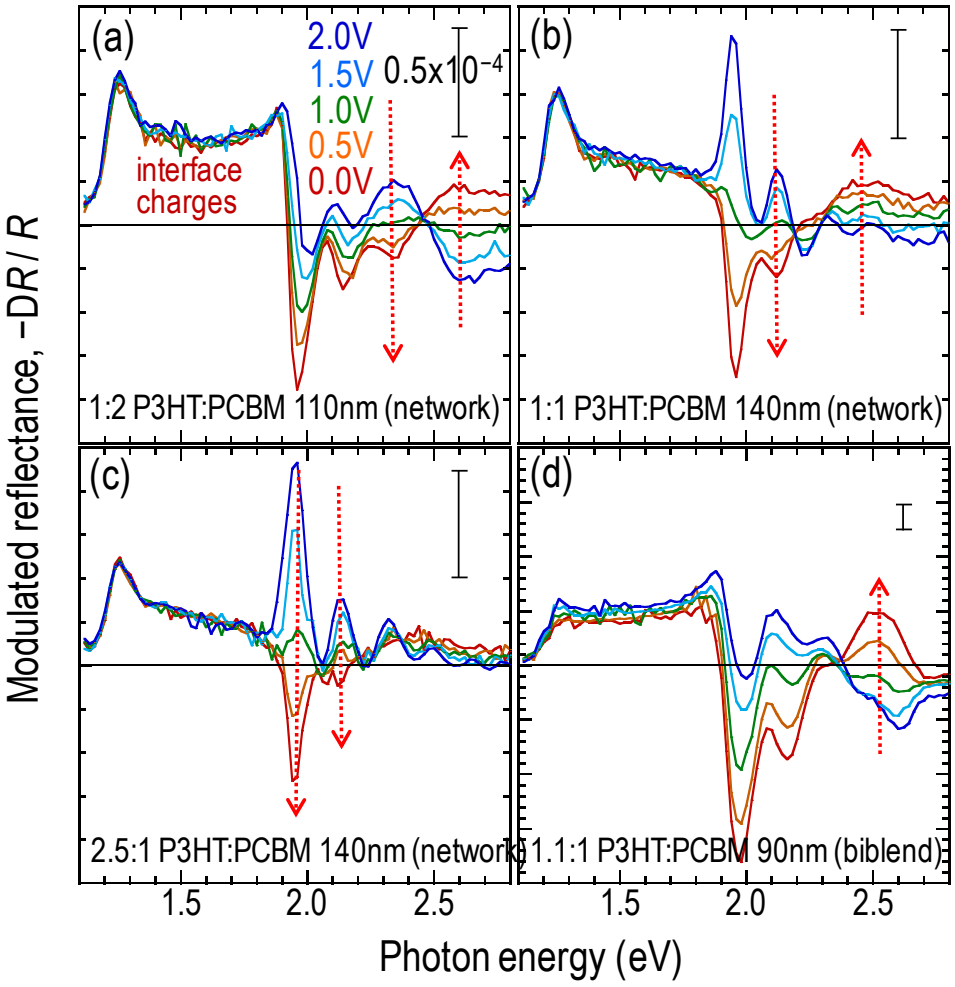

Figure 4.4 EA spectra of PCBM both blend and crosslined network P3HT: PCBM solar cell devices. **(a)-(c).** EA spectrum of crosslinked network P3HT: PCBM device, weight ratio 1:2, total thickness 110nm, crosslinked network P3HT: PCBM device, weight ratio 1:1, total thickness 140nm, crosslinked

network P3HT: PCBM device, weight ratio 2.5:1, total thickness 140nm. **(d).** EA spectrum of blend P3HT: PCBM device, weight ratio 1.1:1, total thickness 90nm.

To verify that V_{bi} is indeed 0.75 V, we measured the illuminated *JV* characteristics (1.2-sun) as a function of temperature to find the photocurrent neutrality point. This is the V_a where the photocurrent switches direction, and has been used to determine V_{bi} through a modulation technique.[34] To observe the photocurrent free from the injection current, the measurements have to be performed at low temperatures where injection is strongly suppressed. **Figure 4.5** shows the variable temperature *JV* characteristics collected for a crosslinked P3HT network: PCBM solar cell. As temperature decreases from room temperature to below 150 K, the forward-bias injection current shuts down completely, and the V_{oc} shifts from the usual 0.63 V at room temperature to 0.73 V. The *JV* curves also become symmetric about V_{oc}, with no further change in V_{oc} below 150 K. The same result was obtained for spin-cast biblend films. Therefore it can be firmly concluded that the V_{bi} of PEDT: PSSH/ P3HT: PCBM/ Ca cells is 0.75±0.05 V. The open-circuit voltage deficit, which is the difference between V_{bi} and V_{oc}, is thus very small, only 0.1–0.15 V, at room temperature.

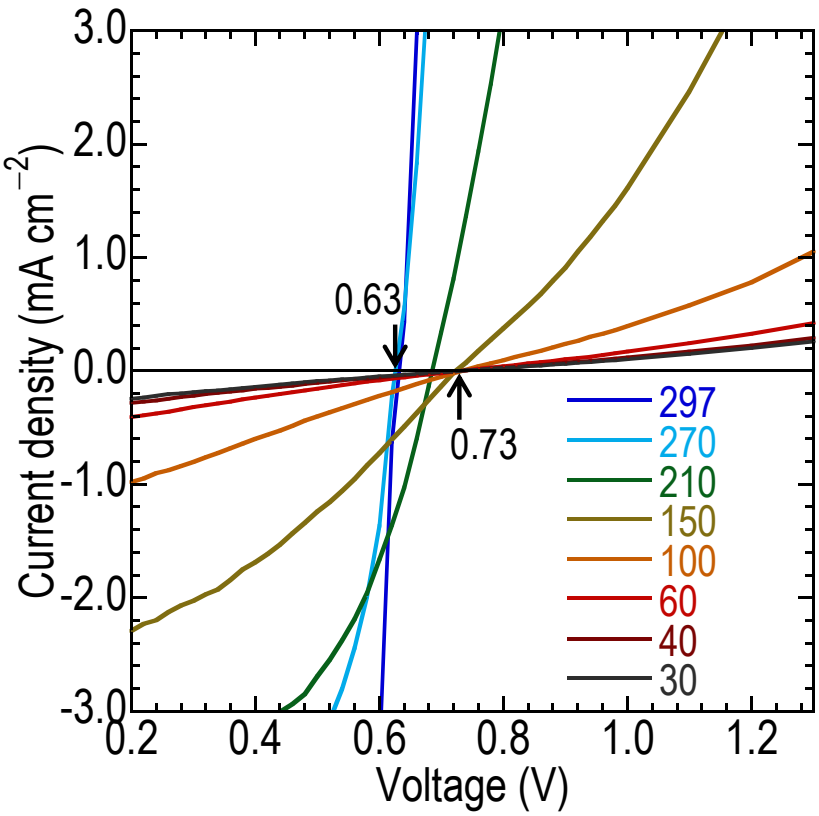

Figure 4.5 Low-temperature *J-V* measurements.

The effective work functions that contribute to this V_{bi} are markedly different from the vacuum work function difference and may be fixed by the respective *e* and *h* polaron levels in the case contact Fermi level E_F pinning, as occurs in the PEDT:PSSH/ P3HT: PCBM/ Ca system. The vacuum work function of the *h* collection electrode (PEDT:PSSH, 5.2 eV)[33] is considerably deeper than the ionization potential of P3HT donor (4.7 eV),[35] while that of the evaporated *e* collection electrode in contact with an organic film (Ca, 2.4 eV)[38] is considerably smaller than the electron affinity of the PCBM acceptor (estimated, 3.4 eV). Therefore the contacts are heavily δ-doped, and V_{bi} of the cell is pinned.[33]

This V_{bi} value has great implications on the balance between injection and photo-generated current, as will be discussed in Chapter 5.

4.4 Conclusions

We have conducted the electroabsorption spectroscopic measurements on both crosslinked and blend P3HT: PCBM solar cells for the first time to determine the built-in potential, which is a very important parameter in understanding the interface and device physics. The built-in potential has been shown to be 0.75±0.05V, in contrary to the previously believed 1.1±0.1V. This result has a huge influence on the device modeling, as will be discussed in next chapter.

4.5 References

1 Scharber, M. C. *et al.* Design rules for donors in bulk-heterojunction solar cells - towards 10% energy-conversion efficiency. *Adv. Mater.* **18**, 789-794 (2006).

2 Brabec, C. J. *et al.* Origin of the open circuit voltage of plastic solar cells. *Adv. Funct. Mater.* **11**, 374-380 (2001).

3 Gadisa, A., Svensson, M., Andersson, M. R. & Inganäs, O. Correlation between oxidation potential and open-circuit voltage of composite solar cells based on blends of polythiophenes/fullerene derivative. *Appl. Phys. Lett.* **84**, 1609 (2004).

4 Kooistra, F. B. *et al.* Increasing the open circuit voltage of bulk-heterojunction solar cells by raising the LUMO level of the acceptor. *Org. Lett.* **9**, 551-554 (2007).

5 Mutolo, K. L., Mayo, E. I., Barry, P., Forrest, S. R. & Thompson, M. E. Enhanced open-circuit voltage in subphthalocyanine/C60 organic photovoltaic cells. *J. Am. Chem. Soc.* **128**, 8108-8109 (2006).

6 Rand, B. P., Burk, D. P. & Forrest, S. R. Offset energies at organic semiconductor heterojunctions and their influence on the open-circuit voltage of thin-film solar cells. *Phys. Rev. B* **75**, 115327 (2007).

7 Schueppel, R. *et al.* Optimizing organic photovoltaics using tailored heterojunctions: A photoinduced absorption study of oligothiophenes with low band gaps. *Phys. Rev. B* **77**, 085311 (2008).

8 Veldman, D., Meskers, S. C. J. & Janssen, R. A. J. The Energy of Charge‐Transfer States in Electron Donor–Acceptor Blends: Insight into the Energy Losses in Organic Solar Cells. *Adv. Funct. Mater.* **19**, 1939-1948 (2009).

9 Veldman, D. *et al.* Triplet formation from the charge-separated state in blends of MDMO-PPV with cyano-containing acceptor polymers. *Thin Solid Films* **511**, 333-337 (2006).

10 Koster, L., Mihailetchi, V., Xie, H. & Blom, P. Origin of the light intensity dependence of the short-circuit current of polymer/fullerene solar cells. *Appl. Phys. Lett.* **87**, 203502 (2005).

11 Mihailetchi, V., Blom, P., Hummelen, J. & Rispens, M. Cathode dependence of the open-circuit voltage of polymer: fullerene bulk heterojunction solar cells. *J. Appl. Phys.* **94**, 6849 (2003).

12 Kim, Y. *et al.* Composition and annealing effects in polythiophene/fullerene solar cells. *J. Mater. Sci.* **40**, 1371-1376 (2005).

13 Li, G. *et al.* "Solvent annealing" effect in polymer solar cells based on poly(3-hexylthiophene) and methanofullerenes. *Adv. Funct. Mater.* **17**, 1636-1644 (2007).

14 Mihailetchi, V. D., Xie, H., de Boer, B., Koster, L. J. A. & Blom, P. W. M. Charge transport and photocurrent generation in poly(3-hexylthiophene):methanofullerene bulk heterojunction solar cells. *Adv. Funct. Mater.* **16**, 699-708 (2006).

15 Ballantyne, A. M. *et al.* Studies of highly regioregular poly (3‐hexylselenophene) for photovoltaic applications. *Adv. Mater.* **19**, 4544-4547 (2007).

16 Tsoi, W. C. *et al.* Effect of Crystallization on the Electronic Energy Levels and Thin Film Morphology of P3HT: PCBM Blends. *Macromolecules* (2011).

17 Akaike, K. *et al.* Ultraviolet photoelectron spectroscopy and inverse photoemission spectroscopy of [6, 6]-phenyl-C61-butyric acid methyl ester in gas and solid phases. *J. Appl. Phys.* **104**, 023710-023710-023715 (2008).

18 Osikowicz, W., de Jong, M. P. & Salaneck, W. R. Formation of the Interfacial Dipole at Organic‐Organic Interfaces: C60/Polymer Interfaces. *Adv. Mater.* **19**, 4213-4217 (2007).

19 Dannetun, P. *et al.* Interface formation betwen poly(2,5-diheptyl-p-phenylenevinylene) and calcium: implications for light-emitting diodes. *Synth. Met.* **67**, 133-136 (1994).

20 Salaneck, W. R. & Brédas, J. L. The metal-on-polymer interface in polymer light emitting diodes. *Adv. Mater.* **8**, 48-52 (1996).

21 Kahn, A., Koch, N. & Gao, W. Electronic structure and electrical properties of interfaces between metals and π - conjugated molecular films. *J. Polym. Sci. Part B Polym. Phys.* **41**, 2529-2548 (2003).

22 Ishii, H., Sugiyama, K., Ito, E. & Seki, K. Energy level alignment and interfacial electronic structures at organic/ metal and organic/ organic interfaces. *Adv. Mater.* **11**, 605-625 (1999).

23 Hill, I. G., Rajagopal, A., Kahn, A. & Hu, Y. Molecular level alignment at organic semiconductor-metal interfaces. *Appl. Phys. Lett.* **73**, 662-664 (1998).

24 Hwang, J. H., Wan, A. & Kahn, A. Energetics of metal-organic interfaces: new experiments and assessment of the field. *Mater. Sci. Eng. R* **64**, 1-31 (2009).

25 Braun, S., Salaneck, W. R. & Fahlman, M. Energy-level alignment at organic/ metal and organic/ organic interfaces. *Adv. Mater.* **21**, 1-23 (2009).

26 Koch, N. Organic electronic devices and their functional interfaces. *Chem. Phys. Chem.* **8**, 1438-1455 (2007).

27 Campbell, I. H., Hagler, T. W., Smith, D. L. & Ferraris, J. P. Direct measurement of conjugated polymer electronic excitation energies using metal/ polymer/ metal structures. *Phys. Rev. Lett.* **76**, 1900-1903 (1996).

28 Brown, T. M. *et al.* Efficient electron injection in blue-emitting polymer light-emitting diodes with LiF/Ca/Al cathodes. *Appl. Phys. Lett.* **79**, 174-176 (2001).

29 Lane, P. A., deMello, A. J., Fletcher, R. B. & Bernius, M. Electric field screening in polymer light-emitting diodes. *Appl. Phys. Lett.* **83**, 3611-3613 (2003).

30 Brewer, P. J. *et al.* Role of electron injection in polyfluorene-based light emitting diodes containing PEDOT:PSS. *Phys. Rev. B* **71**, 205209 (2005).

31 Aspnes, D. & Rowe, J. Resonant nonlinear optical susceptibility: Electroreflectance in the low-field limit. *Phys. Rev. B* **5**, 4022 (1972).

32 Zhou, M. *Energy Level Alignment in Semiconducting Organic Electronic Devices* Ph. D. thesis, National University of Singapore, (2010).

33 Zhou, M. *et al.* The role of delta-doped interfaces for Ohmic contacts to organic semiconductors. *Phys. Rev. Lett.* **103**, 036601-036601-036604 (2009).

34 Zhou, M. *et al.* Determination of the interface δ-hole density in a blue-emitting organic semiconductor diode by electromodulated absorption spectroscopy. *Appl. Phys. Lett.* **97**, 113505 (2010).

35 Zhao, L. H. *et al.* Polarisation effects on energy-level alignment of polymer organic semiconductor films at interfaces. *Appl. Phys. Lett.* **101**, 053304 (2012).

36 Sirringhaus, H. *et al.* Two-dimensional charge transport in self-organized, high-mobility conjugated polymers. *Nature* **401**, 685-688 (1999).

37 Brown, P. J. *et al.* Effect of interchain interactions on the absorption and emission of poly(3-hexylthiophene). *Phys. Rev. B* **67**, 064203 (2003).

38 Zhou, M. *et al.* Effective work functions for the evaporated metal/organic semiconductor contacts from in-situ diode flatband potential measurements. *Appl. Phys. Lett.* **101**, 013501-013501-013504 (2012).

Chapter 5. Modeling and optimization of bulk heterojunction solar cells

In chaper 3, we have demonstrated new approaches to tackle the morphology challenge in polymer: polymer solar cells through phase-directed organization of the heterostructure,[1] and also polymer: fullerene cells through acceptor-doping of crosslinked polymer donor networks.[2] In this chapter, we discuss the new insights gained from detailed modeling of high internal-quantum efficiency cells based on crosslinked P3HT network: PCBM. These cells are remarkable because they show a consistent bulk-distributed heterostructure characterized by an ultrafine but contiguous donor–acceptor morphology over a wide thickness and composition space.[2] Instead of treating V_{bi} as a fitting parameter in the model, we have measured it experimentally, as discussed in chapter 4. This greatly reduces the uncertainty in the fitted carrier density at the contacts. We could thus quantitatively validate the standard device model that comprises separate electrical[3-5] and optical[5-10] stages, and refine its parameters, for the current-density–voltage (*JV*) characteristics of P3HT: PCBM cells measured in the dark and under solar irradiance. Previously attempts have been complicated by the evolving donor–acceptor morphology with thickness and composition.

We investigated the P3HT: PCBM system because this is the most well-studied organic photoactive layer (PAL), and remains one of the most interesting with unsurpassed internal quantum efficiency η_{int}, i.e., fraction of *e* (and *h*) collected in the external circuit per absorbed photon in the PAL approaching *ca*. 0.9 across a wide thickness and composition space.[2]

Nevertheless, in view of recent interest also in low bandgap PALs that show higher η_{int}, we have generalized the model predictions also to these systems.

The rest of this chapter is organized as follows: Section **5.1** describes the optical model, its parameterization and experimental validation. Section **5.2** describes the electrical model, its parameterization, and the experimental validation of the complete optical−electrical model. We focus here less on methodology, which has been covered by other authors in detail, but on insights and their implications for device optimization. Section **5.3** describes a computational study of the transport optimization of highly-efficient organic solar cells based on the calibrated device model. Section **5.4** does likewise for optical-structure optimization. Section **5.5** concludes the chapter.

5.1 Optical model, parameterization and validation

It is widely anticipated that the optical absorption and the exciton generation within the active layer can be well predicted from the real and imaginary components of the refractive index spectra of the layers. It is well known, for example from the work of organic light-emitting diodes that the metal cathode deposited on the active layer reflects considerable amount of incident light, and causes photonic effect in the photo active layer, where a half-space model already suffices to account for the key features of the emissive properties of the device.[11] The predictions of the half-space model has subsequently been validated by full structure calculations of the devices.[12]

A particularly important consequence for organic solar cells is the prediction of strong oscillation of the *PCE* with PAL thickness.[6,7,13] This has however turned out to yet to be

experimentally verified due to the strong coupling of the phase morphology of the spontaneously demixed biblend films with morphology which prevents the unencumbered observation of the photonic structure effect. We show here that this can now be observed in solar cells that have fixed imposed donor–acceptor morphology. This allows the photonic structure effect to be isolated from the morphology effect, and so it becomes possible to confidently extract the internal quantum efficiency, a fundamental parameter of the solar cell. It also provides motivation for careful analysis of the implications of non-uniform exciton generation rate on device characteristics.

5.1.1 Optical transfer matrix formulism

In optics and acoustics, the transfer matrix method is commonly used to study the propagation of electromagnetic and acoustic waves in a layered medium.[7] For example, anti-reflective coatings and dielectric mirrors are based on these principles.

The refraction (transmission) and reflection of light at a single interface between two media is nicely described by Fresnel equations. However, considering a wave propagating via multiple interfaces, as shown in **Figure 5.1**,the reflection between two interfaces is partially transmitted and partially reflected for many times. These inner reflections can interfere destructively or constructively depending on the ratio of the exact path length to the wavelength. The overall reflection (transmission) of the layered structure is the sum of an infinite number of reflections (transmissions), which is troublesome to calculate.

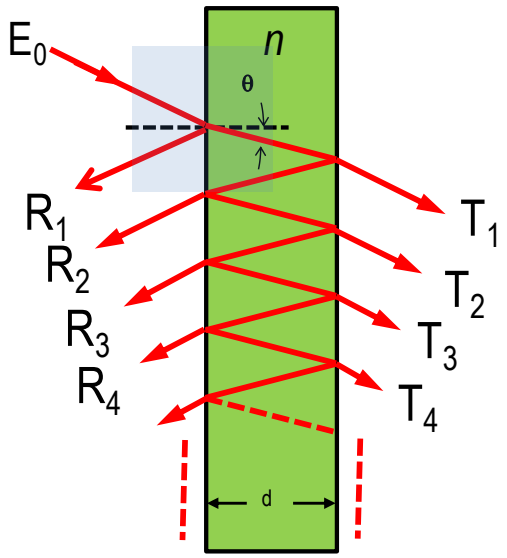

Figure 5.1 Propagation of light through a layer.

The transfer-matrix method is based on the simple continuity conditions for the electric and magnetic fields in the same media or across boundaries from one medium to the next, as revealed by Maxwell's equations. Thus the fields at two different points of a multi layer structure can be connected by a series of matrix operations, as will be shown later.

For simplicity, only normally incident planar waves will be discussed, as the solar cell devices are usually characterized in this way. It can be generalized to more complex cases, such as incidence at any angle and media with magnetic properties. Assuming the layers stack normal to the z axis and taking note that the field within the stack of layers can be represented as the superposition of a forward and backward traveling waves with wave number k_1,

$$E(z) = E_{1f}e^{i\boldsymbol{k_1}z} + E_{1b}e^{-i\boldsymbol{k_1}z} \ldots\ldots (1)$$

For *forward* (right) traveling planar wave,

$$\eta = \frac{\mathrm{E_x}}{\mathrm{H_y}} = \frac{\mathrm{E_y}}{\mathrm{H_x}} = \frac{E_f}{H_f} \ldots\ldots (2)$$

And for *backward* (left) traveling planar wave,

$$\eta = -\frac{\mathrm{E_x}}{\mathrm{H_y}} = -\frac{\mathrm{E_y}}{\mathrm{H_x}} = -\frac{E_b}{H_b} \cdots\cdots (3)$$

Where η is the wave impedance. For the materials used in organic solar cells, the conductivity is low: $\sigma \ll \omega\varepsilon$, and the permeability μ_r =1 at optical frequencies. So

$$\eta = \sqrt{\frac{i\omega\mu}{\sigma + i\omega\varepsilon}} \approx \sqrt{\frac{\mu}{\varepsilon}}$$

$$= \sqrt{\frac{\mu_r}{\varepsilon_r}} * \sqrt{\frac{\mu_0}{\varepsilon_0}} = \sqrt{\frac{\mu_r}{\varepsilon_r}} * \eta_0 = \frac{1}{\sqrt{\mu_r \varepsilon_r}} * \eta_0 = \frac{1}{\boldsymbol{n}} * \eta_0 = \frac{1}{\boldsymbol{n}} \cdots\cdots (4)$$

Where η_0 is the wave impedance in free space, $\eta_0 \approx 377\Omega$, and this constant is omitted in the calculation. $\boldsymbol{n}$ is the complex refractive index, $\boldsymbol{n} = n + \boldsymbol{i}k$, where *n* is the refractive index and *k* is the extinction coefficient.

In a single layer as shown in **Figure 5.2**, the electric and magnetic field at the end point (E_2, H_2) can be derived from that at the incident point (E_1,H_1):

$$\begin{cases} E_2 = E_{1f} e^{ik_1 d_1} + E_{1b} e^{-ik_1 d_1} \\ H_2 = \dfrac{E_{1f}}{\eta_1} e^{ik_1 d_1} - \dfrac{E_{1b}}{\eta_1} e^{-ik_1 d_1} \end{cases} \cdots\cdots (5)$$

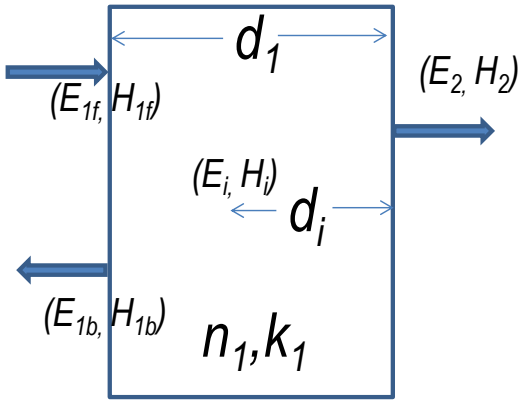

Figure 5.2 Schematic diagram showing electric/ magnetic field at layer boundaries.

Where the k_1 is the complex wave number, $k_1 = 2\pi * \boldsymbol{n}/\lambda$, and d_1 is the distance between two points. The phase shift is used for simplicity, $\delta = k_1 * d_1$, so rewriting the equations in the matrix forms:

$$\begin{bmatrix} E_2 \\ H_2 \end{bmatrix} = \begin{bmatrix} e^{i\delta} & e^{-i\delta} \\ e^{i\delta}/\eta_1 & -e^{-i\delta}/\eta_1 \end{bmatrix} \begin{bmatrix} E_{1f} \\ E_{1b} \end{bmatrix} \cdots\cdots (6)$$

The relationship between the fields and their forward and backward traveling components at any point is described by the following (let δ =0),

$$\begin{bmatrix} E_i \\ H_i \end{bmatrix} = \begin{bmatrix} 1 & 1 \\ 1/\eta_1 & -1/\eta_1 \end{bmatrix} \begin{bmatrix} E_{if} \\ E_{ib} \end{bmatrix} \cdots\cdots (7)$$

Combining equations (6) and (7):

$$\begin{bmatrix} E_i \\ H_i \end{bmatrix} = \begin{bmatrix} 1 & 1 \\ 1/\eta_1 & -1/\eta_1 \end{bmatrix} \begin{bmatrix} e^{i\delta} & e^{-i\delta} \\ e^{i\delta}/\eta_1 & -e^{-i\delta}/\eta_1 \end{bmatrix}^{-1} \begin{bmatrix} E_2 \\ H_2 \end{bmatrix}$$

$$= \begin{bmatrix} 1 & 1 \\ 1/\eta_1 & -1/\eta_1 \end{bmatrix} \frac{\eta_1}{2} \begin{bmatrix} e^{-i\delta}/\eta_1 & e^{-i\delta} \\ e^{i\delta}/\eta_1 & -e^{i\delta} \end{bmatrix} \begin{bmatrix} E_2 \\ H_2 \end{bmatrix} = \begin{bmatrix} \cos\delta & -i\eta_1 \sin\delta \\ -i/\eta_1 \sin\delta & \cos\delta \end{bmatrix} \begin{bmatrix} E_2 \\ H_2 \end{bmatrix}$$

$$= M \begin{bmatrix} E_2 \\ H_2 \end{bmatrix} \cdots\cdots (8)$$

Where

$$M = \begin{bmatrix} \cos\delta & -i\eta_1 \sin\delta \\ -i/\eta_1 \sin\delta & \cos\delta \end{bmatrix} \cdots\cdots (9)$$

and

$$M_{11} = M_{22} = cos\,\delta,\ M_{12} = -i\eta_1 sin\,\delta,\ M_{21} = -i/\eta_1\, sin\,\delta \cdots\cdots (10)$$

Assuming the amplitude of the incident wave to be E_0, the field at incident point and transmitted point can be written with the complex amplitude transmittance and reflectance:

$$\begin{cases} E_1 = E_0 + rE_0 \\ H_1 = n_L(1-r)E_0 \end{cases} \cdots\cdots (11)$$

$$\begin{cases} E_2 = tE_0 \\ H_2 = n_R tE_0 \end{cases} \cdots\cdots (12)$$

Where n_L and n_R are the complex refraction index for the left-most and right-most media. Comparing equations (8), (11) and (12):

$$\begin{cases} 1 + r = t(M_{11} + M_{12}n_R) = tp_1 \\ n_L(1-r) = t(M_{21} + M_{22}n_R) = tp_2 \end{cases} \cdots\cdots (13)$$

Where

$$P = M * \begin{bmatrix} 1 \\ n_R \end{bmatrix}, or \begin{cases} p_1 = (M_{11} + M_{12}n_R) \\ p_2 = (M_{21} + M_{22}n_R) \end{cases} \cdots\cdots (14)$$

Solving (13):

$$r = \frac{\frac{p_2}{p_1} - n_L}{\frac{p_2}{p_1} + n_L}, t = \frac{1+r}{p_1} \cdots\cdots (15)$$

After r and t are determined, the reflectance and transmittance can be easily calculated:

$$R = | r |^2, T = | t |^2 \cdots\cdots (16)$$

For multi stacked layers,

$$M = M_1 * M_2 * M_3 * \ldots * M_n \cdots\cdots (17)$$

where M_i is the transfer matrix for layer *i* as shown in **Figure 5.3**, and other calculations are still valid.

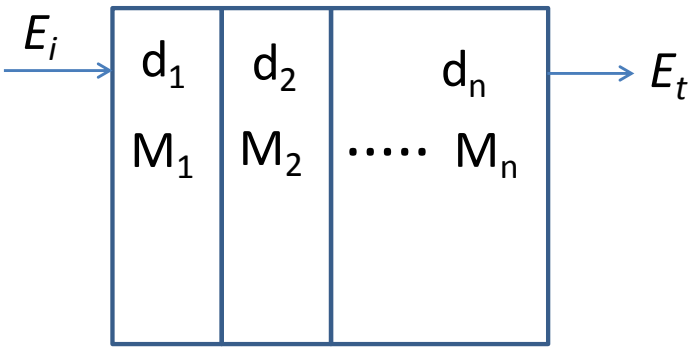

Figure 5.3 Transfer matrix in multi-layer structure.

Using equations (8), (12) and (15), the electric and magnetic field at any point can be computed, as well as the Poynting vector

$$S_i = \text{real}(E_i * conj(H_i))/2 \quad \cdots\cdots (18)$$

which represents the energy flux density. The *dS/dt (z)* is just the exciton generation rate, or energy dissipation rate as a function of the coordinate in the incident direction, and the normalization factor is the incident energy flux density:

$$S_{in} = 1/2 * E_0 * n_L * E_0 = 1/2\, n_L * E_0^2 \cdots\cdots (19)$$

The energy absorbed by the photoactive layer, where the photons can be turned to electrons, is determined by the difference of the Poynting vector at two boundaries of the layer. This value is less than *1-R-T* due to the absorption loss in other layers.

5.1.2 Dielectric function of photoactive layers in solar cell devices

The conventional device structure considered in this work, with ITO/ PEDT: PSSH as the hole collector, Ca/Al or Al as electron collector and the photoactive layer sandwiched in between is shown in **Figure 5.4**. The real *n* (λ) and imaginary *k* (λ) components of the refractive index spectrum of each layer were either obtained from variable angle spectroscopic

ellipsometry (VASE) or taken from literature. These are shown in **Figure 5.5** for the absorption spectral region of the photoactive layer. The n (λ) and k (λ) spectra of P3HT: PCBM with different weight/weight ratios 1:2, 1:1 and 2:1 were experimentally measured, and then interpolated using Bruggemann effective medium approximation to obtain its compositional dependence. The spectra were non-trivial because increasing the PCBM fraction does cause disordering and blue shift of the P3HT spectrum. $n_{PAL}(\lambda)$ lies between 1.5 and 2.2 over much of the absorption band, increasing towards the red edge of the spectrum and decreasing towards the blue part of the spectrum, as a result of the Karmers–Kronig relation. These features are common also to other organic polymer-based PALs, e.g. poly(4,4-dialkylcyclopenta[2,1-b;3,4-b']dithiophene-*alt*-benzothiadiazole), or PCPDTBT: PCBM (compare **Figure 5.6** (a) and (b)).[14,15]

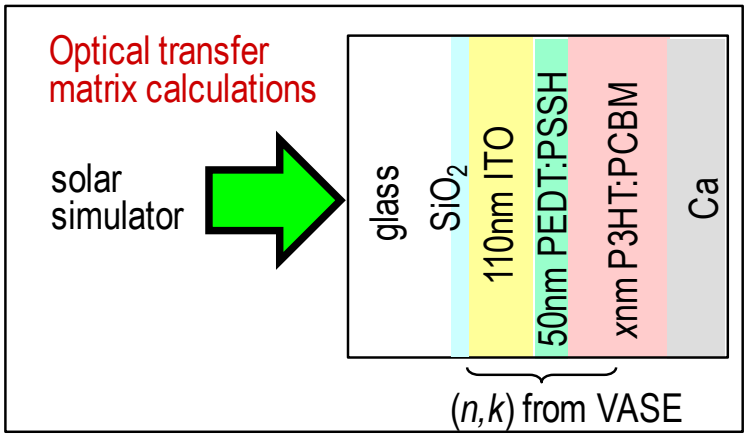

Figure 5.4 Optical model of P3HT: PCBM solar cells. The thickness and composition of the photoactive layer P3HT: PCBM are systematically varied to check for agreement between theory and experiment.

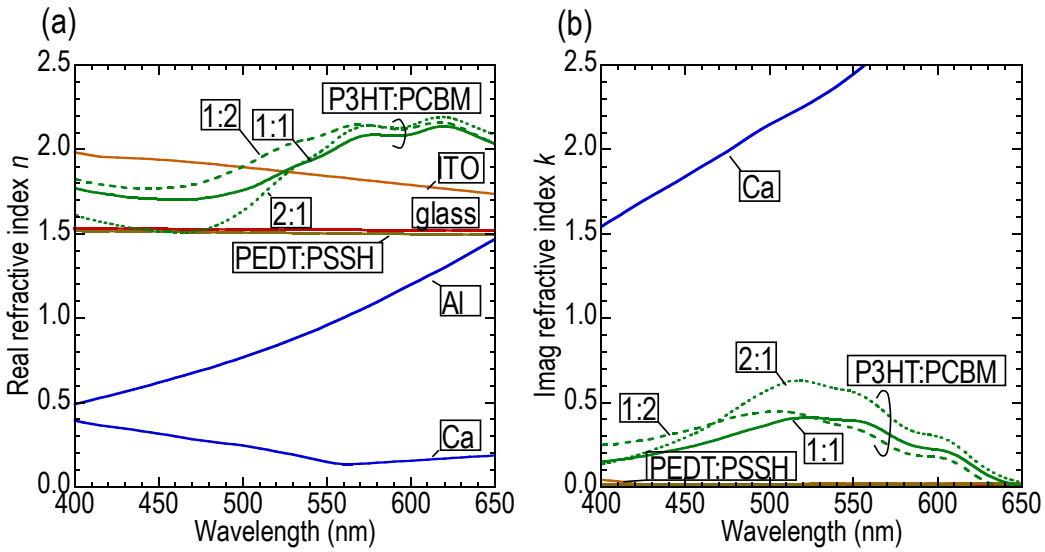

Figure 5.5 (a) Real *n* (λ) and (b) imaginary *k* (λ) refractive index spectra of selected layers over the absorption region of the photoactive layer. The *k* (λ) spectrum of Al lies above 2.5 in the plot.

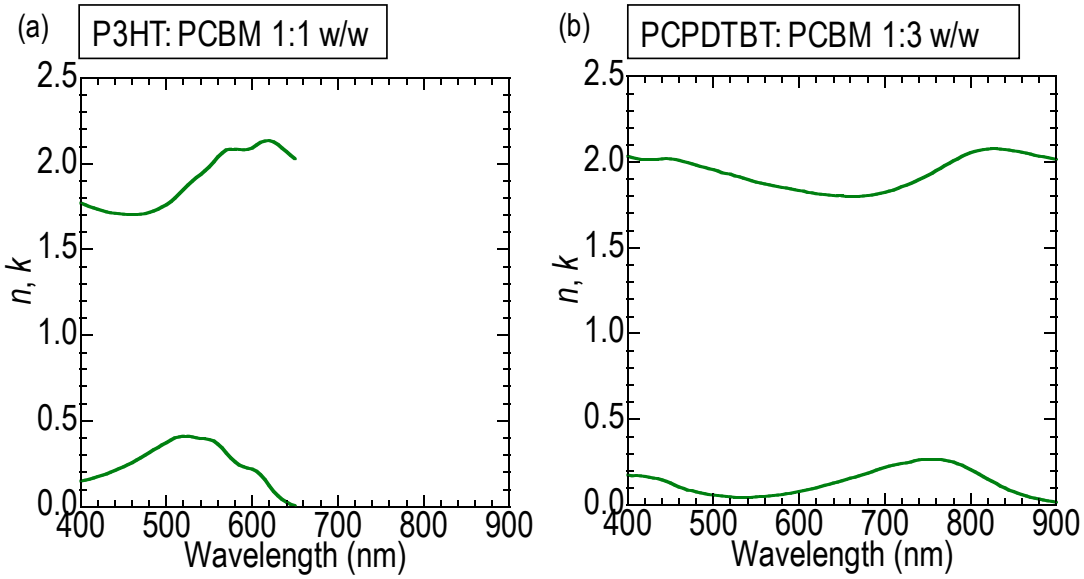

Figure 5.6 Real *n* (λ) and imaginary *k* (λ) refractive index spectra of (a). P3HT: PCBM and (b). PCPDTBT: PCBM system over the absorption region.

5.1.3 Effect of photoactive layer thickness on solar cell absorption

The n_{PAL} and k_{PAL} spectra of P3HT: PCBM (1:1 w/w) and PCPDTBT: PCBM (1:3 w/w) are shown for comparison in **Figure 5.6** (a) and (b) respectively. PCPDTBT is a prototype low bandgap donor polymer. As a consequence of the larger weight fraction of PCBM (and $PC_{71}BM$) present in the "optimized" PAL, the maximum k_{PAL} value at its primary absorption band is correspondingly lower than that of the P3HT: PCBM. Because of the lower absorption wavelength onset, the *n* spectrum is also downshifted as required for Kramers–Kronig consistency. Neverthess the mean refractive index over its absorption band (≈ 1.9) is not much different from that of P3HT: PCBM.

To study fraction of incident photons that is absorbed in these two representative PALs, we computed the rate of absorption of photons $\Phi_{ph}(z)$ in the PAL (cm^{-3} s^{-1}) as a function of distance *z* from the back reflector, from the Poynting vector difference per unit distance integrated over the incident $S(\lambda)$. This exciton generation profile multiplied by η_{gen}, assumed to be a heterostructure constant, gives the photocarrier generation profile *G*(z), since the heterostructure length scale (few nm) is considerably shorter than the optical length scale (few hundred nm):

$$G(z) = \Phi_{ph}(z) \cdot \eta_{gen} \ldots\ldots (20)$$

$\Phi_{ph}(z)$ is then integrated over the PAL thickness to give $\Phi_{ph} = \int_0^d \phi_{ph}(z)dz$. We define $\alpha = \frac{\Phi_{ph}}{\Phi_{ph,inc}}$, which is the fraction of incident photons absorbed in the PAL.

α is plotted as a function of wavelength for P3HT: PCBM and PCPDTBT: PCBM in **Figure 5.7** (a) and (b) respectively, for different *d*, to reveal the optical absorption characteristics of these

cells. The $\alpha(\lambda_o)$ characteristic of P3HT: PCBM, which absorbs over 400–650 nm, increases to a first maximum at d = 70 nm, then decreases and increases to a second higher maximum at d = 200 nm, in an oscillatory behavior. The second absorption maximum has a wider flat top than the first, and so photons at the wings of the absorption band are also effectively absorbed. In contrast, the $\alpha(\lambda_o)$ of PCPDTBT: PCBM, which has a longer-wavelength primary absorption band over 600–900 nm, shows a similar oscillatory behavior stretched out to much larger d, with the absorption thickness maxima at 100 and 280 nm. This increase in d is simply related to the absorption center wavelength and n_{PAL} as a result of optical interference (see Section 5.4).

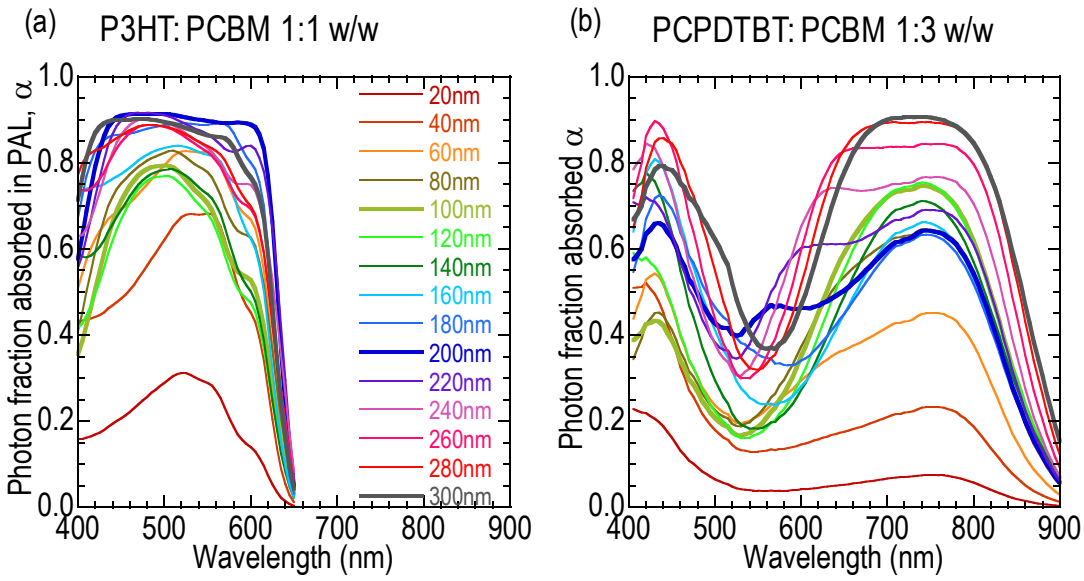

Figure 5.7 Wavelength dependent absorption fraction of (a). P3HT: PCBM and (b). PCPDTBT: PCBM at certain photoactive layer thicknesses.

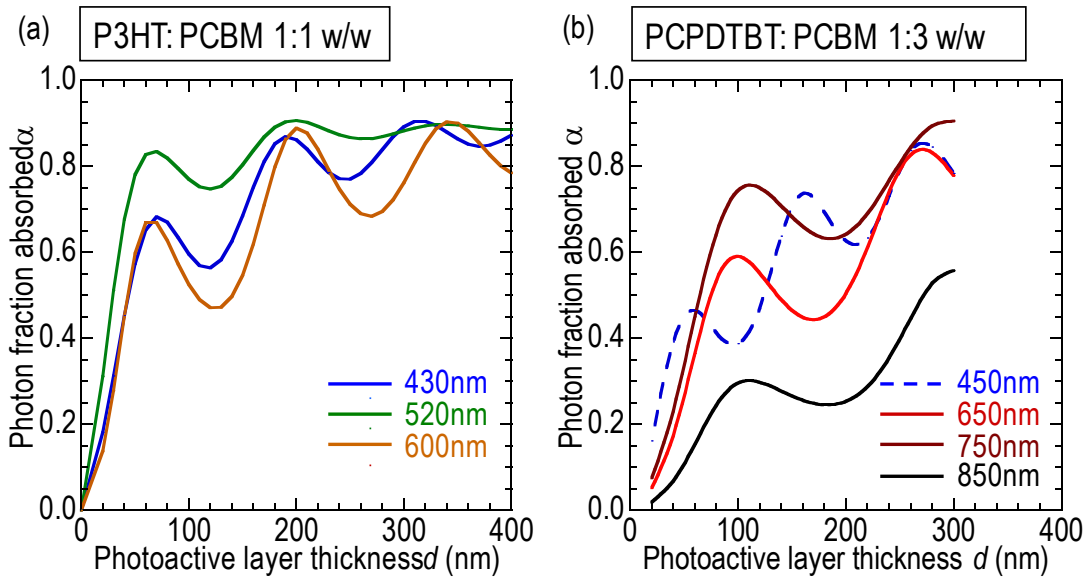

Figure 5.8 Thickness dependent absorption fraction of (a). P3HT: PCBM and (b). PCPDTBT: PCBM at certain wavelengths. Absorption oscillates as a function of photoactive layer thickness. In P3HT: PCBM, the first optimum thickness is around 70nm, and second optimum is at 200nm. In PCPDTBT: PCBM, the first optimum thickness is around 100nm, and second optimum is at 280nm.

5.1.4 Absorption thickness optima

An interesting feature of the oscillatory behavior is revealed when α is plotted as a function of d, as shown in **Figure 5.8**(a) and (b), for wavelengths selected across the absorption band. The absorption thickness optima for different wavelengths within the same absorption band are surprisingly only weakly dependent on λ_o. For example, the shift in the first absorption maximum is less than 20 nm over a wavelength range of 200 nm. This is the consequence of an accidental self-compensation between the increase in λ_o and n_{PAL} across the absorption band, which causes the optical phase difference to change only little over the wavelength range. Thus the absorption thickness maxima d_{optm} (where m is an index), which give the PAL thicknesses that correspond to the spectral-weighted local absorption maxima, are in fact not

so sensitive to the exact wavelength within the absorption band. Therefore, they can be reliably estimated as those of the absorption center wavelength. For P3HT: PCBM, d_{optm} = 70, 200 and 330 nm for m = 1, 2 and 3 respectively, whereas for PCPDTBT: PCBM, d_{optm} = 110 and 290 nm for m = 1 and 2 respectively. For a different absorption band, e.g. the higher-lying absorption at 430 nm for PCPDTBT: PCBM, however, d_{optm} can be rather different. This result allows a robust general relationship to be found for d_{optm} (Section 5.4).

Another notable feature is that the ratio α at the first optimum to the second is disproportionately larger than the ratio of d_{opt1} to d_{opt2}, which is ≈ 0.33. As a result, it is possible to absorb a large fraction of the incident photons in very thin cells. This is due to optical-field enhancement within thin PALs in the presence of the back reflector. In any case, the maximum α does not exceed *ca.* 0.9, due to reflection losses at the air–glass interface, and competing absorptions in the ITO, PEDT: PSSH and metal electrode. However d_{opt1} and d_{opt2} are separated by a relative deep valley. Hence it is important to match PAL thickness to either of these optima to achieve high α (and high Φ_{ph}) which is a prerequisite for high *PCE*. The oscillations greatly damp out beyond d_{opt2}. However the large thickness of the PAL then causes a severely asymmetric photocarrier generation profile that places huge demands on transport that may make this regime generally unusable (Section 5.3).

5.1.5 Effect of PAL composition on absorption

Thin PALs in the vicinity of d_{opt1} do show a usually strong sensitivity of α to the exact film composition. This does not appear to have been appreciated previously. To illustrate the effect for P3HT: PCBM, we show a contour plot of the computed power absorbed in the PAL

as a function of (d_{P3HT}, d_{PCBM}) in **Figure 5.9**, for AM1.5 spectral distribution at 1.2 sun (120 mW cm^{-2}). [The reason for 1.2 sun is historical, and is of no significance since output power is linear and *PCE* is normalized.] The composition of the film is represented by (d_{P3HT}, d_{PCBM}), which gives the effective thicknesses of P3HT and PCBM (cm^3 cm^{-2}). The ratio d_{P3HT} /d_{PCBM} thus gives the composition ratio, while d_{P3HT} + d_{PCBM} gives the total thickness d.

Two features can be noted. As the PAL thickness increases at a constant composition ratio, i.e., along diagonals radiating from the (0, 0) origin, there is a strong oscillation in the absorbed power with the thickness. This can be seen in the projection of the contour plot along constant composition-ratio lines. For example, along the P3HT: PCBM 1:1 w/w line, the first and second absorption maxima reaches 33 mW cm^{-2} at (45 nm, 25 nm) and 38 mW cm^{-2} at (130 nm, 75 nm) respectively.

However the first and second absorption composition peaks are not oriented in the same way. While the second (and higher) peak is as broad and spans a wide composition range that is equally effective in absorbing the solar spectrum, the first maximum is contracted in the d_{PCBM} direction but elongated along the d_{P3HT} direction. The reason for this is because absorption in thin PALs increases strongly with k_{PAL}. Hence the peak is disposed towards the 2:1 P3HT-rich composition line, since P3HT is by far the stronger absorbing component. As a consequence, the absorption at d_{opt1} though not the thickness itself depends strongly on composition.

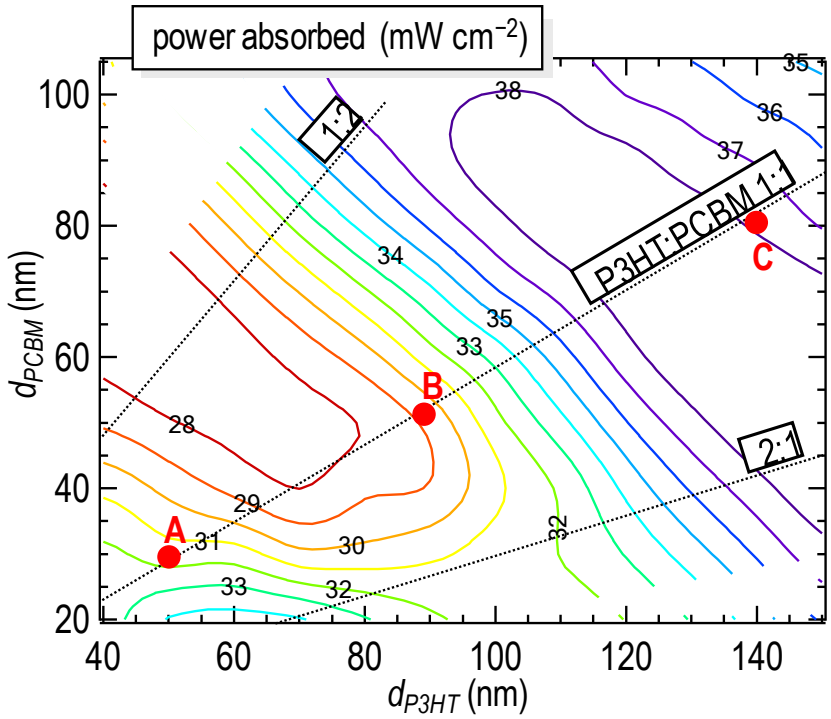

Figure 5.9 Computed composition dependence of power absorbed (contour lines) for 1.2-sun equivalent illumination with relative spectral intensity that same as in AM1.5, showing oscillation of the solar cell absorbance in composition phase space.

5.1.6 Optical-field intensity pattern

To explain why thin PALs at the first absorption thickness maximum can provide strong absorption, we plot the fractional photon absorbed per unit distance across the PAL in **Figure 5.10**, and for different *d* values that correspond to A, B and C along the 1:1 composition line in **Figure 5.10**, near the first maximum, valley, and second maximum respectively. We plot the results for different wavelengths across the primary absorption band, which is proportional to the average optical-field intensity. We also show the AM1.5-integrated exciton generation profile.

The plots show that d_{opt1} and d_{opt2} correspond to the emergence of one and two optical-field antinode in the PAL respectively. In the thicker PAL, the stronger antinode resides in the front half of the PAL as expected, and the weaker one in the back half. "Front" here refers to the face that is illuminated by light. The reason why a PAL at d_{opt1} can absorb so strongly is because of the enhanced optical field caused by reflection by the back reflector. In other words, photons traveling through thin PALs get a second pass through the PAL. This enhancement becomes weakened at d_{opt2} because of much greater absorption in the first pass. The absorption valley between d_{opt1} and d_{opt1} is due to entry of an optical-field node at the front face, which suppresses absorption there. Thus reducing the back reflectivity, e.g. to achieve semi-transparent solar cells, will cause the absorption at d_{opt1} to fall markedly, and suppress the oscillations.

Secondly, it is clear there is an asymmetry in the exciton generation profile at d_{opt2} (and also higher d_{optm}). While the optical-field intensity pattern for d_{opt1} is *nearly* symmetric about the antinode plane, the pattern for d_{opt2} is strongly weighted to the front of the PAL. This results in an asymmetric $G(z)$, which dominates transport optimization (Section V) and appears to also not have previously been appreciated.

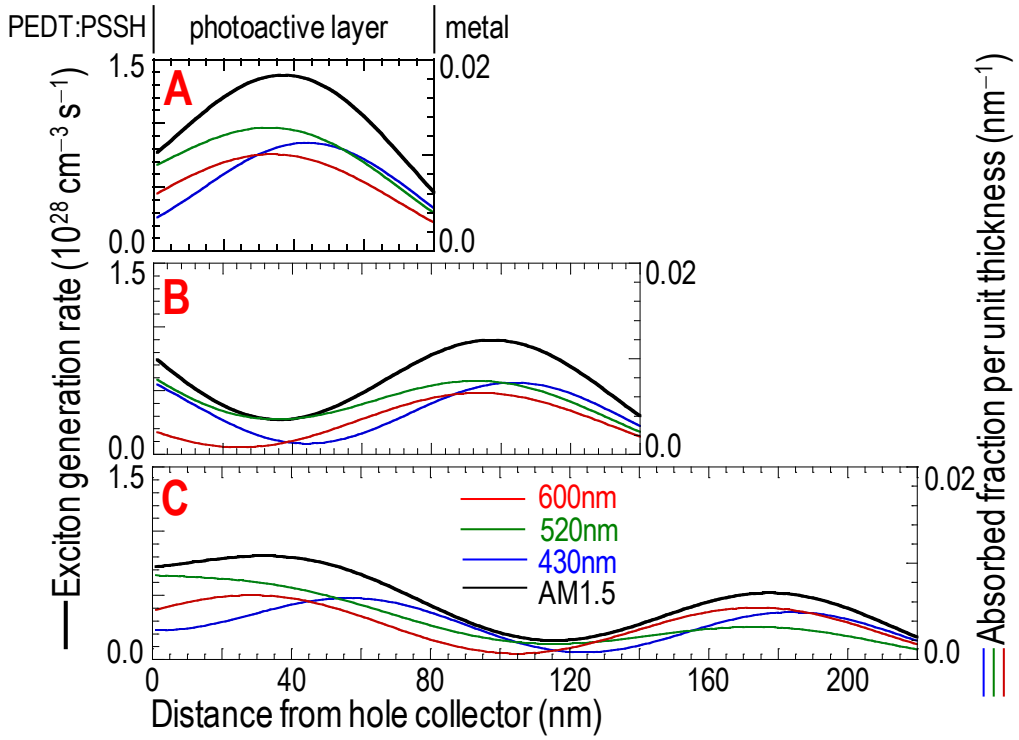

Figure 5.10 The exciton generation profile in the P3HT: PCBM solar cells. **(Left axis)** Computed exciton generation profile under at 1.2-sun equivalent illumination (120 mW cm^{-2}) of the AM1.5 spectrum. **(Right axis)** Computed incident photon absorped fraction per unit distance $(1/I_o)(dI/dz)$ at 600, 520 or 430-nm wavelengths for the photoactive layers indicated A, B and C in **Figure 5.9**.

5.1.7 Experimental validation

We have previously noted that the *PCE* landscape of the crosslinked P3HT network: PCBM solar cells with consistent morphology contains clear signatures of the absorption landscape, which provides unambiguous evidence for composition- and thickness-dependent optical interference effects in these cells.[2] Using this set of devices, we show here that quantitative agreement has also been reached between model predictions and the measured device J_{sc} as a function of d. **Figure 5.11** plots the measured J_{sc} for a set of network cells (red closed symbols) along the 1:1 P3HT: PCBM line, together with the computed ideal J_{id} assuming unity

η_{int} (dotted line). The J_{sc} of these network cells closely track J_{id} with a constant factor of 0.9, which gives the η_{int} of these cells. In contrast, the J_{sc} of the usual demixed biblend cells (blue open symbols) along the same line shows an initial η_{int} = 0.8, but gradually fall away to η_{int} = 0.65, due presumably to the strong evolution of morphology with PAL thickness in these demixed biblend films.[2] The quantitative agreement between theory and experiment for the crosslinked P3HT network: PCBM cells provides a satisfying validation of the optical model, even if there is no a priori reason why it should fail.

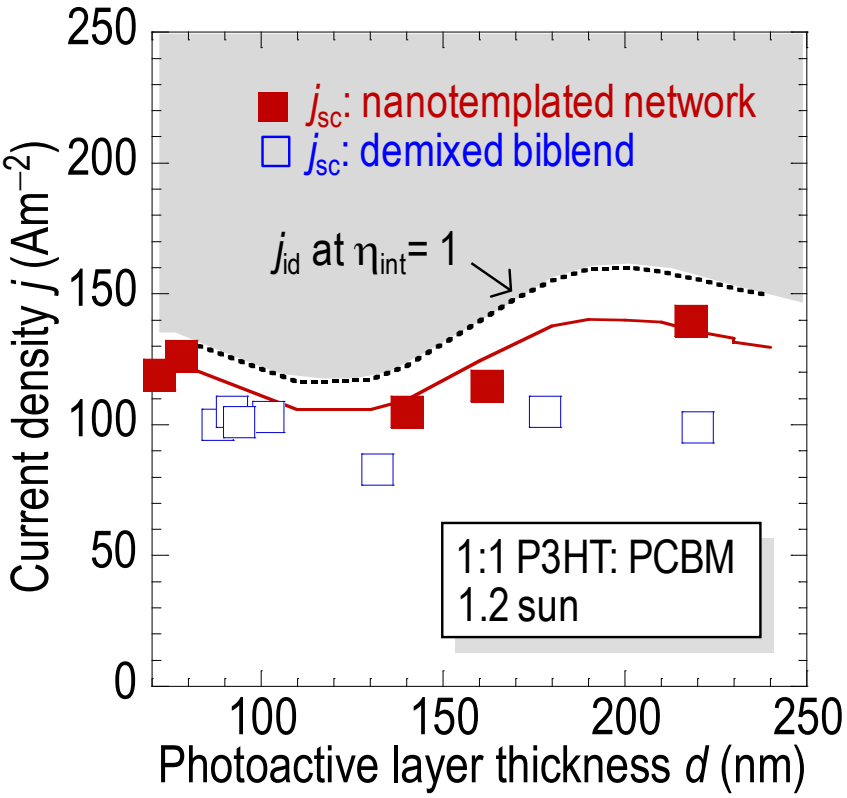

Figure 5.11 Quantitative test of the optical-structure effect. Plot of experimental J_{sc} and predicted ideal J_{id} against PAL thickness. Symbols, experimental data; dotted black line, optical model prediction; solid red line, model prediction with a constant scale factor of 0.90. The consistent tracking between the measured J_{sc} and the ideal J_{id} for the crosslinked P3HT network: PCBM solar cells wprovides critical validation of the optical model.

5.2 Electrical model, parameterization and validation

To model the current density–voltage (*J*-*V*) characteristics of the cells, we adopted the standard diffusion–drift model with bulk carrier generation and recombination.[3-5] We used *G(z)* as input to the photocarrier generation rate, and determined the response of the electron *n*(*z*) and hole *p*(*z*) densities under diffusion, drift and recombination.

5.2.1 Description of the drift-diffusion model

The optical model delivers the input *G*(*z*) profile for the cell. We then determined the steady-state electron *n*(*z*) and hole *p*(*z*) densities that emerge self-consistently under the action of diffusion, drift and recombination. To model the *JV* characteristic, we adopted the standard diffusion–drift model[3-5] assuming photocarrier generation and recombination characteristics that were guided by experiments.

The Poisson equation is given by:

$$\frac{\partial^2 \Psi(\mathrm{z})}{\partial \mathrm{z}^2} = \frac{\mathrm{q}}{\varepsilon}[\mathrm{n}(\mathrm{z}) - \mathrm{p}(\mathrm{z})] \cdots\cdots (21)$$

where $\Psi(\mathrm{z})$ is the electric potential, *q* is the elementary charge (1.602x10^{-19} C) and ε is the dielectric constant, taken to be 3.0 for P3HT: PCBM system. *p*(*z*) and *n*(*z*) are the hole and electron densities respectively.

The drift–diffusion currents are given by:

$$\begin{cases} \mathrm{J_p} = -\mathrm{qp}\mu_\mathrm{h}\dfrac{\partial \Psi}{\partial \mathrm{z}} - \mathrm{qD_p}\dfrac{\partial \mathrm{p}}{\partial \mathrm{z}} \\ \mathrm{J_n} = -\mathrm{qn}\mu_\mathrm{e}\dfrac{\partial \Psi}{\partial \mathrm{z}} + \mathrm{qD_n}\dfrac{\partial \mathrm{n}}{\partial \mathrm{z}} \end{cases} \cdots\cdots (22)$$

where D_p and D_n are the hole and electron carrier diffusion coefficients, assumed to obey the Einstein relation:

$$\begin{cases} D_p = \mu_h V_T \\ D_n = \mu_e V_T \end{cases} \cdots\cdots (23)$$

with V_T the thermal voltage $V_T = k_B T / q$, where k_B is Boltzmann's constant and T is the absolute temperature. The assumption of non-dispersive transport is justified by high steady-state carrier density (>10^{16} cm^{-3}) and the more or less constant electric field across the bulk of the PAL. The μ_h and μ_e are known from independent measurements to be (1 ± 0.5) x 10^{-3} and (1 ± 0.5) x 10^{-4} $cm^2 V^{-1} s^{-1}$ respectively.[4,5] μ_e is expected to be reliable, since it is determined by electron hopping between PCBM molecules that are in van der Waals contact in an amorphous state. μ_h however may be variable, as it depends on molecular order of the P3HT chain segments. We find 2 x 10^{-4} $cm^2 V^{-1} s^{-1}$ describes the data well, and allow it to vary slightly to fit the *JV* characteristics.

5.2.2 Built-in potential

The electrostatic potential difference across the photoactive layer is determined by the applied voltage at the *h* collection contact V_a at location $z = d$, together with the built-in potential V_{bi}:

$$\Psi(d) - \Psi(0) = -V_{bi} + V_a \cdots\cdots (24)$$

Although this has sometimes been cast in terms of an energy gap, we find that V_{bi} provides a more precise concept. Assuming that the diffuse tail of the δ-doped layer[16] at each the contacts does not contribute to a significant potential drop, the V_{bi} drops between the two interface planes on the OSC side at $z = 0$ and $z = d$. This V_{bi} arises from the use of dissimilar *e* and *h* collectors in the PV cell, which causes an internal electric field to exist even at zero bias. The required applied potential to cancel this field to attain the flatband condition in the bulk of the PAL is the V_{bi}. This corresponds to the difference in effective work functions between the

two contacts,[17] and can be directly measured by electromodulated absorption spectroscopy.[16,18-21] Thus it is a key device parameter that together with V_a determines the electric field inside the cell. Nevertheless due to previous experimental difficulties, the value of V_{bi} even for P3HT: PCBM has only been estimated from *JV* or other indirect methods to be between 0.6 and 1.2 V.

To pin down this important parameter, we used a systematic electromodulated absorption (EA) spectroscopy study to find out the V_{bi} is 0.75 V (see Chapter 4).

5.2.3 Photo-carrier generation efficiency

The current divergence equations are given by:

$$\begin{cases} \frac{\partial \mathrm{J_p(z)}}{\partial \mathrm{z}} = \mathrm{qU(z)} \\ \frac{\partial \mathrm{J_n(z)}}{\partial \mathrm{z}} = -\mathrm{qU(z)} \end{cases} \cdots\cdots (25)$$

where $J_n(z)$ ($J_p(z)$) is the electron (hole) current density, and $U(z)$ is the net photocarrier generation rate given by $G(z) - R(z)$, where $R(z)$ is the depth-dependent carrier recombination rate ($cm^{-3}\ s^{-1}$).

$$\mathrm{G(z)} = \eta_{gen}\ \Phi_{\mathrm{ph}}(\mathrm{z}) \cdots\cdots (26)$$

where η_{gen} is assumed to be given by $\eta_{gen} = p \cdot \gamma_{CT}$, where γ_{CT} is the formation probability of the charge-transfer state and P is its dissociation probability according to the Braun–Onsager model.[22] Although this assumption does not appear to have been validated for P3HT: PCBM, we use it here, following Blom and co-workers,[3,4] as an expedient to mimic experimentally results. To reproduce the large P and its weak field dependence as suggested by transient

absorption spectroscopy,[23,24] and likely consequence of carrier delocalization in both PCBM and P3HT phases,[25] we took k_{rec} to be 10^5 s^{-1} and *e*–*h* distance in the CT state to be 2.8 nm. This gives $p \approx 0.85$ at 0.01 MV cm^{-1}, increasing to 0.92 at 0.1 MV cm^{-1}, as shown in **Figure 5.12**. Since the field dependence is weak, the error in assuming a particular form is not of any consequence.

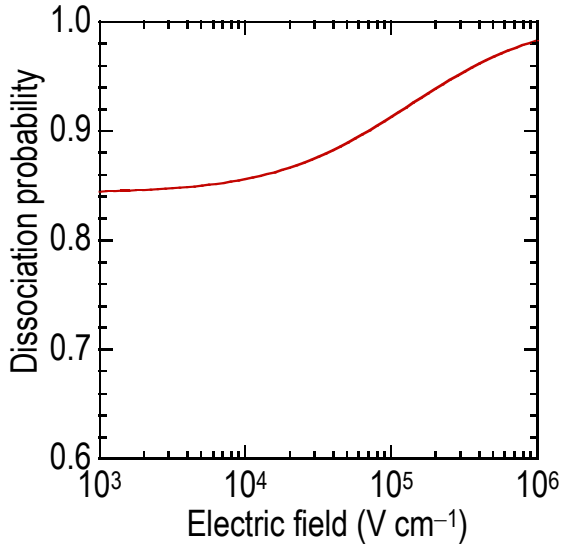

Figure 5.12 Plot of the CT-state dissociation probability vs electric field. Generated from the Braun−Onsager model with k_{rec} of 10^5 s^{-1}, and *e*–*h* distance in the CT of 2.8 nm, to mimic transient absorption spectroscopy results from Ref[26].[26] To indicate the range of uncertainty in these parameters: k_{rec} = 1 x 10^4 s^{-1} and *a* = 2.2 nm also gives a similar plot.

5.2.4 Non-geminate photocarrier recombination

The carrier recombination rate is given by:

$$R(z) = k_{bi} n(z) p(z) \cdots\cdots (27)$$

where k_{bi} is the bimolecular recombination coefficient. Recent work suggests this has a carrier-density dependence,[27] which we assume is true over the range of steady-state carrier densities present in the cell, and is built on a Langevin-like expression:

$$k_{bi} = \xi(1-P)\frac{\sqrt{n(z)p(z)}}{n_o}\frac{q<\mu_e+\mu_h>}{\varepsilon} \quad \cdots\cdots (28)$$

Here the carrier-density dependence is imposed *ad hoc* as the geometric mean of $n(z)$ and $p(z)$, with n_o as a normalization factor for the $[n(z)p(z)]^{1/2}$ term, taken to be 3.3 x 10^{16} cm^{-3}, a typical mean density in the cell. The k_{bi} is then modified by a proportionality factor ξ, taken to be a fitting parameter.

5.2.5 Boundary conditions

Recent device spectroscopy measurements confirm the presence of a δ-doped carrier layer at the OSC interface of ohmic contacts.[16] This layer has a density that is often only weakly bias-dependent. We thus imposed at the *e and h* collection contact respectively:

$$\begin{cases} n(0) = N_e \\ p(d) = N_h \end{cases} \quad \cdots\cdots (29)$$

However no independent determination of N_e and N_h is presently available. Nevertheless the vacuum-level offset at the PEDT: PSSH/ P3HT contact (1.0 V)[28] is similar to that expected at the PCBM/ Ca contact (for Ca effective work function of 2.4 eV;[17] and PCBM P^- level of 3.5 eV). Therefore the double-layer charge densities at both these interfaces can be expected to be similar. Hence for simplicity we may assume $N_e \approx N_h = N$, which we take to be another fitting parameter.

We have also considered the use of non-injecting contacts to simulate the situation where the δ-doped layer is absent. In this case:

$$\begin{cases} n(z=0) = n(z=\zeta) \\ p(z=d) = p(z=d-\zeta) \end{cases} \quad \cdots\cdots (30)$$

where ζ is a simulation distance step.

The Poisson and current continuity equations were then solved iteratively and self-consistently following Grummel and co-workers.[29,30] The correctness of the solutions was confirmed by visual inspection for self-consistency of the simulated characteristics: $G(z)$, $R(z)$, $n(z)$, $p(z)$, $J_n(z)$, $J_p(z)$ and $\phi(z)$, for example, as shown in **Figure 5.15**.

5.2.6 Evaluation of N and ξ

The two key parameters that need to be fitted are thus N and ξ. N governs the forward injection current in the vicinity of V_{bi}, when the space-charge limit (SCL) is not yet reached. To evaluate N, we fitted the JV curve over the voltage range $0 \leq V_a \leq 0.9$ V, as shown in **Figure 5.13**. We found that $N \approx 5\pm1 \times 10^{17}$ cm^{-3} provides a good fit to both the dark and illuminated JV characteristics. The prior determination of V_{bi} removes parameter coupling and allows N to be determined with confidence.

The N value is much larger than the steady-state carrier densities in the cell under solar irradiance (≈ 0.1–1 x 10^{16} cm^{-3}; Section V) and thus appears to be a robust boundary condition that is determined by the nature of the ohmic contacts. It corresponds to an equivalent monolayer charge density of *ca*. 1 x 10^{11} cm^{-2} when integrated over a 1.6-nm-thick layer. This is only ≈ 2% of the double-layer charge density of ≈ 5 x 10^{12} cm^{-2} that is required to provide the 1.0-eV vacuum-level offset at each of the two contacts.[16] This suggests that only a small

fraction of the carriers, at the % level, in the δ-doped layer is mobile and can contribute to the injection current. The δ-carrier density comprises a small mobile fraction and a large immobile fraction. This suggests that the carriers at the interface reside in a broad energy distribution, extending perhaps over several k_BT, due to coulomb or other disorder, and so only a small fraction can be injected into the bulk of the OSC.

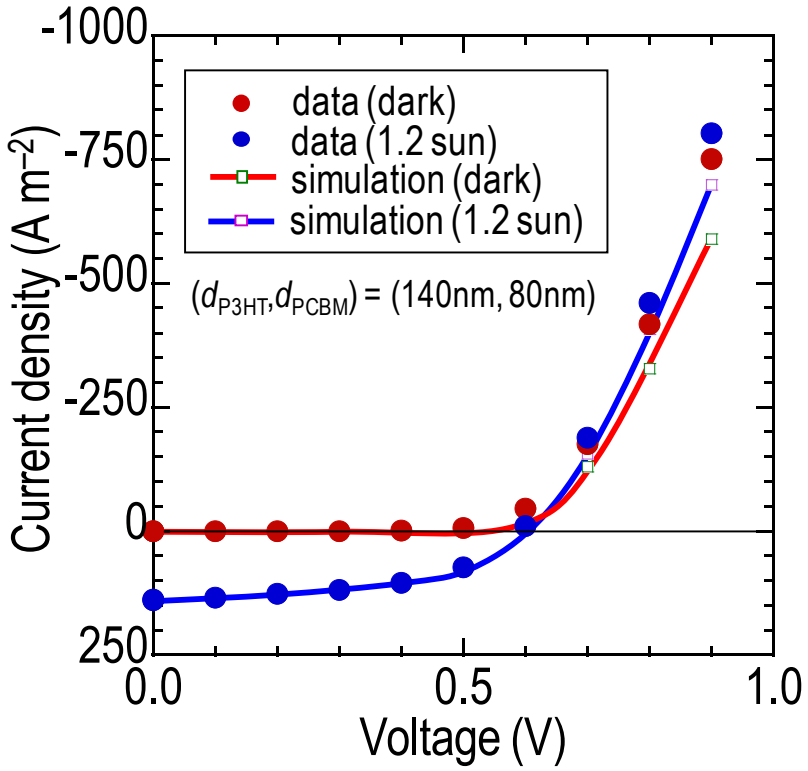

Figure 5.13 Evaluation of interface mobile carrier density. Experimental (symbols) and simulated (lines) *JV* characteristics for crosslinked P3HT: PCBM solar cells, collected in the dark and under 1.2-sun irradiance. The fitting allows N (assumed to be equal to N_e and N_h) to be unambiguously obtained given V_{bi} has been separately determined by experiment.

To determine ξ, we fitted the *JV* characteristics for several d values over the voltage range −1 V ≤ V_a ≤ 0.6 V, with ξ as a global fitting parameter defined by Eq(28), and found ξ ≈ 0.1. This

procedure is not able to test the validity of the functional form of Eq(28). Nevertheless we can determine that the k_{bi} at the typical carrier density in the device (10^{16} cm^{-3}) is ≈ 2 x 10^{-12} cm^{-3} s^{-1}. For comparison, the Langevin recombination rate constant k_L given by $k_L = (1-p)\frac{q<\mu>}{\varepsilon}$, where <μ> is the effective carrier mobility ≈ $\sqrt{\mu_e^2 + \mu_h^2}$ (sometimes erroneously assumed to be the lower mobility) and p is the dissociation probability of the CT state formed by *e*–*h* capture, is 6 x 10^{-10} cm^{-3} s^{-1}. Thus k_{bi} is 2–3 orders of magnitude smaller than k_L, as suggested already by other authors.[3,4,27,31] This conclusion here is robust in the framework of the model.

The large reduction in the recombination constant has been suggested to have a geometric origin due to separate confinement of *e* and *h* transport paths.[27,31] We propose here a simple scaling argument for the magnitude of this effect. In a two-phase system where *e* and *h* are confined to separate percolating phases, only carriers that that encounter in contacting phases can recombine. Carriers that fall into their mutual coulomb trap but are separated by intervening phases cannot recombine and must eventually escape their mutual coulomb attraction. If the phases have width ℓ that is small compared to the coulomb capture radius r_C, the probability for carriers within the coulomb radius to also be in adjacent phases scales with $(\ell / r_C)^2$, based on their cross-sectional area ratio. Hence for ℓ of a few nm as typical in these cells,[2] and r_C ≈ 20 nm, the k_{bi} can be lowered by 2 orders of magnitude, in concordance with the fitted result.

5.2.7 Experimental validation of the optical–electrical model

We found the model with the "global" parameters described above can accurately predict the *JV* characteristics of the crosslinked P3HT network: PCBM cells as shown in **Figure 5.14**. This is remarkable because excellent match between theory and experiment occurs over an unprecedentedly wide range of PAL thicknesses that span the first two d_{optm}. It shows the devices are indeed well-behaved. It also provides a stringent validation of the device model and its parameters.

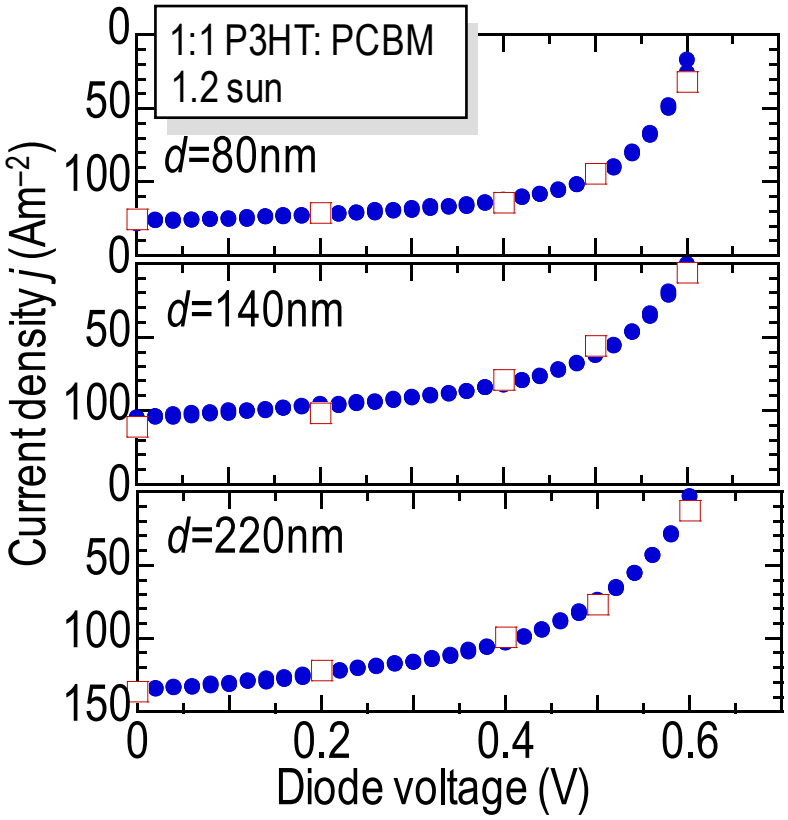

Figure 5.14 Quantitative test of the optical−electrical device model. Solid symbols, experimental data for crosslinked P3HT: PCBM solar cells with 1:1 w/w ratio; open symbols, model prediction. The excellent agreement achieved for a "global" set of parameters across a wide PAL thickness range confirms the validity of the model and the quality of its parameters.

5.3 Transport optimization of organic solar cells

With this calibrated model, we can begin to systematically survey the optimization landscape. This space is very large because of the number of degrees of freedom. To be tractable, we have confined the study to the following parameters: μ_e and μ_h, d, and $\tilde{n}_{PAL}$; while keeping the others (V_{bi}, k_{bi}, N, and P) fixed at the values found in P3HT: PCBM cells. We have fixed V_{bi} = 0.75 V because this is fairly typical of organic solar cells, and its impact on cell performance is relatively easy to understand (both V_{oc} and FF fall with decreasing V_{bi}). We have fixed k_{bi} and P because they are likely also to be characteristic of efficient materials systems. We have fixed N because this arises from ohmic contacts, but will briefly discuss what happens when this constraint is relaxed. We have also fixed the absorption spectrum of the PAL to be that of the 1:1 w/w P3HT: PCBM. Hence we focused here only on the optimization of transport and optical-structure factors, assuming that the others are separately optimized, and the transport and optical-structure effects are not coupled.

5.3.1 Second absorption maximum

For an organic solar cell with back reflector, d_{opt1} occurs at ≈ 70–120 nm. This small thickness together with the strong composition sensitivity may make d_{opt1} challenging to manufacture consistently and defect-free over large areas. Hence we focus on the transport optimization landscape in the vicinity of d_{opt2}, although we will briefly discuss the situation at d_{opt1}. At the d_{opt2} thickness, the photocarrier generation profile is significantly asymmetric with a stronger optical-field antinode in the front and a weaker one at the back of the PAL, causing the average transport distances for e and h to their collection contacts to differ. We denote here the carrier that has on average to travel a longer distance to its collector the “distal” carrier, and

the other one the "proximal" carrier. This results in a pronounced non-monotonic dependence of *JV* characteristics on mobility ratio.

In the following, we illuminate through the *h* contact (i.e., normal cell configuration), and so *h* is the proximal carrier while *e* is the distal carrier. These labels will obviously switch if the cell is illuminated through the *e* contact (i.e., inverted configuration[32]). The computed photocarrier generation profile $G(z)$ and the net photocarrier generation profile $U(z)$ plotted against distance z from the back reflector, are shown for five cases of μ_e and μ_h in the top row panels of **Figure 5.15**. The μ range is from 10^{-2} to 10^{-4} cm^2 V^{-1} s^{-1}, which covers the accessible useful range in PV OSCs. The plots are constructed for V_a = 0 V (i.e., at short circuit) for the normal cell configuration with d = 220 nm. The crosslinked P3HT network: PCBM cells correspond approximately in-between the second and third columns with (μ_e, μ_h) = (1 x 10^{-3}, 2 x 10^{-4}) (μ in units of cm^2 V^{-1} s^{-1}). The next two rows show the computed $n(z)$ and $p(z)$, and their associated $J_n(z)$ and $J_p(z)$. The bottom row shows the computed $\phi(z)$. The difference ϕ(220nm) – ϕ(0nm) is fixed at 0.75 V, corresponding to the assumed V_{bi} of the cells. The computed *JV* characteristics in the power generation quadrant are shown in **Figure 5.16**, while the computed *FF* and *PCE* values are shown in a matrix in **Table 5.1**.

(a) Power conversion efficiency (%)

1x10^{-2}	2.0	4.6	5.9
1x10^{-3}	2.3	5.2	5.4
1x10^{-4}	2.9	3.3	3.0
μ_h / μ_e	1x10^{-4}	1x10^{-3}	1x10^{-2}

(b) Fill factor

1x10^{-2}	0.43	0.66	0.86
1x10^{-3}	0.42	0.73	0.74
1x10^{-4}	0.44	0.49	0.49
μ_h / μ_e	1x10^{-4}	1x10^{-3}	1x10^{-2}

Table 5.1. (a) *PCE* and (b) *FF* computed for P3HT: PCBM solar cells with different electron and hole mobility combinations. Conditions are as given in **Figure 5.15**. Carrier mobilities are given in units of cm^2 V^{-1} s^{-1}.

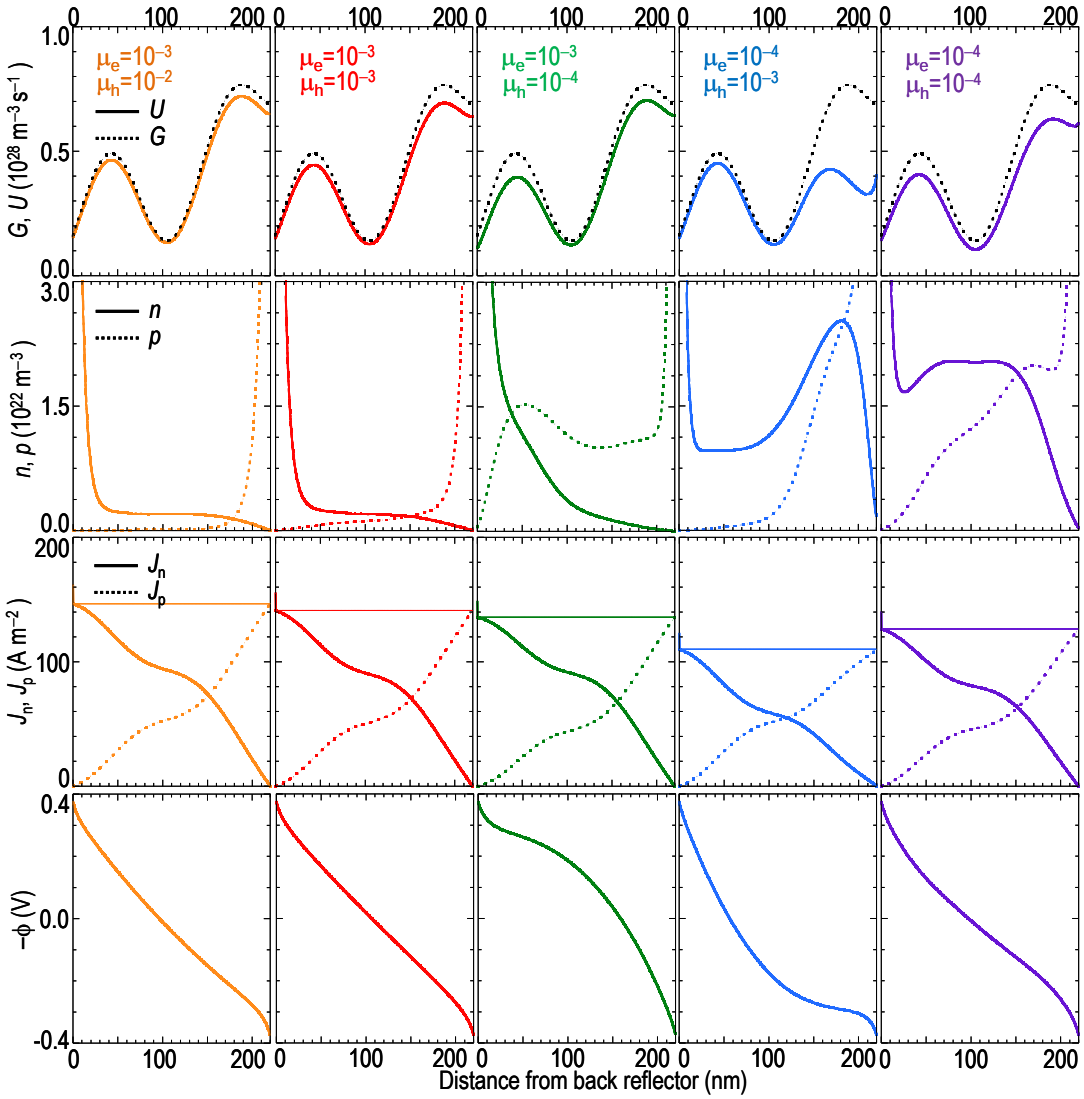

Figure 5.15 Charge carrier mobility and non-uniform exciton generation profile effect in a 220nm P3HT: PCBM device, *Va* =0 V. Exciton/ net generation profile, electron and hole (*n,p*) density profile, electron and hole current density profile (*Jn, Jp*) and voltage profile at four typical electron/hole mobility combinations. Illumination equals to 1.2-sun.

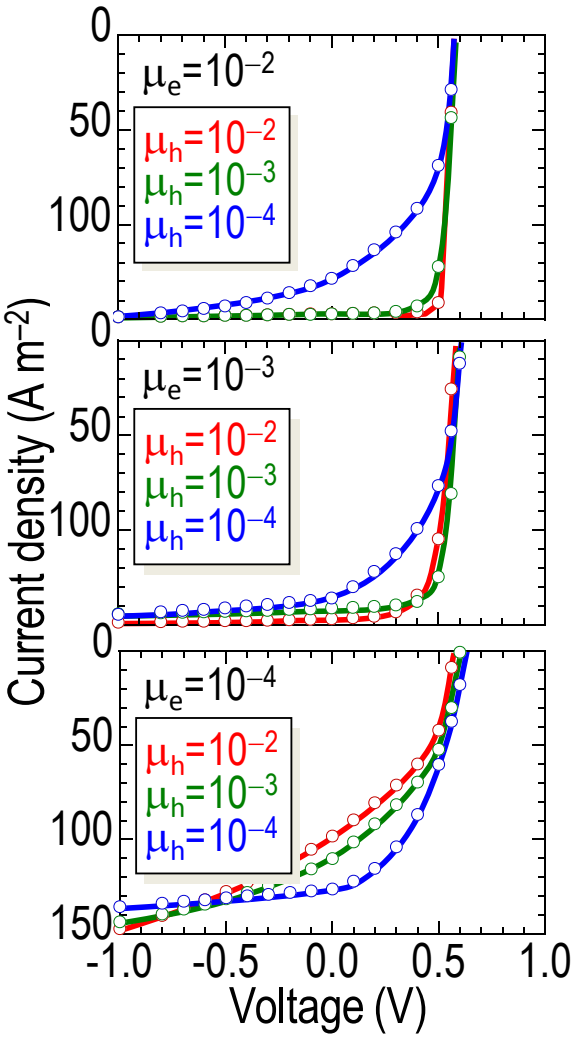

Figure 5.16 Modeled JV curves of 220 nm P3HT: PCBM solar cell with different mobility combinations.

5.3.2 Steady-state photogenerated carrier densities

Figure 5.15 shows a clear accumulation of *n* and *p* at the respective contacts, which correspond to the δ-doped layers.[16] These densities decay exponentially into the PAL over a distance of *ca*. 20 nm to reach the steady-state photogenerated bulk value. The combined voltage drop over the diffused tails of these δ-doped layers is only 0.05 V, and practically independent of μ. This justifies the assumption in Eq(24) that V_{bi} drops between the z = 0 and z = d planes.

If both μ_e and μ_h are large ($\geq 10^{-3}$ cm^2 V^{-1} s^{-1}), we find the steady-state bulk photogenerated carrier densities are small (n, $p \leq 2 \times 10^{15}$ cm^{-3}). The space-charge voltage (SCV) given by Eq(21) [explicitly, $\phi(z) = \iint \frac{q}{\varepsilon}[n(z) - p(z)]dzdz$] across the PAL is small, < 0.1 V, as indicated also by the small ϕ curvature. The $J_n(z)$ and $J_p(z)$ profiles indeed contain the signature of the two optical-field antinodes. Both the J_n and J_p profiles show a large step increase across the primary antinode and a smaller one across the secondary antinode.

When either or both of the carrier mobilities decrease, n and p will build up in the PAL. This has the following consequences: (i) $R(z)$ increases to a more sizeable fraction of $G(z)$, and so $U(z)$ falls further below $G(z)$. (ii) SCV increases, as indicated by a larger curvature in ϕ. Four qualitatively distinct cases can be distinguished, as exemplified by the following sets of (μ_e, μ_h): (10^{-3}, 10^{-3}), (10^{-4}, 10^{-4}), (10^{-4}, 10^{-3}) and (10^{-3}, 10^{-4}). We label these four cases (high, high), (low, low), (low, high) and (high, low), based on the relative magnitudes of their μ_e and μ_h. We can the understand the transport optimization landscape by considering the changes when transforming between these cases.

When we go from (high, high) to (low, low), the following occurs: (i) SCV increases, (ii) J_{sc} decreases, (iii) *FF* decreases, and (iv) *PCE* decreases. Basically all parameters of cell performance turn bad, as can also be seen by inspecting elements in the diagonal direction in **Table 5.1**. For example, if $\mu_e = \mu_h = \mu$ (i.e., matched mobilities), *FF* decreases from 0.86 to 0.44 when μ decreases from 10^{-2} to 10^{-4} cm^2 V^{-1} s^{-1}. This is the result of a large increase in n and p throughout the PAL. Hence a PAL with higher carrier mobilities for both signs generally outperforms one with lower mobilities.

5.3.3 Effect of mismatched mobilities

When we go from (low, low) to (high, low) or (low, high), the space-charge voltage increases. Having one carrier to be more mobile counter-intuitively causes the SCV to increase. This is because the mobility mismatch causes the neutral space-charge plane where $n(z) = p(z)$ to shift away from the PAL center toward the collector of the fast carrier, resulting in the growth of the space-charge width and density, as noted previously for the case of uniform $G(z)$.[5] For a realistic non-uniform $G(z)$, however, two qualitatively different outcomes are possible depending on whether the distal carrier is the fast or slow carrier.

If the distal carrier is the fast carrier, i.e., the (high, low) case here, we find a significant improvement in cell performance: J_{sc}, *FF*, and *PCE* are all higher than the (low, low) case. In marked contrast, where the distal carrier is the slow carrier, we find a marked degradation in cell performance: J_{sc}, *FF* and *PCE* are all lower than the (low, low) case, as can be seen in **Figure 5.16**, and on inspection of the off-diagonal elements in **Table 5.1**.

This leads to the apparent paradox that *reducing* the mobility of the proximal carrier to match that of the distal carrier improves cell performance. **Figure 5.15** shows that this improvement comes about because decreasing the sweep out of the proximal carrier suppresses the space-charge buildup particularly at the primary antinode, and the associated internal recombination losses. Further improvement can be achieved by increasing the mobility of the distal carrier to exceed that of the proximal carrier. There is an optimal ratio (here, $\mu_e / \mu_h \approx 10$) beyond which cell performance degrades again. For example, for a fixed $\mu_e = 10^{-3}$, both J_{sc} and *FF* increase as μ_h goes from 10^{-4} to 10^{-3}, but decrease as μ_h goes further to 10^{-2} (compare blue, green

and red curves in middle panel of **Figure 5.16**). However for fixed $\mu_h = 10^{-3}$, both J_{sc} and *FF* increase as μ_e increases over the same range (compared green curves across all panels). Finally, even better improvement can be achieved if both carrier mobilities are increased. For a 220-nm-thick PAL with similar optical and absorption characteristics as 1:1 w/w P3HT: PCBM, the simulation shows a *PCE* of ≈ 6% can be reached if $\mu \approx 10^{-2}$ cm^2 V^{-1} s^{-1}.

5.3.4 Optimal cell configuration

Hence the most desirable situation is not simply to achieved matched mobilities but to have them as large as possible (at least up till 10^{-2} cm^2 V^{-1} s^{-1}). If the carrier mobilities are mismatched, the optimal cell configuration is the one in which the slower carrier travels the shorter distance to its collector. For example, if $\mu_h << \mu_e$, as in P3HT: PCBM, the optimal cell configuration is the normal one, but if $\mu_e << \mu_h$, the optimal one is the "inverted" cell, from transport considerations alone. For cells operating at the first absorption thickness optimum, both configurations however are expected to work nearly equally well, because $G(z)$ is nearly symmetric (Section 5.1). Using a transparent conductive optical layer[33] to obtain one optical-field antinode within the PAL produces a similar situation.

5.3.5 Scope for contact engineering

Finally we examine the effect of boundary conditions on the *JV* characteristics of the solar cells. The *JV* characteristics for matched mobilities with $\mu = 10^{-2}$, 10^{-3} and 10^{-4} cm^2 V^{-1} s^{-2}, for ohmic contacts with $N = 5 \times 10^{17}$ cm^{-3} are plotted together for comparison in the top panel of **Figure 5.17**. It is clear that the V_{oc} is ≈ 0.6 V, which is 0.15 V lower than the V_{bi}, similar to

what is experimentally observed. This situation is nearly independent of μ in this range, but with a discernible fall in V_{oc} for an increase in μ. However, if the boundary conditions are switched to non-injecting contacts, through Eq(16) where N is no longer fixed by the contact, the V_{oc} increases back to 0.75 V for all cases, as plotted in the bottom panel of **Figure 5.17**. Thus it is clear that the open-circuit voltage deficit of 0.1−0.15 V present in P3HT: PCBM cells primarily derives from majority carrier injection provided by the ohmic contacts in the cells. Recombination losses do not play a significant role in limiting the V_{oc} here, unlike the situation in cells where k_{bi} is much larger.[34] Therefore shutting down ohmic injection may provide a route to improving *PCE* by shifting the V_{oc} to the V_{bi}, provided that the V_{bi} does not fall as a result.

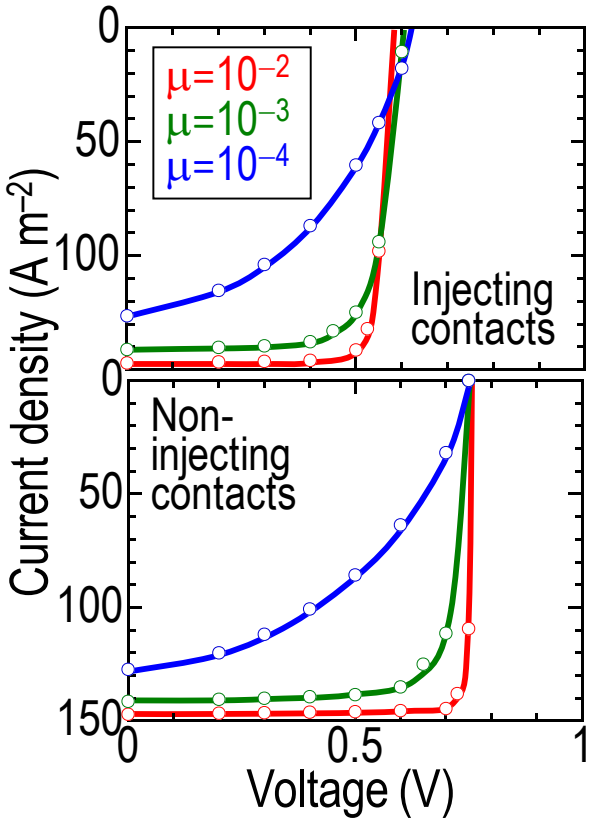

Figure 5.17 Effect of nature of contact on *JV* characteristics. Conditions are as given in **Figure 5.15**, with $u_e = u_h$. Carrier mobilities are given in units of $cm^2\ V^{-1}\ s^{-1}$.

5.4 Optical-structure optimization of organic solar cells

5.4.1 Multivariate optimization

We now consider optical-structure optimization of the PAL thickness in the cells. In general, this is a function of the thicknesses and optical properties of all layers in the cell. However for typical cell structures where a transparent conductor is used as collector of one carrier and a metal as collector of the other carrier, the optimization is strongly determined by optical interference effects set up by the reflector. In this case, *d* plays the key role, and the objective is then to determine d_{optm} for absorption of the AM1.5-weighted incident photon fraction, $\alpha_w = \int \alpha(\lambda) \cdot S(\lambda) \frac{\lambda}{hc} \cdot d\lambda$. This corresponds to finding *d* that satisfies:

$$(\frac{\partial \alpha_w}{\partial d})_{\xi_i} = 0 \text{, and } (\frac{\partial^2 \alpha_w}{\partial d^2})_{\xi_i} < 0 \quad \cdots\cdots (31)$$

where ξ_i are all the other parameters of the cell that are held constant ($\tilde{n}_{PAL}$, $\tilde{n}$, thickness of all the other layers). To simplify this, we note that for an absorption spectrum dominated by a single band, d_{optm} is approximately given by *d* that satisfies:

$$(\frac{\partial \alpha_p}{\partial d})_{\xi_i} = 0 \text{, and } (\frac{\partial^2 \alpha_p}{\partial d^2})_{\xi_i} < 0 \quad \cdots\cdots (32)$$

where α_p is the fraction of incident photon absorbed at the center wavelength in the absorption band λ_p. This reduces one layer of computation without loss of accuracy. We consider the standard device structure as before: glass/ 130-nm-thick ITO/ 50-nm-thick PEDT:PSSH/ PAL/ Ca/ Al; and only d_{opt1} and d_{opt2}, since a much larger thickness ($d_{opt3} \approx$ 300–350 nm) results in an extremely asymmetric *G*(*z*) that suffers a huge SCV penalty.

5.4.2 Effect of n_{PAL} and k_{PAL}

We found that for realistic $\tilde{n}_{PAL}$ spectra, although the extinction coefficient k_{PAL} determines the magnitude of α_p, it is the refractive index n_{PAL} that determines how α_p varies with thickness. To establish this, a set of hypothetical $\tilde{n}_{PAL}$ was generated from 1:1 w/w P3HT: PCBM and 1:3 w/w PCPDTBT: PCBM by linear scaling of the k spectrum followed Kramers–Kronig transformation to obtain the n spectrum for n fixed at infinite frequency. **Figure 5.18(a)** shows one model family of $\tilde{n}_{PAL}$ derived from P3HT: PCBM that shows k systematically varied between 0.094 and 0.58. As a result, the "free space" film absorptivity given by $\frac{4\pi}{\lambda_p}k_{PAL}$ varies between 20 and 130 x 10^3 cm^{-1} at 540-nm wavelength, near the peak of its absorption. This absorptivity range covers the practical accessible range.

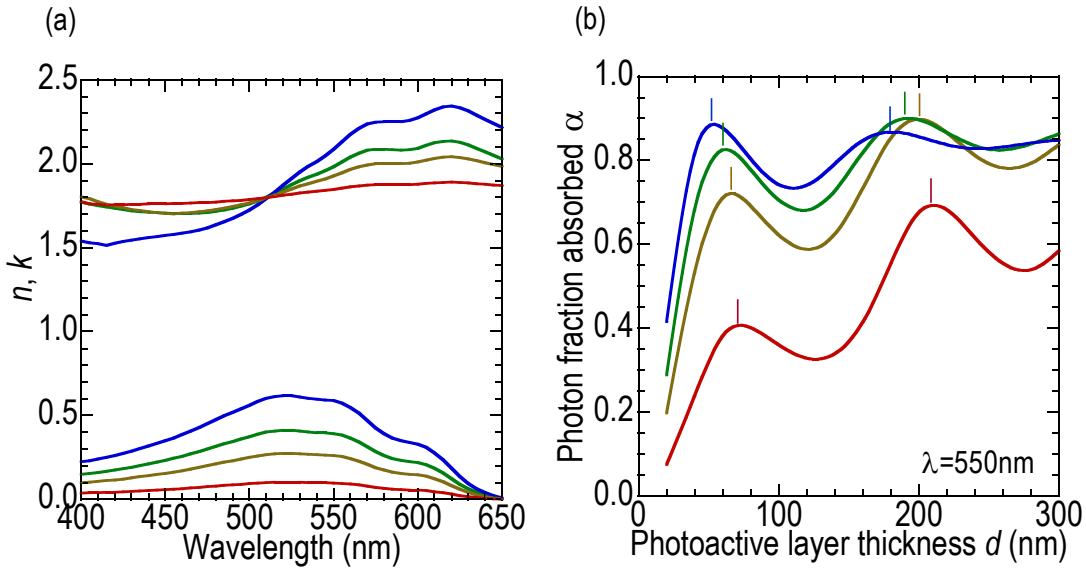

Figure 5.18 Effect of film absorptivity on the absorption oscillation. **(a)** Model dielectric functions derived from the 1:1 w/w P3HT: PCBM system. The four dielectric functions are Kramers–Kronig compliant, with peak absorptivities (at 540-nm wavelength) of 22 (red), 59 (orange), 87 (green) and 133 (blue) x 10^3 cm^{-1} respectively. **(b)** Computed fraction of incident photons absorbed in the PAL near the center absorption wavelength in the PAL as a function of thickness. Markers locate the maxima in the absorption oscillations. The colors match the respective dielectric functions in (a).

The computed dependence of α_p on d for the different model $\tilde{n}_{PAL}$ are shown in **Figure 5.18(b).** As k increases, the oscillatory α_p characteristic shifts upwards and levels off. The maximum α_p is reached at an absorptivity of ≈ 60 x 10^3 cm^{-1} for d_{opt2}. Concomittantly, d_{opt1} and d_{opt2} shift only marginally, decreasing by ≈ 20 nm for d_{opt1} and ≈ 30 nm for d_{opt2}. This shift arises primarily from the increase in n, from 1.84 to 2.08 at 540-nm wavelength, due to Kramers–Kronig consistency. This is confirmed by calculations at fixed n, which shows no change at all in d_{opt1} over the same k range. For shorter wavelengths, the relative change in n is even smaller, and so the shift is even less. Therefore the d_{optm} are rather insensitive to k_{PAL}.

5.4.3 Analytical expression for d_{optm}

The key variables that determine d_{optm} are thus n_{PAL} and the λ_p. Therefore the optical-structure optimization landscape is given by the dependence of d_{optm} on (n_{PAL}, λ_p). We characterized this surface for m = 1 and 2 by determining d_{optm} on a (n_{PAL}, λ_p) grid, for 1.5 < n_{PAL} < 2.5, and 400 < λ_p < 900 nm, keeping the thicknesses of ITO, PEDT and Ca layers constant. **Figure 5.19(a)** and **(b)** show the computed surfaces for d_{opt1} and d_{opt2} respectively. It is clear that both the d_{opt1} and d_{opt2} increase with increasing λ_p and/or decreasing n_{PAL}.

To develop a quantitative equation for the $d_{optm}(n_{PAL}, \lambda_p)$ surface, we employ a "half-space" model which considers the optical interference within the PAL due to the back reflector. The half-space model has previously been described for organic LEDs.[11] Full device optical structure calculations have confirmed that this model correctly reproduces the radiation profile.[12] The simplification obtained leads to useful design rules.

For a half-space model, elementary wave theory gives the constructive interference distance (d_m) to the optical-field antinode from the reflector, at normal incidence, to be:

$$2k_p n_{PAL} d_m + \Delta_r = 2m\pi \cdots\cdots (33)$$

where k_p is the free-space wavevector ($2\pi/\lambda_p$), Δ_r is the reflection phase shift, and m is the optical-field antinode index. For typical evaporated metal films on OSCs, Δ_r can deviate significantly from the ideal value of π for a perfect reflector.[11] To model this, we consider a simple empirical function of the form:

$$\Delta_r = \pi - a_1 - a_2 \frac{n_{PAL}}{\lambda_p} - a_3 \frac{n_{PAL}}{\lambda_p^2} \cdots\cdots (34)$$

where a_1, a_2 and a_3 are empirical coefficients that depend on the OSC/ metal interface.

Rearranging, we obtain the antinode positions to be given by:

$$d_m = \frac{(2m-1)\pi + a_1}{4\pi} \frac{\lambda_p}{n_{PAL}} + \frac{a_2}{4\pi} + \frac{a_3}{4\pi\lambda_p} \cdots\cdots (35)$$

d_{optm} is larger than d_m by a geometric factor that accommodates the width of the antinode. We found $d_{opt1} \approx 2 * d_1$ and $d_{opt2} \approx 4/3 * d_2$. This suggests that the $d_{optm}(n_{PAL}, \lambda_p)$ surface obeys an equation of the form:

$$d_{optm}(n_{PAL}, \lambda_p) = b_1 \frac{\lambda_p}{n_{PAL}} + b_2 + \frac{b_3}{\lambda_p} \cdots\cdots (36)$$

where the b variables are related to the a variables and the geometric factor.

We fitted the surfaces to Eq(36). The fit is excellent as shown by the close match between the half-space model and the full optical-structure calculation for both d_{opt1} (spanning the d range 40−200 nm) and d_{opt2} (140−440 nm). The fits are shown as contour lines, and the fit parameters given in the caption of **Figure 5.19**.

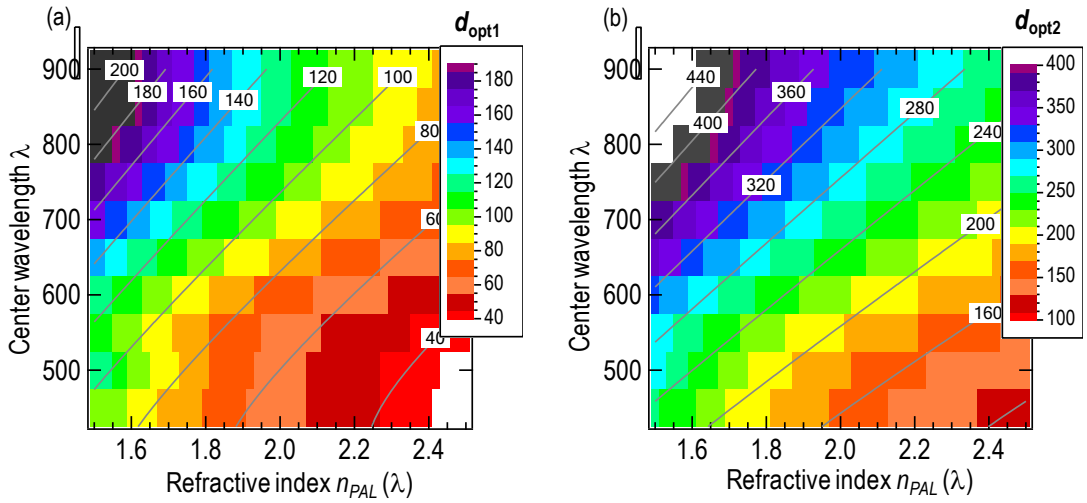

Figure 5.19 Computed optimal PAL absorption thickness as a function of absorption center wavelength and refractive index. Device structure: glass/ 130-nm ITO/ 50-nm PEDT: PSSH/ PAL/ 30-nm Ca/ Al. The computed surface is well-described by a simple half-space model (see text) with b_1 = 0.545±0.005, b_2 = –151.4±3.4 nm, and b_3 = 37,500±1,100 nm^2 for d_{opt1}; and b_1 = 0.981±0.005, b_2 = –138.0±3.3 nm, and b_3 = 35,700±1,100 nm^2 for d_{opt2}.

The values of b_1 are close but not identical to the values expected for a perfect reflector, which are 0.5 and 1.0 for m = 1 and 2 respectively. The values of b_2 and b_3 for the d_{opt1} and d_{opt2} fits are also broadly in agreement. This suggests the simple half-space model does indeed provide a sufficiently accurate and self-consistent description of d_{optm}. The results do not change significantly when ITO or PEDT: PSSH thicknesses, or k_{PAL}, are varied within reasonable limits. However they do change with the metal reflector. We found that this change can be represented in first order by a linear shift. When the reflector is changed from Ca (a "poor" metal in the optical sense, for which Δ_r is significantly larger than π),[11] to Al (a "good" metal), the b_2 value increases only by +14 nm.

The key value of Eq(36) is the insight gained and the *a priori* estimation of d_{optm} that is now possible. For example, for 1:1 w/w P3HT: PCBM/ Ca, where λ_p = 530 nm and n_{PAL} = 1.90, the equation predicts d_{opt1} = 75 nm and d_{opt2} = 200 nm, which are in excellent agreement with experiment. For 1:3 w/w PCPDTBT: PCBM/ Ca, where λ_p = 750 nm and n_{PAL} = 1.90, the equation gives d_{opt1} = 110 nm and d_{opt2} = 290 nm, which is also in agreement with the full optical-structure calculations (Section III). It is clear that this rather large shift here comes primarily from the λ_p / n_{PAL} term. If the reflector is changed to Al (or Ag), 14 nm should to be added to these results.

The chief value of such an approach is it allows one to quickly work out the d_{optm} required simply from the measured $\tilde{n}$ spectrum and the parameters for the reflector. For example, for the P3HT: PCBM (1:1 w/w) system, λ = 530 nm and n_{PAL} = 1.9. The model predicts d_{opt1} = 75 nm and d_{opt2} = 200 nm, in agreement with experiment. For the PCPDTBT: PCBM (1:3 w/w) system, λ = 750 nm and n_{PAL} = 1.90. The model predicts d_{opt1} = 110 nm and d_{opt2} = 290 nm. The bulk of this very sizeable shift comes simply from the λ / n_{PAL} scaling relation. Add 14 nm to the results if the metal electrode is changed to Al or Ag.

5.5 Conclusions

We have successfully simulated the *JV* characteristics of high quantum efficiency crosslinked P3HT network: PCBM solar cells over a wide PAL thickness range using the standard optical–electrical model, with a calibrated set of global parameters. This shows that the behavior of

these solar cells can be described in first order by rather simple physics, which provides confidence in the model and its parameters. We have learnt the following:

(i) The electron−hole recombination rate in P3HT: PCBM cells is lower than the Langevin model by 2–3 orders of magnitude, in agreement with other authors, which can be explained by a simple geometric scaling argument to arise from separate confinement of electrons and holes;

(ii) The interface mobile carrier density that contributes to the injected current density is lower than the actual δ-doped carrier density at the contacts by 1–2 orders of magnitude, which provides evidence for energy broadening;

(iii) The built-in potential in PEDT: PSSH/ P3HT: PCBM/ Ca cells is 0.75 V, with the negative polaron levels of P3HT and PCBM at 3.2 and 3.5 eV respectively;

(iv) The open-circuit voltage deficit in these cells is only 0.1–0.15 V, which is primarily due to carrier injection at the ohmic contacts, which may be suppressed with suitable contact engineering;

(v) Optimal transport requires the mobilities of both electrons and holes to be high, and if the mobilities are mismatched, the distal carrier needs to have the higher mobility;

(vi) The photocarrier generation rate is an oscillatory function of the PAL film thickness with the location of maxima governed by a simple scaling with leading λ_p / n_{PAL} term, where λ_p is absorption center wavelength and n_{PAL} is refractive index.

5.6 References

1 Png, R. Q. *et al.* High-performance polymer semiconducting heterostructure devices by nitrene-mediated photocrosslinking of alkyl side-chains. *Nature Mater.* **9**, 152-158 (2010).

2 Liu, B. *et al.* Very high internal quantum efficiency over wide composition phase space in polymer: fullerene solar cells based on crosslinked polymer donor networks *Nat. Commun. in press* (2012).

3 Koster, L., Smits, E., Mihailetchi, V. & Blom, P. W. M. Device model for the operation of polymer/fullerene bulk heterojunction solar cells. *Phys. Rev. B* **72**, 085205 (2005).

4 Mihailetchi, V. D., Xie, H., de Boer, B., Koster, L. J. A. & Blom, P. W. M. Charge transport and photocurrent generation in poly(3-hexylthiophene):methanofullerene bulk heterojunction solar cells. *Adv. Funct. Mater.* **16**, 699-708 (2006).

5 Kotlarski, J. D., Blom, P. W. M., Koster, L., Lenes, M. & Slooff, L. H. Combined optical and electrical modeling of polymer: fullerene bulk heterojunction solar cells. *J. Appl. Phys.* **103**, 084502 (2008).

6 Pettersson, L. A. A., Roman, L. S. & Inganäs, O. Modeling photocurrent action spectra of photovoltaic devices based on organic thin films. *J. Appl. Phys.* **86**, 487 (1999).

7 Hoppe, H., Arnold, N., Sariciftci, N. & Meissner, D. Modeling the optical absorption within conjugated polymer/fullerene-based bulk-heterojunction organic solar cells. *Sol. Energ. Mat. Sol. Cells* **80**, 105-113 (2003).

8 Hoppe, H., Arnold, N., Meissner, D. & Sariciftci, N. Modeling of optical absorption in conjugated polymer/fullerene bulk-heterojunction plastic solar cells. *Thin Solid Films* **451**, 589-592 (2004).

9 Sievers, D. W., Shrotriya, V. & Yang, Y. Modeling optical effects and thickness dependent current in polymer bulk-heterojunction solar cells. *J. Appl. Phys.* **100**, 114509 (2006).

10 Moulé, A. J., Bonekamp, J. B. & Meerholz, K. The effect of active layer thickness and composition on the performance of bulk-heterojunction solar cells. *J. Appl. Phys.* **100**, 094503 (2006).

11 Kim, J. S., Ho, P. K. H., Greenham, N. C. & Friend, R. H. Electroluminescence emission pattern of organic light-emitting diodes: Implications for device efficiency calculations. *J. Appl. Phys.* **88**, 1073-1081 (2000).

12 Ho, P. K. H. Unpublished. (2005).

13 Dennler, G., Scharber, M. C. & Brabec, C. J. Polymer:fullerene bulk-heterojunction solar cells. *Adv. Mater.* **2009**, 1323-1338 (2009).

14 Peet, J. *et al.* Efficiency enhancement in low-bandgap polymer solar cells by processing with alkane dithiols. *Nature Mater.* **6**, 497-500 (2007).

15 Lee, K. L. *et al.* Processing additives for improved efficient from bulk heterojunction solar cells. *J. Am. Chem. Soc.* **130**, 3619-3623 (2008).

16 Zhou, M. *et al.* The role of delta-doped interfaces for Ohmic contacts to organic semiconductors. *Phys. Rev. Lett.* **103**, 036601-036601-036604 (2009).

17 Zhou, M. *et al.* Effective work functions for the evaporated metal/organic semiconductor contacts from in-situ diode flatband potential measurements. *Appl. Phys. Lett.* **101**, 013501 (2012).

18 Campbell, I. H., Hagler, T. W., Smith, D. L. & Ferraris, J. P. Direct measurement of conjugated polymer electronic excitation energies using metal/ polymer/ metal structures. *Phys. Rev. Lett.* **76**, 1900-1903 (1996).

19 Brewer, P. J. *et al.* Role of electron injection in polyfluorene-based light emitting diodes containing PEDOT:PSS. *Phys. Rev. B* **71**, 205209 (2005).

20 Bodrozic, V. *et al.* The built-in potential in blue polyfluorene-based light-emitting diodes. *Adv. Mater.* **20**, 2410-2415 (2008).

21 Zhou, M. *et al.* Determination of the interface delta-hole density in a blue-emitting organic semiconductor diode by electromodulated absorption spectroscopy. *Appl. Phys. Lett.* **97**, 113505-113501-113504 (2010).

22 Braun, C. L. Electric field assisted dissociation of charge transfer states as a mechanism of photocarrier production. *J. Chem. Phys.* **80**, 4157 (1984).

23 Marsh, R. A., Hodgkiss, J. M. & Friend, R. H. Direct measurement of electric field-assisted charge separation in polymer:fullerene photovoltaic diodes. *Adv. Mater.* **22**, 3672–3676 (2010).

24 Howard, I. A., Mauer, R., Meister, M. & Laquai, F. Effect of morphology on ultrafast free carrier generation in polythiophene: fullerene organic solar cells. *J. Am. Chem. Soc.* **132**, 14866-14876 (2010).

25 Deibel, C., Wagenpfahl, A. & Dyakonov, V. Influence of charge carrier mobility on the performance of organic solar cells. *Phys. Stat. Solid.* **2**, 175-177 (2008).

26 Shuttle, C. *et al.* Experimental determination of the rate law for charge carrier decay in a polythiophene: Fullerene solar cell. *Appl. Phys. Lett.* **92**, 093311 (2008).

27 Shuttle, C. *et al.* Bimolecular recombination losses in polythiophene: Fullerene solar cells. *Phys. Rev. B* **78**, 113201 (2008).

28 Zhao, L. H. *et al.* Polarization effects on energy-level alignment at the interfaces of polymer organic semiconductor films. *Appl. Phys. Lett.* **101**, 053304 (2012).

29 Gummel, H. A self-consistent iterative scheme for one-dimensional steady state transistor calculations. *IEEE T. ELECTRON. DEV.* **11**, 455-465 (1964).

30 Scharfetter, D. & Gummel, H. Large-signal analysis of a silicon read diode oscillator. *IEEE T. ELECTRON. DEV.* **16**, 64-77 (1969).

31 Juška, G., Arlauskas, K., Stuchlik, J. & Österbacka, R. Non-Langevin bimolecular recombination in low-mobility materials. *J. Non-Cryst. Solids.* **352**, 1167-1171 (2006).

32 Waldauf, C. *et al.* Highly efficient inverted organic photovoltaics using solution based titanium oxide as electron selective contact. *Appl. Phys. Lett.* **89**, 233517 (2006).

33 Kim, J. Y. *et al.* New architecture for high-efficiency polymer photovoltaic cells using solution-based titanium oxide as an optical spacer. *Adv. Mater.* **18**, 572-576 (2006).

34 Koster, L. J. A., Wienk, M. M., Maturová, K. & Janssen, R. A. J. Quantifying bimolecular recombination losses in organic bulk heterojunction solar cells. *Adv. Mater.* **23**, 1670-1674 (2011).

Chapter 6. Summary and outlook

Polymer electronics is a young and promising field that may open up new possibilities and applications such as solar cells. This new class of materials also exhibit some new properties and physics that were never seen before.

In this thesis, we have demonstrated that acceptor doping into a lightly-crosslinked polymer donor film produces a remarkable nanotemplated network morphology that can sustain near unity photocurrent generation efficiency over a very wide composition phase space. This is an advance over the standard biblend demixing method. We have also demonstrated clear evidence for the roles of the 1D photonic structure and of compositional effect on morphology. By providing a means to "fix" the morphology, the heterostructure becomes robust, and the morphology can become decoupled from the electronic structure. This lays down a clear path towards the general optimization of polymer: fullerene and other heterostructures, e.g. the recombination of low bandgap polymer and more absorbing $PC_{71}BM$ for higher Jsc, deep HOMO polymer for higher Voc, and even tandem solar cells, etc. It can be also extended to the nanoscale morphology manipulation in other polymer systems.

In order to further understand the device physics, we have pinned down a very important parameter (the built-in potential), successfully fitted the JV characteristics with single set of parameters for all experimental data and summarized several design rules for solar cells. More detailed work can be done on the recombination mechanism and modeling, and on the origin of the Vbi in actrual devices.

Appendix

A. Publications related to work done in this thesis

1. Png, R.Q., Chia P.J., Tang J.C., Liu B., Sivaramakrishnan S., Zhou M., Khong S-H., Chan H. S. O., Burroughes J. H., Chua L.L., Friend R.H., Ho P.K.H., "High-performance polymer semiconducting heterostructure devices by nitrene-mediated photocrosslinking of alkyl side-chains". *Nature Mater.* **9**, 152-158 (2010).
2. Liu, B., Png, R.Q., Zhao L.H., Chua L.L., Friend R.H., Ho P.K.H., "Very high internal quantum efficiency over wide composition phase space in polymer: fullerene solar cells based on crosslinked polymer donor networks". *Nat. Commun.*, 3 (2012) 1321.
3. Liu, B., Png, R.Q. & Ho, P.K.H., "New Organic solar cell design rule: Influence of non-uniform exciton generation profile and charge carrier mobility on organic solar cell performance". In preparation (2012).

B. Publications (up till 2012) from work not described in this thesis

1. Zhao, B., Liu, B., Png, R.Q., Zhang, K., Lim, K. A., Luo, J., Shao, J., Ho, P.K.H., Chi, C., Wu, J., "New Discotic Mesogens Based on Triphenylene-fused Triazatruxenes: Synthesis, Physical Properties and Self-assembly". Chem. Mater. 2010, 22, 435-449.

C. Conference presentations (presenting author underlined)

1. Liu, B., Png, R.Q., Zhao L.H., Chua L.L., Friend R.H., Ho P.K.H., "High-efficiency polymer-based single-layer solar cells based on molecular infiltration of the acceptor", E-MRS Spring 2011, Nice, France. (Oral presentation)
2. Liu, B., Png, R.Q., Friend R.H., Ho P.K.H., "High-efficiency bulk heterojunction organic solar cells based on ultrafine contiguous crosslinked polymer donor networks", International Conference on Simulation of Organic Electronics and Photovoltaics (SimOEP12), Oliva, Valencia, Spain. (Oral presentation)

3. Liu, B., Png, R.Q., Zhao L.H., Chua L.L., Friend R.H., Ho P.K.H., “High-efficiency bulk heterojunction organic solar cells based on ultrafine contiguous crosslinked polymer donor networks”, International Conference of Young Researchers on Advanced Materials (ICYRAM 2012), Singapore. (Poster presentation)